Charles University, Prague
Faculty of Mathematics and Physics
Department of Electronic Structures

Doctoral Thesis

Synthesis and study of new hydrides based on *f*-metals

Khrystyna Miliyanchuk

Supervisor: Doc.RNDr. Ladislav Havela, CSc.

Prague
2006

Acknowledgements

At the very beginning I would like to thank all the people who contributed to the realization of the following work.

First of all I should express my sincerest gratitude to my supervisor Doc.RNDr. Ladislav Havela, CSc. whose thorough guidance led me through the whole process of the research activity – from the stage of stating the task till the search for the methods of realization and the analysis. Thanks to his huge experience, keen observations, understandable explanations, patience and vivid discussions I could gradually progress in my own understanding and skills.

I would like to thank my consultants Prof. Dr. Alexandr Andreev and Doc.RNDr. Martin Diviš, CSc. Prof. Andreev's long experience in the physics of uranium intermetallics and fruitful discussions led to the generation of new ideas, which mostly proved to be justified by interesting results. Due to the lectures of Doc. Diviš I was able to consider the studied phenomena from completely different point of view, since the theoretical approach made it possible to see what is behind our observation and to see beyond the limitations of the experimental setup.

I feel true gratitude to the leader of the group of magnetic properties and for most time of my studies the Chairman of the Department of Electronic Structures Prof. RNDr. Vladimír Sechovský, DrSc., who made everything possible to make my work comfortable and effective and whose support and interest in my work served always as an encouragement for me. I would like to thank the present Chairmen of the Department of Electronic Structures Doc. RNDr. Radomír Kužel, CSc., for initiating tight collaboration for me with the group of X-rays analysis what helped to perform structure studies without any complications. I highly appreciate the assistance of Doc. RNDr. Pavel Svoboda, CSc., in the samples preparation, what was the origin for all the further studies. My thanks go to Mgr. Stanislav Daniš, Ph.D., whose skills in crystal structure analysis helped to solve different non-trivial tasks. The discussions with Doc. Pavel Javorský contributed much to my understanding of the heat capacity results and neutron diffraction studies. I wish to thank Mgr. Oleksandr Kolomiyets, Ph.D., for introducing me to the field of solid state physics. I would like to thank my collegues RNDr. Jana Poltierová-Vejpravová, Mgr. Jiři Prchal, Mgr. Jan Prokleška, Mgr. Denys Vasilyev, Ph.D., RNDr. Ján Rusz, Ph.D. who were always willing to share their experience, and to thank the whole stuff of the Deparment of Electronic Structures for friendly creative atmosphere and team spirit.

I want to express my deep gratitude to RNDr. Eva Šantavá, CSc., for her kind assistance in the physical properties measurements at the JLMS. My thanks also go to Ing. Miroslav

Maryško, CSc., for the help with SQUID measurement at the Academy of Sciences of Czech Republic.

I would like to express my thanks to the team of Solid State Chemistry from the Instituto Tecnólogico e Nuclear/CFMC-UL, Sacavém, Portugal, for fruitful collaboration and hospitality. Dr. Laura Pereira's and Dr. António Pereira Gonçalves's experience in the studies of U_2T_2X compounds led to a series of fascinating results. I would like also to thank Dr. João Carlos Waerenborgh and Dr. Piotr Gaczynski for introducing me to the Mössbauer spectroscopy experiment.

I want also to thank Dr. Karel Prokeš, DrSc., from Hahn-Meitner Institute, Berlin, for his help in performing the neutron diffraction experiment.

Last but not least I want to thank my family and Dr. Yaroslav Galadzhun for their love, support, and encouragement, and all my Prague friends whose part in solving various problems and sharing amusements was equally important.

Contents

Introduction 5

1. Electronic and magnetic properties of actinides 6

1.1. Hubbard model 6

1.2. Stoner model 7

1.3. Finite temperatures 11

1.4. Magnetic properties of uranium intermetallics 12

2. Metal-hydrogen systems 14

2.1. Binary diagrams of metal-hydrogen systems and hydride formation criteria 15

2.2. Effect of hydrogenation on the electronic structure and magnetism 19

3. U*TX* and U_2T_2X compounds: state of the art 21

3.1. U*TX* compounds 21

3.2. U_2T_2X compounds 24

3.3. Hydrides of uranium ternaries 27

4. Sample preparation and experimental techniques 30

4.1. Hydrides Synthesis 30

4.2. X-ray diffraction studies and crystal structure refinement 31

4.3. Neutron diffraction 33

4.4. Magnetic measurements 36

4.5. Specific heat measurements 36

4.6. Mössbauer Spectroscopy 38

5. Results and discussion 42

5.1. Hydrides of U*TX* compounds 42

5.1.1. Hydrides of UCoSn and URuSn compounds: crystal structure and magnetism 42

5.1.2. Hydrides of $UCo_{1-x}Ru_xSn$ compounds: crystal structure and magnetism 46

5.1.3. Deuterides of UCoSn and URuSn 49

5.1.4. Hydride of UCoSi: crystal structure and magnetism 59

5.2. Hydrides of U_2T_2X compounds 65

5.2.1. Hydrides of U_2Co_2Sn 65

5.2.1.1. α-$U_2Co_2SnH_x$ 66

5.2.1.2. β-$U_2Co_2SnH_{1.4}$ 70

5.2.2. $U_2Ni_2SnH_{1.8}$ and $U_2Ni_2InH_{1.9}$ hydrides 71
5.2.3. $U_2Ni_2SnD_{1.8}$ deuteride 75
5.2.4. $U_2Co_2InH_{1.9}$ and $U_2Fe_2SnH_{1.7}$ hydrides 81
5.2.5. Hydrogenation of U_2Pd_2In 85
6. Conclusions 86
References 89
Appendix A 95
Appendix B 96
Appendix C 97
Appendix D 99
Appendix E 101
Appendix F 102

Introduction

Hydrogenation is a powerful tool capable of changing both crystal and electronic structure of intermetallic compounds. As a result, the new compounds – hydrides – exhibit qualitatively new physical properties and such modifications provide us with additional information on the peculiarities of interatomic interactions in the initial compounds on the one hand, and on the other hand it gives rise to completely new compounds, frequently with fascinating properties. One should consider two main effects of hydrogen absorption on the intermetallic compounds. Hydrogen acts as small perturbation on the system expanding it, *i.e.* plays the role of negative pressure agent. The other, sometimes more important effect, is the bonding of hydrogen to other atoms in the lattice.

Intermetallic compounds of 5*f* elements, including uranium, are especially sensitive to hydrogen absorption. For purely band systems, the interatomic distance between the uranium atoms is a crucial parameter, which determines the magnetic properties. However, most of uranium intermetallics are characterized by a 5*f*-ligand hybridisation, and the strength of hybridisation is an extremely important parameter. Hydrogen intrusion can easily modify the hybridised band by withdrawing electronic states due to chemical bonding with the atoms which contribute to the band.

This work presents the results of studies of two groups of intermetallic compounds of uranium. Our results on the hydrides of the compounds with U*TX* stoichiometry (*T* – transition metal, *X* – *p*-element) complete the studies, started in the previous period already. Hydrides of U_2T_2X compounds form a new large group of uranium-based hydrides and we are particularly focused on these compounds.

1. Electronic and magnetic properties of actinides

The elements of the periodic table between actinium (Z = 89) and lawrencium (Z = 103) are labelled as actinides. Their atomic structure consists of radon core, a partially filled 5*f*-shell, and two to four valence electrons in the atomic 6*d* and 7*s* states. Generally (with few exceptions) it can be described as:

$$(\mathrm{Rn})^{86}5f^{N}6d^{1}7s^{2}\ (N = 0 \div 14)$$

Unlike rare-earth metals, for which the 4*f* states are localized, the 5*f* electrons of the actinides are not so well localized, especially for the first part of actinides series. Such delocalisation leads to several important consequences. First of all, the formation of more or less narrow band intersected by the Fermi energy E_F can result in considerable decrease of magnetic moments compared to free ion values. Moreover, magnetic moments totally disappear in a broad-band limit leading to weak (Pauli) paramagnetism. Besides some hybridisation both with 6*d* and 7*s* bands, hybridisation with the electronic states of ligand atoms occurs. In case of presence of magnetic moments, the strength of magnetic coupling is typically larger than for analogous 4*f* states interacting via RKKY interaction.

1.1. Hubbard Model

One of the simplest models to describe the electron correlations and solid state magnetism is Hubbard model [1]. It combines electron hopping between neighbouring sites and the Coulomb repulsion of electrons at the same site. The Pauli principle is taken into account. The Hubbard Hamiltonian is the following:

$$H = \sum_{ij\sigma} t_{ij} c_{i\sigma}^{+} c_{j\sigma} + U \sum_{i} n_{i\uparrow} n_{i\downarrow}\ , \tag{1.1}$$

where electron hopping is determined by the t_{ij} parameter, whereas the parameter U models the Coulomb interaction. $c_{i\sigma}^{+}, c_{i\sigma}$ are the fermion creation and annihilation operators for an electron with spin σ on site i and $n_{i\sigma} = c_{i\sigma}^{+} c_{i\sigma}$ is the related ladder operator counting the occupation on site i.

Depending on the sign of U the Hubbard Hamiltonian describes various phases:

- U > 0 (repulsive): paramagnetic metallic, ferromagnetic metallic, antiferromagnetic insulating,

- U < 0 (attractive): normal Fermi liquid, superconducting, charge density wave (insulator), normal Bose liquid (insulator).

Being rather simple, Hubbard model describes complex quantum-mechanical problem. A drawback of this model is that it does not work for the ferromagnetic ordering, since it does not allow electron hopping while all the spins are aligned. Meanwhile, for approximately half-filled band the antiferromagnetic alignment it is more apt since it makes hopping process favourable.

1.2. Stoner Model

Stoner theory of itinerant magnetism for *d*-metals [2, 3], being in fact the mean field limit of Hubbard model, describes particles, which move freely in the periodic potential of the solid as a more or less free electron gas. The electron states are not described by discrete energy levels but by density of states formed by energy bands. The model is based on the following postulates:

- the carriers of magnetism are the electrons in the *d* (or *f*) band;
- effects of exchange are treated within a molecular field term;
- Fermi statistics should be fulfilled.

The theory is derived from a paramagnetic density of states, which is split into two identical bands for spin-up and spin-down. If an external magnetic field (molecular field) is applied, the bands become shifted to new values ε_f^+ for spin-up and ε_f^- for spin-down and two subbands are formed due to the redistribution of electrons. The occupancies of the spin-up n^+ and spin-down n^- bands differ therefore. The Stoner equations can be formulated:

$$n^{\pm} = \int_0^{\infty} N(\varepsilon) \frac{1}{\exp(\frac{\varepsilon}{k_B T} - \eta^{\pm}) + 1} d\varepsilon \qquad (1.2)$$

$$k_B T \eta^{\pm} = k_B T \eta \pm \frac{IM}{2} \pm \mu_B H_{ex} \text{ with } \eta = \frac{\mu}{K_B T}$$

μ is chemical potential which is equal to the Fermi energy what is the energy of the highest occupied state, and consequently the new Fermi energies, caused by the field, can be considered

as chemical potentials for spin-up (+) and spin-down (−) as μ^+ and μ^-. The energy shift due to splitting can be given as:

$$\Delta E = IM = I(n^+ - n^-) \tag{1.3}$$

Both in Eqns. (1.2) and (1.3), the quantity I is the Stoner exchange factor and M is the magnetic moment. Magnetic susceptibility is determined therefore as:

$$\chi = \frac{M}{H} = \frac{2\mu_B^2 \int_0^\infty N(\varepsilon)\left|\frac{df}{d\varepsilon}\right| d\varepsilon}{1 - I\int_0^\infty N(\varepsilon)\left|\frac{df}{d\varepsilon}\right| d\varepsilon} \tag{1.4}$$

where df/dε is the energy derivative of the Fermi-Dirac distribution. Eqn. (1.4) is the most general form of the Stoner susceptibility. At T = 0 K it is reduced to:

$$\chi = \frac{2\mu_B^2 N(\varepsilon_F)}{1 - IN(\varepsilon_F)} = 2\mu_B^2 N(\varepsilon_F) S \tag{1.5}$$

The term $2\mu_B^2 N(\varepsilon_F)$ is Pauli susceptibility describing noninteracting (no exchange) gas of free electrons and S is Stoner enhancement factor. If $IN(\varepsilon_F)$ factor is larger than unity, then χ becomes negative and formation of spontaneous magnetic order occurs. This gives rise to well-known Stoner criterion, which defines the onset of magnetism if

$$IN(\varepsilon_F) \geq 1 \tag{1.6}$$

Since Stoner exchange factor I is quasi-atomic property which depends only very little on chemical or metallurgical effects (bonding, alloying, etc.), the possible formation of magnetic moments depends on the density of states at Fermi level $N(\varepsilon_F)$.

If a system fulfills the Stoner criterion for magnetic order, Eqn. (1.4) also allows to calculate the Curie temperature providing the magnetic order disappears at the temperature when denominator of Eqn. (1.4) becomes zero:

$$I\int_0^\infty N(\varepsilon)\left|\frac{df}{d\varepsilon}\right| d\varepsilon = 1 \tag{1.7}$$

Eqn. (1.7) is a temperature dependent Stoner criterion. Unfortunately, the Curie temperatures calculated within Stoner model are at least one order of magnitude higher than the observed values. Therefore effective Fermi degeneracy temperature T_F was introduced:

$$T_F^{-2} = \left| \frac{\pi^2 k_B^2}{6}\left[\frac{N(\varepsilon_F)''}{N(\varepsilon_F)} - \left(\frac{N(\varepsilon_F)'}{N(\varepsilon_F)}\right)\right]^2 \right| \tag{1.8}$$

which depends on the local structure of the density of states at the Fermi energy via its first and second energy derivative (Sommerfield expansion) and takes into account the softening of the

Fermi-Dirac distribution at $T \neq 0$ K, creating holes below the Fermi energy and occupied states above. With the definition of T_F, T_C can be rewritten:

$$T_C^2 = T_F^2 (IN(\varepsilon_F) - 1) \tag{1.9}$$

It is seen that T_C becomes considerably smaller only if $IN(\varepsilon_F)$ is slightly larger than one, that is the model can work for very weak itinerant electron magnetism.

The finite temperatures behaviour of the susceptibility and the magnetic moment in the terms of the Stoner model are described by the equation for the magnetic isotherms of weakly itinerant systems:

$$\left(\frac{M(H,T)}{M(0,0)}\right)^3 - \frac{M(H,T)}{M(0,0)}\left(1 - \frac{T^2}{T_C^2}\right) = \frac{2\chi_0 H}{M(0,0)} \tag{1.10}$$

Eqn. (1.10) describes Arrott plots which were also found experimentally and represent linear dependence between M^2 and H/M. One finds parallel lines with a constant slope, which has the value $2\chi_0$, where χ_0 is the zero field differential susceptibility. The intersection with the M^2 axis is given by:

$$M^2 = M(0,0)^2 (1 - \frac{T^2}{T_C^2}), \tag{1.11}$$

so that distance between the parallel lines is given by the temperature dependence of magnetization. Additional effects (inhomogeneities or magnetization processes in small fields, spin fluctuations in high fields) often cause the deviations from linearity. Other non-linearities can be caused by critical phenomena, *i.e.* deviations from the mean-field behaviour.

The inverse susceptibility $\frac{\mathrm{d}H}{\mathrm{d}M}$ determined from Eqn. (1.10) yields:

$$\frac{\mathrm{d}H}{\mathrm{d}M} = \frac{1}{\chi} = \frac{3M^2}{2\chi_0 M_0^2} - \frac{1}{2\chi_0}\left(1 - \frac{T^2}{T_C^2}\right) \tag{1.12}$$

One should consider two cases:

1. $T > T_C$

   Above the Curie temperature the magnetic moment becomes zero and one obtains

$$\chi = 2\chi_0 \left(\frac{T^2}{T_C^2} - 1\right)^{-1} \tag{1.13}$$

2. $T < T_C$

   In the ordered state one should consider the temperature dependence of magnetization represented by Eqn. (1.11) in order to get:

$$\chi = \chi_0 \left(1 - \frac{T^2}{T_C^2} \right)^{-1} \tag{1.14}$$

The reason for the change of susceptibility by the factor of two lies in the fact that the susceptibility simply measures the amount of magnetic moment produced by applied field. In the Stoner model there is no magnetic order above T_C, therefore magnetic field creates spins from the "spin vacuum". Meanwhile in the magnetically ordered state all spins are parallel to the molecular field and the applied field has to flip the spin from – to +, which explains the factor of two. However in both cases the inverse susceptibility does not show the Curie-Weiss behaviour, but always the T^2 dependence.

Eqn. (1.10) is equal to the Landau expansion of the free energy of ferromagnet which reads:

$$F = \frac{1}{2} A M^2 + \frac{1}{4} B M^4 - MH \tag{1.15}$$

From the extremal conditions ($\frac{dF}{dM} = 0$ and $\frac{d^2F}{dM^2} > 0$) and using Eqn. (1.14), the coefficients A and B can be easily derived:

$$A = -\frac{1}{2\chi_0} \left(1 - \frac{T^2}{T_C^2} \right) \quad , \tag{1.16}$$

$$B = \frac{1}{2\chi_0 M_0^2} \tag{1.17}$$

Furthermore the relationships which can be found are:

$$M_0^2 = -\frac{A}{B} \tag{1.18}$$

$$\Delta F = -\frac{M_0^2}{8\chi_0} \tag{1.19}$$

$$M^2 = M_0^2 \left(1 - \frac{T^2}{T_C^2} \right) \tag{1.20}$$

where χ_0 and M_0 are the susceptibility and magnetic moment at equilibrium, respectively, ΔF is the difference in energy between the magnetic and the non-magnetic state at $T = 0$, and M is the magnetic moment at a given temperature T. Replacing A, B, and M in Eqn. (1.15) by the respective expressions given by Eqns. (1.16), (1.17), and (1.20), yields the temperature dependence of the free energy at $H = 0$ as following:

$$F_m = -\frac{M_0^2}{8\chi_0}\left(1-\frac{T^2}{T_C^2}\right)^2 \tag{1.21}$$

Although the Stoner model works very well for the ground-state properties at $T = 0$ K, it totally fails at finite temperatures. No reasonable values for the ordering temperatures can be obtained, neither the correct power law for the temperature dependence of magnetic susceptibility. The reason is the presence of transversal spin-fluctuations, which were not accounted within the theory. Therefore one had go beyond the Stoner model.

1.3. Finite Temperatures

Several theories were developed which took into account the fluctuations and which may provide a reasonable description of fluctuations of the spin density in itinerant electron systems [4]. Murata and Doniach [5] proposed to use the mean square of the local spin density in the expansion of free energy instead of the bulk magnetization *M*, reflecting the fact that magnetization becomes a spatial distributed quantity. The amplitude of spin fluctuations is increasing with temperature, which can lead to the Curie-Weiss-type susceptibility. This treatment carries totally new character for the temperature dependencies for magnetic moment and susceptibility. Thus Eqn. (1.20) is changed for:

$$M^2 = M_0^2\left(1-\frac{T}{T_C}\right) \tag{1.22}$$

This behaviour differs from the Stoner model insofar as the reduction of the magnetic moment at low temperatures is stronger. The reason is that the collective modes described by the spin fluctuations can be readily excited at low temperature, where the Stoner excitations are very small.

The susceptibility below and above T_C is given by

$$\chi = \chi_0\left(\frac{T}{T_C}-1\right)^{-1} \qquad \text{for } T < T_C, \tag{1.23}$$

$$\chi = 2\chi_0\left(\frac{T^2}{T_C^2}-1\right)^{-1} \qquad \text{for } T \geq T_C, \tag{1.24}$$

which leads to a Curie constant *C*

$$C = \frac{d\chi^{-1}}{dT} = \frac{1}{2\chi_0 T_C}, \tag{1.25}$$

which is no longer temperature dependent (as for the Stoner model) and thus describes a Curie-Weiss behavior.

The most successful in qualitative and quantitative description of spin fluctuations in itinerant magnets has been the Self-Consistent Renormalisation (SCR) theory of spin fluctuations developed by Moriya [6]. He used the mean square local amplitude of the spin density $\left\langle S_L^2 \right\rangle$ for itinerant magnets similarly to the local moments for the localized state. Moriya has shown in his unified theory of 3*d*-electron magnetism that there are several temperature dependencies of $\left\langle S_L^2 \right\rangle$, as schematically shown on Fig. 1.1, depending on the strength of electron-electron correlations. For strongly correlated systems $\left\langle S_L^2 \right\rangle$ is non-zero above T_C and weakly increases with temperature. This gives mechanism for the Curie-Weiss magnetic susceptibility associated with spatially extended modes of spin-fluctuations instead of local moments as spatially localized spin fluctuations.

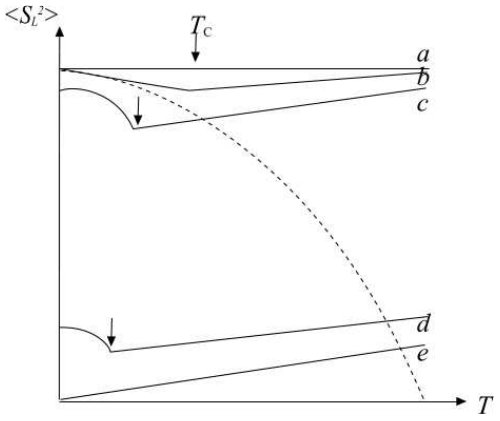

Fig. 1.1. Temperature dependencies of the local spin fluctuation amplitude. a) local moment; b) strongly correlated limit; c) invar type; d) weak itinerant-electron ferromagnet; e) exchange-enhanced Pauli paramagnet. Dashed curve represents a Stoner ferromagnet.

1.4. Magnetic properties of uranium intermetallics

Magnetic properties of uranium compounds cannot be described by one general theory, since the properties of actinides intermetallics are strongly dependent of the degree of the localization of 5*f* states. Moreover, in certain limits the 5*f* magnetism is in several aspects different than typical one for 3*d* or 4*f* systems. For the materials with localized 5*f* states exchange interactions can be seen as being analogous to regular lanthanides, for which the indirect exchange of the RKKY type is a good approximation. However, the actinide ions have less localized character than lanthanide ions. Consequently, 5*f* levels lay closer to the Fermi energy than the 4*f* levels, which results in the contribution of the 5*f* states in the metallic bonding. The other limit, systems with strongly itinerant 5*f* states (when direct 5*f*-5*f* overlap between neighbouring atoms plays a role), can be understood in terms of the Stoner-Edwards-

Wohlfarth theory for itinerant magnets, in which the ordering temperature is proportional to the ordered moment. An important difference between 5*f* and 3*d* systems is the ratio between the energy of the spin-orbit coupling, $\Delta_{S\text{-}O}$, and the energy width of the 3*d* (5*f*) band W_{3d} (W_{5f}). 5*f*-electron systems are characterized by narrower *f*-bands comparing to 3*d* bands, but on the other hand – the spin-orbit interaction is much larger in *f*-electron systems, of the order of eV. Due to the strong spin-orbit interaction, typically a large orbital magnetic moment μ_L is induced, which is antiparallel to the spin moment in light actinides.

For intermediate delocalization, when the 5*f*–5*f* overlap is very small, the role of 5*f*–ligand hybridization should be taken into account. It is a primary mechanism of destabilizing the 5*f* magnetic moments, but because the spin information is preserved in the hybridization process, it leads to indirect exchange coupling. Maximum ordering temperatures can consequently be expected for a moderate strength of hybridization, because a strong hybridization completely suppresses magnetic moments, whereas a weak one leaves the moment intact, but their coupling is weak.

In the compounds of uranium, the degree of localization is directly dependent on the inter-uranium spacing: if it increases enough for the narrowing of 5*f* band and consequent increase of the density of states at E_F, the Stoner criterion is fulfilled. For the uranium compounds the critical spacing was determined quantitatively and the value $d_{U\text{-}U}$ = 340-360 pm, called the Hill limit, is approximate boundary value of the spacing, corresponding to the critical overlap of 5*f* electronic wave functions. For smaller spacing the compounds are typically nonmagnetic (often superconducting). For $d_{U\text{-}U}$ larger than Hill limit they incline to a magnetically ordered ground state. The proximity of the compounds to the boundary between the magnetic and nonmagnetic state enhances dramatically the role of the atomic environment and coordination number.

But for compounds with $d_{U\text{-}U}$ larger than the Hill limit, the main control parameter is not the inter-uranium spacing, but the hybridizations of the 5*f* states with electronic states of other elements. This is essentially important for the compounds with the transition metals. The 5*f* states of strongly electropositive uranium remain pinned at E_F, whereas the late transition metals, being much more electronegative, have particular *d* states shifted toward higher binding energies, thus leaving the 5*f*–*d* overlap in energy scale small. Therefore, the 5*f* magnetism typically arises in compounds with the transition metal from the right end of a particular series. The magnetic moments of transition metals are mostly suppressed even for those *d*-metals, which are magnetically ordered in pure state, like cobalt, nickel or iron. Exceptions are the compounds in which *d*-magnetism prevails due to a very high content of the transition metal.

While moving to the left within the transition metal series the 5*f*–*d* overlap increases, leading typically to nonmagnetic ground-state. But in some cases magnetic moments appear both on uranium and transition metal atoms.

The model, which gave the most realistic results, was developed by Cooper et al. [7] on the basis of Coqblin–Schrieffer approach, describing the mixing of ionic *f*-states and conduction-electron states, in which the mixing term of the Hamiltonian of Anderson type is treated as perturbation, and the hybridization interaction is replaced by an effective resonant scattering in *f*-states. This approach leads to the fact that a population of the 5*f* states with orbital moments perpendicular to the bonding axis is observed. The interaction between two 5*f* ions prefers a strong ferromagnetic coupling of uranium atoms along the bonding direction, whereas there is no special general tendency for a weaker ferro- or antiferromagnetic coupling perpendicular to it. This has a serious impact on magnetic anisotropy of the compounds, which is typically much stronger for actinide compounds comparing to their lanthanides counterparts.

Since the spin–spin exchange interaction is essentially isotropic, it is magnetocrystalline anisotropy which orients magnetic moments in particular directions. Materials with uniaxial symmetry (hexagonal and tetragonal) have usually easy magnetization direction either parallel or perpendicular to the *c*-axis. The systematic studies of uranium intermetallics showed that in vast majority of cases the easy-magnetization direction is perpendicular to the nearest U–U links. If the uranium atoms form the network within the basal plane, the moments have to orient themselves perpendicular to the plane, yielding easy-axis anisotropy type. In an opposite case, if uranium atoms form separated linear chains, an easy-plane anisotropy appears.

To conclude, one can see that magnetic properties of uranium intermetallics are strongly dependent on the peculiarities of crystal structure (inter-uranium distances, atomic environment) and the electronic structure (the degree of *f*–ligand hybridization, the tendency for localization/ itinerancy). Any tiny modifications in these two parameters can lead to tremendous changes in magnetism and one of the available tools to achieve it is the introduction of hydrogen to the system.

2. Metal-Hydrogen Systems

The studies of hydrides should start from the definition what is a hydride. In the narrowest sense, this term is used just in cases when metal lattice is changed upon hydrogen absorption. However, we are going to use this term in broader sense. We will also define as

hydrides the compounds for which the hydrogen absorption leads to the modifications of the crystal structure, such as pure lattice expansion or the formation of the new structure, which is closely related to the original one. These compounds typically possess unique properties what allows to consider them as new materials. In short, we will designate all the phases of metal–hydrogen systems except for random interstitial solid solutions as hydrides. Hereafter we will make short review of metal–hydrogen binary phase diagrams and discuss the possible constituents – both metal hydrides and metal-based solid solutions of hydrogen. It should be also mentioned that due to metallic nature of hydrides, ordered structures are mostly stable around some stochiometric composition and the homogeneity range becomes wider as the temperature increases. Thus a certain degree of disorder is usually present in hydride phases [8].

2.1. Binary Diagrams of Metal–Hydrogen systems and Hydride Formation Criteria.

The phase diagrams of metal–hydrogen systems are often rather complicated and contain several ordered structures, especially at lower temperatures. The metal–hydrogen specimens differ essentially from the ordinary alloys formed of solid elements: we cannot change the temperature of a hydride specimen without consequent change of the composition. The exchange of hydrogen between a specimen and the surrounding atmosphere is of crucial importance in treating metal–hydrogen systems. The equilibrium concentration of hydrogen in a specimen is a unique function of the temperature T and pressure p of the surrounding H_2 gas.

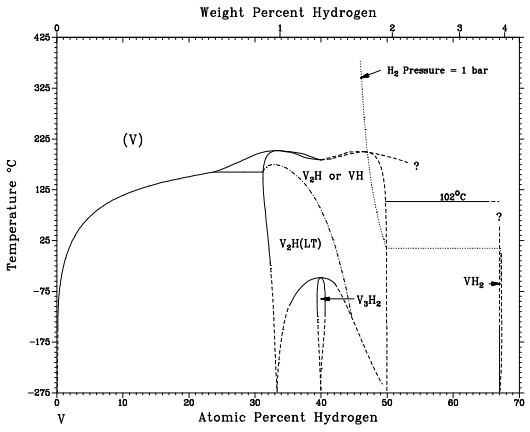

Fig. 2.1. Phase diagram of V–H system.

On Fig. 2.1, a binary phase diagram V–H [9] is presented as an example. This diagram shows the formation of the solid solution of hydrogen in vanadium, which is determined by linear variation of lattice parameters of the distorted vanadium matrix, and the formation of several vanadium hydrides with different structures [10]. The solubility of hydrogen in metal is described by the Sieverts law:

$$x \propto \sqrt{p} \qquad (2.1).$$

Since the temperature dependence of the solubility shows a thermal-activation type of behaviour, the overall expression for the solubility takes the form:

$$x = \sqrt{\frac{p}{p_0}} e^{\Delta S_S / k} e^{-\Delta H_S / kT} \tag{2.2}$$

ΔS_S is the entropy of solution referred to the H_2 gas of pressure p_0 and temperature T, and ΔH_S is the enthalpy (heat) of solution, k is the Boltzmann constant ($1.3806 \cdot 10^{-23}$ JK^{-1}).

The Sieverts law is followed at low concentrations of hydrogen. Hydrogen molecules are dissociated into atoms while getting dissolved in metals, and in region where gaseous hydrogen can be regarded as an ideal gas. At higher pressure, a deviation from ideal-gas behaviour makes the chemical potential for given p, T higher and, consequently, the solubility larger than the Sieverts law predicts. For example, the solubility at room temperature under 5 MPa of H_2 gas is enhanced by ≈ 3% due to the deviations from ideal-gas behaviour. At still higher pressures, the chemical potential of gaseous (fluid) hydrogen steeply increases, and gives rise to a very large enhancement of the solubility. At such regime the effects of interaction between hydrogen atoms should be considered.

Since it has been found that the enthalpy of solution is a function of hydrogen concentration, the reason should be the interaction between the dissolved atoms. The dependence of enthalpy on the hydrogen concentration can be presented as consisting of two parts – volume-dependent contribution and volume-independent one:

$$\frac{\partial \Delta H_S}{\partial x} = \left(\frac{\partial \Delta H_S}{\partial V} \right)_x \frac{\partial V}{\partial x} + \left(\frac{\partial \Delta H}{\partial x} \right)_V . \tag{2.3}$$

The first term can be estimated using the empirical relationship showing that volume per metal atom, v, increases linearly with hydrogen concentration:

$$v = v_0 + x v_H \tag{2.4}$$

where v_0 is the atomic volume of the pure host metal, and v_H is the volume increase per hydrogen atom. In many cases, v_H assumes a value close to $3 \cdot 10^6$ pm^3. Thus, the first term of Eqn. (2.3), called the elastic contribution, can be calculated as

$$\left(\frac{\partial \Delta H_S}{\partial V} \right)_x \frac{\partial V}{\partial x} \cong -K_0 \frac{v_H^2}{v_0} \equiv -u_{els} . \tag{2.5}$$

This assumes nearly a constant value for a given host metal because the bulk modulus K_0 usually depends only weakly on the hydrogen concentration. The elastic contribution to ΔH_S can be written then as $-u_{els}x$. The origin of the elastic contribution is the decrease in the pv_H term in the enthalpy when a negative pressure $p = -vH_x/v_0$ is produced, on an average, by the presence of hydrogen atoms.

The second term of Eqn. (2.3), including all volume independent contributions, can be called briefly as “electronic” contribution. This is a contribution coming mainly from the extra electrons brought into the lattice by hydrogen atoms. One may expect that the electronic contribution consists of a term that depends only on the total number of extra electrons and acts uniformly over the crystal, and the rest depends on local electronic states and becomes effective at shorter distances. The most primitive picture would suggest that the sole action of extra electrons is to fill the states at the Fermi level E_F of a rigid band of a host metal and then the mean-field contribution to ΔH_S can be written as $\int_0^x [N(E_F)]^{-1} dx$, where $N(E_F)$ is the density of states at E_F. However, more careful examination reveals that more sophisticated approach than simple band-filling picture is required and a short-range repulsion between hydrogen atoms has to be considered. Obviously, the interactions regarded should be those acting between more than two hydrogen atoms.

The many-body character of the interaction at high hydrogen concentrations was concluded by Oats and Stoneham [11], who showed that short-range elastic interaction energy for clusters of hydrogen atoms cannot be written as a sum of pair interactions. Further indication of short-range repulsive interaction can be demonstrated by empirical rule that in metal-hydrogen systems the hydrogen atoms cannot come closer to each other than 210 pm [12]. Another evidence is that the reduction of the partial configurational entropy has been noted in solid solution phases in comparison to what is expected for random distribution over all interstitial sites. Finally, the formation of ordered structures in practically all metal-hydrogen systems can also be regarded as proof for the short-range repulsion. If H–H interactions were attractive, precipitation of H-rich phases would be preferred at low temperatures instead of formations of ordered arrangements. The short-range repulsion should also give rise to short-range order in seemingly disordered solid-solution phases and, consequently, to diffuse scattering in diffraction experiments.

In the case of intermetallic hydrides, certain positions for hydrogen atoms are preferred. Fig. 2.2 presents some favourable positions on the example of three principal crystal structures (fcc, hcp, and bcc). Only two types of interstitial sites – octahedral (O) and tetrahedral (T) sites – are shown, because they are practically the only ones that are occupied by hydrogen atoms.

The number of interstitial sites per metal atom and the space available for these sites are given in Table 2.1.

In the crystal structure determination of hydrides, X-ray diffraction should be supplemented with neutron experiments (neutron diffraction or inelastic scattering) in order to locate the positions of hydrogen atoms. In most cases, neutron diffraction experiments were performed on deuterides because the coherent scattering cross section is much larger and incoherent cross section is much smaller in deuterium than in hydrogen. The site locations of hydrogen and deuterium atoms are mostly (but not necessarily) the same.

Table 2.1. Number and size of interstitial sites in the most common structures

Structure	*fcc* and *hcp* (*c*/*a* = 1.633)		*bcc*	
Site[a]	O	T	O	T
Number[b]	1	2	3	6
Site[c]	0.414	0.225	0.155	0.291

[a] O: octahedral sites, T: tetrahedral sites
[b] Number per metal atom
[c] Maximum sphere radius to be accommodated in interstitial space formed by metal atom spheres. In units of metal atoms radius.

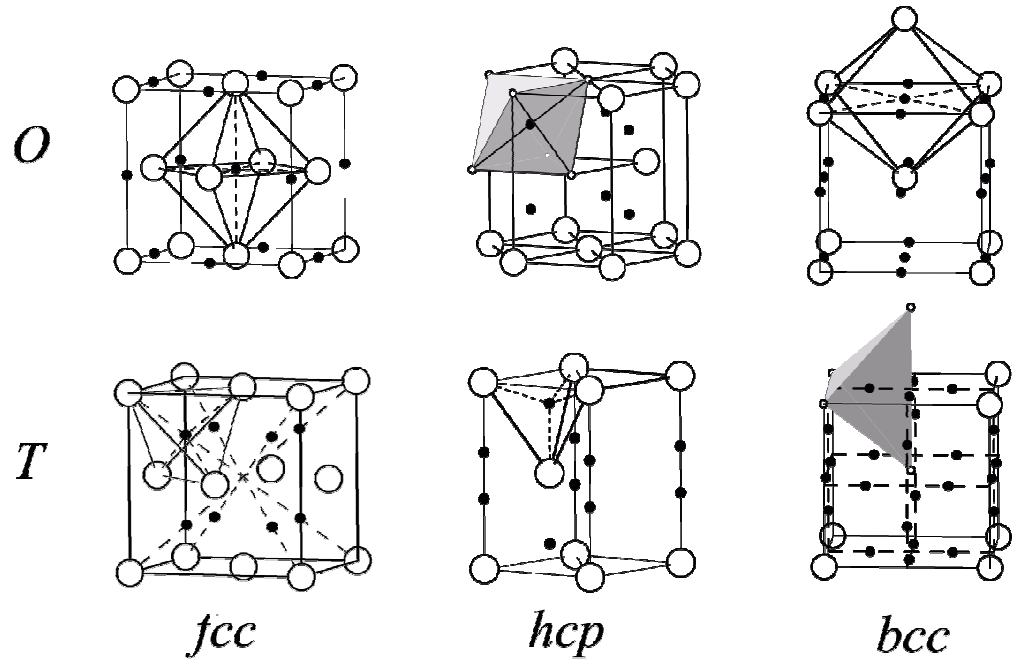

Fig. 2.2. Interstitial sites (octahedral (*O*) and tetrahedral (*T*)) in face-centred cubic (*fcc*), hexagonal closed-packed (*hcp*) and body-centred cubic (*bcc*) structures. The interstitials are shown as black dots.

To conclude, we should review the criteria, which are to be fulfilled to make the hydride formation favourable. Hydrogen absorption by intermetallics at hydrogen pressure below 100 bar at room temperature requires the presence of hydride-forming element. No exception is known to this "rule". Geometrical requirements include sufficient size for the interstitials and their arrangement in space. The well-known Westlake's criterion states that available interstitial sites must have a spherical volume with radius ≥ 40 pm [13-17]. As it was discussed above, the minimum H-H distance should be 210 pm. Besides, according to the "Shoemaker's exclusion rule" two tetrahedra sharing the same face cannot be occupied simultaneously [18-20]. Despite the simplicity of these rules they provide good ground for the preliminary estimate of the probability of the formation of stable hydride. However one should keep in mind that there are always some exceptions from these rules due to the fact that the stability of the hydride is determined by many factors and none of them predominates in all cases. For example, it was shown that UPd_3, which fulfils all the requirements listed above, absorbs just a negligible amount of hydrogen [21]. The correlation between the bonding strength in the intermetallic lattice and the corresponding hydrogen absorption capacities was analysed and it was shown that besides the geometrical considerations, the stabilities of the parent intermetallic compounds is another factor which determines the possibility of hydrogen absorption [22]. Possible hydrogen absorption has to be therefore established experimentally.

2.2. Effect of Hydrogenation on the Electronic Structure and Magnetism

One of the common features of the electronic structures of metal hydrides is the formation of hydrogen-induced states below E_F of a metal that can be filled with added electrons [12]. Hybridization of the valence states with the *s*-states of hydrogen lowers in energy of the electronic states of *s*-symmetry in a host metal – each hydrogen atom added lowers one band that is partially filled. The states formed in this way are of bonding character. The same number of antibonding states brought by hydrogen is expelled to higher energies above the Fermi level.

The electronic structure calculations showed that the modifications of density of states strongly depend on the hydrogen site symmetry. For example, it was shown that for some compounds the filling of the octahedral sites leads to more pronounced changes comparing to the tetrahedral sites [23]. Another important parameter, which defines the character of band structure modifications, is the mutual arrangement of hydrogen atoms. It was shown [12] that the new states induced below E_F are very sensitive to H-H distances and their position depends on the proximity of hydrogen atoms to one another. This finding, discussed by Switendick,

contributed to the confirmation of the geometrical criterion stated above about the existence of the minimum H-H distance 210 pm.

The changes of band structure due to hydrogenation lead to changes of magnetic properties and this is in particular pronounced for compounds of 5*f* elements [24]. In some cases it is possible even to describe the influence of hydrogen presenting it as purely negative pressure agent. From this point of view, hydrogenation leads to the narrowing of electronic bands and, consequently, to the increase of magnetic moments and/or decrease of the degree of hybridization of magnetic electrons with ligand atoms or, in certain cases, with the atom of the same type. On the contrary, magnetic moments of regular lanthanides, where in many cases the magnetic 4*f* electrons form ionic-like states, as a rule remain intact upon hydrogenation, and magnetic studies of hydrides indicate mainly the impact on exchange interactions. The increase of inter-atomic spacing in rare-earths intermetallics may affect the magnetic exchange not through the shrinking of a band width but mainly through modification of the RKKY-type exchange, typically mediating 4*f*-4*f* interactions. An exception is anomalous rare-earths (as Ce) [25-26], which have the 4*f* states close to E_F and the band picture can be considered. More pronounced changes are observed for valence fluctuators in which the hydrogenation can stabilize the valency and lead to a magnetic state.

The finding of the formation of UH_3 is an obvious case proving how dramatic changes upon hydrogenation might occur in the actinide compounds. Metallic uranium crystallizes with orthorhombic structure type (space group *Cmcm*) and does not show magnetic ordering, being weak Pauli paramagnet with the value of magnetic susceptibilit $\chi = 4.9\times10^{-9}$ m^3/mol at room temperature. Two modifications of UH_3 hydride were reported. Both α-UH_3 (low temperature modification) [27] and β-UH_3 (high temperature modification) [28-29] crystallize with cubic *Pm3n* space group. Crystal structure of α-UH_3 can be considered as simple *bcc* packing of uranium atoms each surrounded by an icosahedron of the atoms of hydrogen. Therefore uranium atoms are separated in space and the lattice is held mainly by metal-hydrogen bonds. α-UH_3 is a ferromagnet with ordering temperature between 174 and 178 K. However, α-UH_3 phase is difficult to prepare and it frequently contains a mixture of α- and β-phases [30]. Crystal structure of β-UH_3 consists of two uranium sublattices. One uranium sublattice forms a *bcc* structure of widely spaced presumably magnetic metal atoms similar to what was observed for α-phase, whereas the second sublattice builds infinite chains of closely spaced uranium atoms, two in each cube phase. The metal-metal distance in the face chains is only 3.31 Å, and band calculations showed that there should be major *f*-*f* overlap of the 5*f* functions for this distance,

whereas the *bcc* sublattice seems to be the most likely candidate for local magnetic moments. β-UH_3 is also a ferromagnet with T_C in the range between 170 and 181 K. The measured paramagnetic moment μ_{eff} = 2.44-2.97 μ_B is below the expected value for the localized $5f^3$ (U^{+3} – 3.62 μ_B) or $5f^2$ (U^{+4} – 3.58 μ_B) state. It was shown by calculations that both α-UH_3 and β-UH_3 structures favor *f*-electron bonding with the hydrogen states, β-UH_3 more so than α-UH_3 [31]. The photoemission studies indicated the itinerant character of magnetism in UH_3 [32]. Due to the lack of saturation, the data of spontaneous moment for β-UH_3 exhibit a considerable scatter (0.87 μ_B – 1.18 μ_B), while the neutron diffraction gives a moment of 1.39 μ_B [24]. This is obviously a consequence of rather high magnetic anisotropy. The electronic specific heat coefficient of β-UH_3 (γ= 28.5 mJ/mol K^2 [33]) is nearly by a factor of three larger than that of metallic uranium. By analogy with Ce hydrides, this γenhancement may presumably arise from a correlation effect as in heavy fermion systems rather than from a simple increase of the density of states at the Fermi energy.

3. U*TX* and U_2T_2X Compounds: State of the Art

As it has been shown above, hydrogenation has tremendous effect on the magnetism of pure uranium metal. However, even more fascinating results can be expected while moving towards more complicated systems, *i.e.* uranium-based intermetallic compounds. The existence of large groups of isostructural compounds makes it possible to study systematically the influence of even tiny changes of electronic structure, by changing the environment of uranium atoms and fixing structure parameters. Hydrogenation brings additional variable to the system by volume expansion and with another electron contributed. The resulting effects are frequently helpful for better understanding of the nature of interactions in initial compounds and may lead to the formation of new compounds with qualitatively new properties.

3.1. UTX Compounds

U*TX* compounds (*T* – transition metal, *X* – p-element) form the largest group of isostoichiometric uranium ternaries. The majority of U*TX* compounds crystallize with either hexagonal ZrNiAl structure type or orthorhombic TiNiSi structure type (Fig. 3.1). ZrNiAl (space group $P\bar{6}2m$, atomic positions U – 3*g* (x_U; 0; 0.5); T_1 – 1*b* (0; 0; 0.5); T_2 – 2*c* (1/3; 2/3; 0); *X* – 3*f* (x_{Sn}; 0; 0)) is derived from binary Fe_2P structure type and is a typical layered structure. U–*T* and *T*–*X*

layers, lying in the basal plane, alternate along the *c*-axis. Each uranium atom has four nearest uranium neighbours within the U–*T* layer and U–*T* layers are separated by the lattice parameter *c*. This structure type is mostly encounterd for *X* standing for aluminum, gallium and tin. TiNiSi structure type (space group *Pnma*, atomic positions U – 4*c* (x_U; 0.25; z_U); *T* – 4*c* (x_T; 0.25; z_T); *X* – 4*c* (x_X; 0.25; z_X)) is an ordered variant of binary $CeCu_2$ structure type and is presented on Fig. 3.1, too. More detailed analysis shows that this structure can be easily derived from hexagonal AlB_2 structure by displacement-disorder transformations. TiNiSi structure is typical for U*T*Si and U*T*Ge compounds.

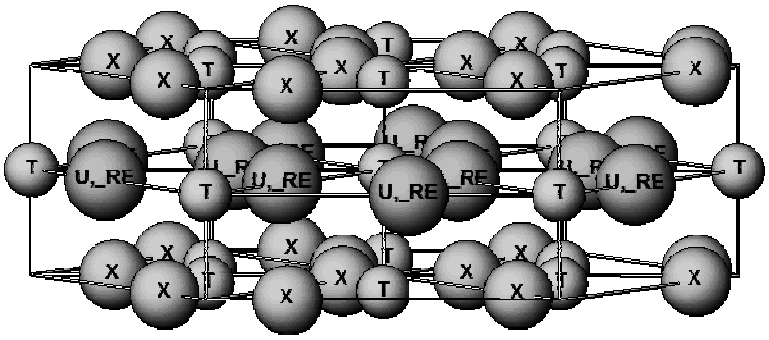

(*a*)

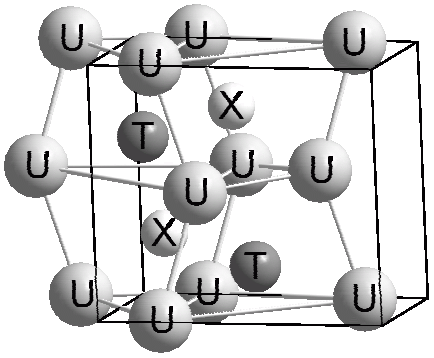

(*b*)

Fig. 3.1. Schematic representation of ZrNiAl (*a*) and TiNiSi (*b*) structure types

U*TX* compounds show large variety of magnetic properties. The compounds crystallizing with ZrNiAl structure type are characterized by a rather high magnetic anisotropy. The close packing within the basal plane leads to non-negligible 5*f*-5*f* overlap and to strong 5*f*-*d* hybridization. As a consequence, a strong ferromagnetic coupling of the involved U magnetic moments appears. In order to estimate the type of interactions along the *c*-axis both, the 5*f*-*d* (U-*T*) and 5*f*-*p* (U-*X*) hybridization should be taken into account. In case the former prevails a ferromagnetic coupling would rather occur and if the latter – antiferromagnetic.

UCoSn crystallizes in the ZrNiAl structure type with lattice parameters a = 714.8 pm, c = 399 pm [34] (a = 715.3 pm, c = 400.1 pm [35]). It is a stable U-moment ferromagnet below T_C = 80-88 K [35-38]. The strong magnetic anisotropy with magnetic moments oriented along the *c*-axis was found. The magnetic moment of uranium atoms, estimated from the single crystal magnetization measurements, reaches 1.2 μ_B/f.u. [39].

URuSn also crystallizes with ZrNiAl structure type with lattice parameters a = 736.9 pm and c = 396.1 pm [35]. It orders ferromagnetically below T_C = 51-55 K [38, 40-42] with a spontaneous uranium magnetic moment of 1.1 μ_B/f.u. Similar to UCoSn, it is characterized by strong uniaxial anisotropy with the *c*-axis as the easy magnetization direction.

For both UCoSn and URuSn ^{119}Sn Mössbauer spectroscopy data have been reported [40, 43]. It was shown that the direction of magnetization coincides with the crystallographic *c* axis for both compounds, and the principal axes of the electric field gradient tensor were determined with respect to the crystallographic axis. For UCoSn the V_{yy} component is parallel to the *c* axis while in the case of URuSn, the V_{zz} component is parallel to this axis.

The studies of the solid solution $UCo_{1-x}Ru_xSn$ were reported in Ref. 44. Ferromagnetism is observed through the whole $UCo_{1-x}Ru_xSn$ composition range with T_C nearly constant (≈ 80 K) for $x < 0.6$ and gradually decreasing with further increasing x. The spontaneous magnetic moment first increases up to 1.5 μ_B/f.u. at x = 0.5, which is followed by a decrease with further increase of Ru concentration. Variations of the lattice parameters are non-monotical and exhibit considerable deviations from the Vegard's law. At x = 0.6, the dependence of the parameter a shows clearly the change of the slope and the parameter c passes through a minimum. This observation led to an assumption that Ru atoms first occupy the 2*c* site and only then – the 1*b* site.

UCoSi was firstly reported to crystallize with orhtorhombic $CeCu_2$ structure type. Later it was recognized that it is in fact the TiNiSi structure type, representing the ordered ternary variant of the former. There is a certain scatter of the values of lattice parameters in the literature and they are within the range a = 683.9-685.2 pm, b = 410.2-411.9 pm, c = 704.9-714.3 pm [45-49]. UCoSi is paramagnetic at least down to 1.4 K. The high field magnetization at T = 4.2 K is practically linear up to 35 T reaching 0.12 μ_B/f.u. at this field [50]. No anisotropy was observed for this compound, which is an indication of lack of magnetism connected with the uranium 5*f*-electrons.

3.2 U_2T_2X compounds

Large group of isostructural U_2T_2X compounds crystallizes with tetragonal structure of the Mo_2FeB_2 structure type (space group *P4/mbm*, atomic positions U – 4*h* (x_U; x_U+0.5; 0.5); *T* – 4*g* (x_T; x_T+0.5; 0); *X* – 2*a* (0; 0; 0)), which is an ordered variant of binary U_3Si_3 type (Fig. 3.2) [51]. The crystal structure can be presented as a packing of distorted fragments of AlB_2 and CsCl simple structures, which form the network of octahedra and trigonal bipyramids (consisting of two tetrahedra sharing a face), all forming interstitials favourable for hydrogen allocation. The structure consists of two alternating layers separated by the distance of *c*/2. One layer at *z* = 0.5 consists exclusively of uranium atoms, and another contains *T* and *X* atoms. Each uranium atom has two nearest uranium neighbours separated by lattice parameter *c* and one in the basal plane. These distances are typically not much smaller than 3.5 Å, which allows the formation of uranium magnetic moments. The direction of the shortest inter-uranium distance (along *c*-axis or in the basal plane) varies for different compounds of the U_2T_2X series, following apparently the rule that uranium moments should be perpendicular to the shortest U–U link. The orientation of the uranium magnetic moments is not the same for all compounds (Table 3.1). Since the inter-uranium distance for most compounds out of the series is not the restricting parameter for the formation of magnetically ordered structures, it is the 5*f*-*d* hybridization which is the controlling parameter that determines the existence of magnetic order

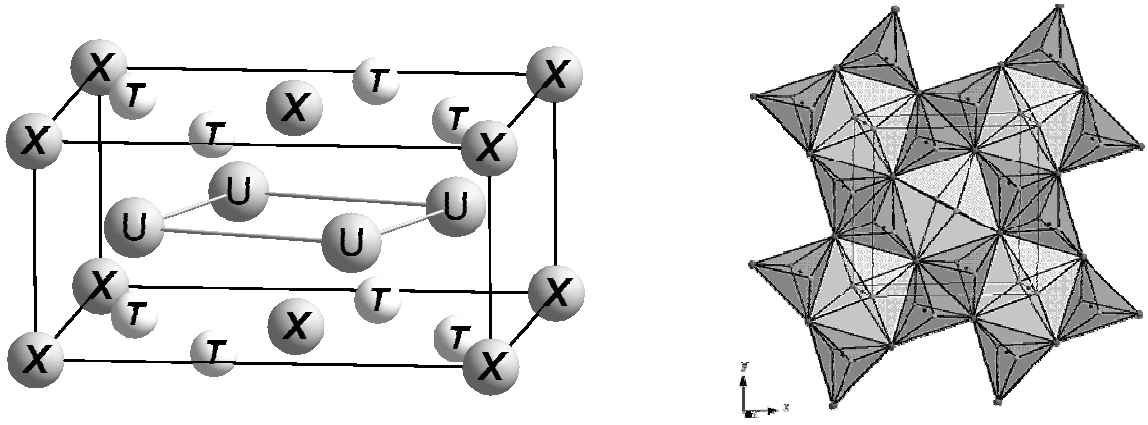

(*a*) (*b*)

Fig. 3.2. Schematic representation of Mo_2FeB_2 structure type (*a*) and the arrangement of interstitials within this structure type (*b*). Light grey parts show CsCl fragments, dark – AlB_2.

The binary prototype U_3Si_2 is a non-magnetic spin-fluctuator [52] due to the proximity of the nearest uranium atoms. However, if one of the two positions of uranium atoms is occupied

by non-transition metal like In or Sn, and Si position is occupied by a transition metal, the picture is changed dramatically. The magnetic order in the U_2T_2X series changes from 5*f*-antiferromagnetism to weak paramagnetism, with a heavy-fermion behaviour on the verge of magnetism [53]. The driving force of these changes is the increase of the hybridization strength, what is reflected by the fact that magnetically ordered compounds are formed with the transition metals from right-hand side of the transition metal series of the periodic table, while moving through periodic table to the left – the tendency for the magnetic order vanishes. This makes the U_2T_2X compounds very sensitive to the lattice and electronic structure modifications, what can be easily achieved by hydrogenation.

Table 3.1. Basic characteristics of selected U_2T_2X compounds. *a*, *c* – lattice parameters at room temperature; $d_{\perp c}$ – interuranium spacing within the basal plane; the ground state magnetic properties are defined as AF for antiferromganetic, SF for spin-fluctuator, WP for weakly paramagnetic state; T_N – magnetic ordering temperature. The inter-uranium distance along *c*-axis is equal to the lattice parameter *c*. The shortest inter-uranium distance is starred.

Compound	*a* (pm)	*c* (pm)	$d_{\perp c}$ Å	Type	T_N (K)	γ(mJ/(mol K^2))	Ref
U_2Ni_2Sn	726.3	369.1	3.581*	AF	26	172	[53-56]
U_2Ni_2In	737.4	357.2*	3.602	AF	14	206(350)	[51, 53, 57, 58]
U_2Co_2Sn	728.9	350.5*	3.531	SF	-	250	[53, 56]
U_2Co_2In	736.6	343.2*	3.530	WP	-	32	[51, 53]
U_2Fe_2Sn	729.6	344.6*	3.500	WP	-	-	[59]
U_2Pd_2In	763.7	375.2*	3.767	AF	37	393	[51, 60]

U_2Ni_2Sn is an antiferromagnet with T_N = 26 K. In the paramagnetic region the magnetic susceptibility is described by a modified Curie-Weiss law with the parameters μ_{eff} = 2.3 μ_B/U, θ_P = -110 K, and $\chi_0 = 1.8 \cdot 10^{-8}$ m^3/mol [57, 53]. The magnetization curve (at T = 4.2 K) shows three metamagnetic transitions at 30, 39, and 51 T and reaches the value of magnetization 1.3 μ_B/f.u. in 57 T [55]. Neutron powder diffraction and Mössbauer spectroscopy experiment were performed in order to determine the magnetic structure [54]. ^{119}Sn Mössbauer spectroscopy at 4.2 K shows that Sn atoms experience a zero magnetic hyperfine field, what agrees well with proposed magnetic order – an antiferromagnetic structure with a propagation vector $\boldsymbol{q}$ = (0, 0, 1/2) and antiferromagnetic coupling also within the basal plane with uranium moments μ_U = 1.05 μ_B (at T = 1.5 K). However, later single-crystal neutron diffraction study seemed to indicate the *c*-axis orientation of magnetic moments [61].

U_2Ni_2In is an antiferromagnet with T_N = 14.3 K. The paramagnetic susceptibility is described by the Curie-Weiss dependence with μ_{eff} = 2.0 μ_B/U. and θ_P = -80 K [57]. The magnetization curve shows a broad S-shape centered at 27 T, which was tentatitevely attributed to a change in the magnetic structure [62]. The enhanced value of specific heat coefficient γ points to a strongly itinerant character of magnetism, which is still underlined by low magnetic entropy of only 0.4*R*ln2 [57, 58]. A neutron diffraction experiment showed a non-collinear structure with uranium moments of 0.60 μ_B (at T = 10 K) oriented along equivalent <110> directions and coupled antiferromagnetically between the adjacent plane layers. Thus the magnetic unit cell is twice larger comparing to the crystallographic one [58, 63].

U_2Co_2Sn was found to be non-magnetic, but with strong ferromagnetic spin-fluctuation features and exhibiting non-Fermi liquid behaviour. The temperature dependence of magnetic susceptibility is described by a modified Curie-Weiss law with μ_{eff} = 1.5 μ_B/U, θ_P = 51 K, and a relative large $\chi_0 = 2.3 \cdot 10^{-8}$ m^3/mol f.u., and it is strongly field-dependent below T = 10 K. The pronounced upturn of the low-temperature specific heat, leading to the enhanced value of γ= 250 mJ/(mol f.u. K^2) [53], was a attributed to spin-fuctuation effects. Besides, they were also responsible for the high slope of the resistivity curve at low temperatures and for its approach to saturation in the high temperature range [64, 65]. More detailed analysis was presented in Ref. 66 based on the specific heat, resistivity and magnetic susceptibility measurements and it clearly identifies U_2Co_2Sn as a non-Fermi-liquid system.

U_2Co_2In and *U_2Fe_2Sn* are also non-magnetic compounds and show rather similar behaviour. U_2Co_2In is weakly paramagnetic with susceptibility about $6 \cdot 10^{-8}$ m^3/mol f.u. in the low temperature limit and γ= 32 mJ/(mol f.u. K^2) [53, 57]. Very little information is available on U_2Fe_2Sn. It is just known that it is a Pauli paramagnet and the electrical resistivity shows only a weak saturation tendency at high temperatures [67].

U_2Pd_2In orders antiferromagnetically at T_N = 37 K. The uranium moments of 1.6 μ_B are oriented along equivalent <110> directions and are coupled ferromagnetically between the layers [60, 63]. The studies on the single crystals [68] revealed that the paramagnetic susceptibility for magnetic fields applied along the *c*-axis is much smaller than for the fields applied within the basal plane. For both directions the paramagnetic susceptibility can be described by a modified Curie-Weiss law with the parameters μ_{eff} = 3.0 μ_B/U, θ_P = -125 K and $\chi_0 = 0.9 \cdot 10^{-8}$ m^3/mol f.u. for field parallel to *c*-axis, and μ_{eff} = 2.5 μ_B/U, θ_P = -23 K and $\chi_0 = 2.0 \cdot 10^{-8}$ m^3/mol f.u. for field applied in the basal plane. The specific heat shows pronounced magnetic anomaly at T = 36 K

and a low temperature upturn which can be fitted using the additional spin-fluctuation term and leading to γ= 393 mJ/(mol f.u. K^2).

3.3. Hydrides of Uranium Ternaries

So far the broad investigation of hydrogen absorption properties of uranium ternaries comprised mainly U*TX* compounds (*T* – transition metal, *X* – *p*-element). Antiferromagnetic UNiAl was the first compound among equiatomic uranium ternaries, crystallizing with the hexagonal ZrNiAl structure type, found to absorb hydrogen. Several UNiAl-based hydrides with different hydrogen content were reported [69-73]. The structure parameters of the synthesized hydrides of UNiAl are listed in Table 3.2. Although UNiAl is an antiferromagnet with T_N = 19 K, the range of hydrides with orthorhombic structure (space group *Pnma*) with a hydrogen content up to 0.58 H at./f.u. does not show magnetic ordering down to 2 K. The hydride with a higher hydrogen content, hexagonal $UNiAlH_{0.7}$, shows ferromagnetic ordering below 87 K. Further hydrogenation results in the recovering of antiferromagnetic ordering, the Néel temperature for $UNiAlH_{2.3}$ is 99 K [74].

Table 3.2. Structure parameters od $UNiAlH_x$ hydrides: lattice parameters *a*, *b* and *c*, and volume per formula unit *V*.

Compound	Structure type	*a* (pm)	*b* (pm)	*c* (pm)	*V* (10^7pm^3)
UNiAl	Hexagonal	673.47	-	403.71	5.286
$UNiAlH_{0.06}$	Orthorhombic	705.8	392.0	743.4	5.142
$UNiAlH_{0.14}$	Orthorhombic	700.8	393.4	747.0	5.149
$UNiAlH_{0.58}$	Orthorhombic	672.2	413.0	790.4	5.486
$UNiAlH_{0.70}$	Hexagonal	699.09	-	399.10	5.631
$UNiAlH_{2.30}$	Hexagonal	718.44	-	402.44	5.996

The structure studies on deuterides $UNiAlD_{0.7}$ and $UNiAlD_{2.2}$ were performed for the determination of deuterium positions [75]. In $UNiAlD_{0.7}$ all deuterium atoms are located inside the polyhedra of 3U–2Ni type, consisting of two [U_3Ni] tetrahedra sharing a face, near the center of a triangular formed of uranium atoms expanding these triangulars. Further expansion leads to additional hydrogen absorption inside another 3U–2Ni and 3U–2Al polyhedra and formation of $UNiAlD_{2.2}$. Two more partly occupied deuterium positions are located around a midpoint connecting two uranium atoms along the *c*-axis.

It was found out that in the family of U*TX* aluminides the hydrogen absorption is limited to *T* = Ni. It can be illustrated by the studies of hydrogen absorption properties of $U(Fe_{1-x}Ni_x)Al$ series of compounds [76, 77], for which hydrogen absorption was not registered for *x* below ≈ 0.7. $U(Fe_{0.3}Ni_{0.7})Al$ absorbs at most 0.8 hydrogen atoms per formula unit, preserves ferromagnetic type of order and in hydrogenated state shows much higher values of ordering temperature, paramagnetic Curie temperature and the uranium magnetic moment comparing to non-hydrogenated compound. $U(Fe_{0.15}Ni_{0.85})Al$ absorbs 2.4 hydrogen atoms per formula unit similar to UNiAl and hydrogenation induces antiferromagnetic order in nonmagnetic initial intermetallic below ≈ 70 K. In both cases mentioned above hydrogenation leads to the reduction of 5*f*-3*d* hybridization and localization of uranium 5*f* electrons. Lower hydride $U(Fe_{0.15}Ni_{0.85})AlH_{0.6}$ crystallizes with orthorhombic structure and exhibits no magnetic order, similar to the lower hydrides of UNiAl (Table 3.3).

Table 3.3. Basic structure and magnetic characteristics of $U(Fe_{1-x}Ni_x)Al$ compounds and respective hydrides.

Compound	Structure type	Ground state	T_N, T_C (K)
$U(Fe_{0.15}Ni_{0.85})Al$	hexagonal	non-magnetic	-
$U(Fe_{0.15}Ni_{0.85})AlH_{0.6}$	orthorhombic	non-magnetic	-
$U(Fe_{0.15}Ni_{0.85})AlH_{2.4}$	hexagonal	antiferromagnetic	70
$U(Fe_{0.3}Ni_{0.7})Al$	hexagonal	ferromagnetic	15
$U(Fe_{0.3}Ni_{0.7})AlH_{0.8}$	hexagonal	ferromagnetic	90

U*T*Si compounds crystallizing with orthorhombic TiNiSi structure type were inspected for hydrogen absorption too [78]. Two hydrides $UNiSiH_{2.0}$ and $UPdSiH_{2.0}$ were studied. For all these compounds hydrogenation results in the increase of the lattice symmetry from orthorhombic to hexagonal (ZrBeSi structure type) (Table 3.4). $UPdSiH_{2.0}$ orders antiferromagnetically at T_N = 46 K compared to T_N = 31 K for UPdSi, but it shows only one field-induced transition ($\mu_0 H_c$ = 6.8 T at 4.2 K), whereas UPdSi undergoes two of them (at 4 T and 7 T). $UNiSiH_{2.0}$ is a ferromagnet with T_C = 98 K, whereas UNiSi is an antiferromagnet with T_N = 85 K. The number of magnetic phases remains unchanged, *i.e.* 3, in the UNiSi–H system. The observed changes are attributed to the increased inter-uranium spacing in the hydrides.

Table 3.4. Structure parameters of UPdSi, UNiSi, and respective hydrides: lattice parameters *a*, *b* and *c*, and volume per formula unit *V*.

Compound	Structure type	*a* (pm)	*b* (pm)	*c* (pm)	V (10^7pm^3)
UPdSi	Orthorhombic	702.6	420.5	767.0	5.665
$UPdSiH_{2.0}$	Hexagonal	417.7		799.5	6.039
UNiSi	Orthorhombic	695.2	412.7	705.5	5.060
$UNiSiH_{2.0}$	Hexagonal	403.2		777.6	5.474

High-pressure and high-field studies were performed both for $UPdSiH_{2.0}$ and $UNiSiH_{2.0}$ [79]. High-field magnetization measurements revealed an antiferromagnetic ground state in $UPdSiH_{2.0}$ and uncompensated antiferromagnetic one in $UNiSiH_{2.0}$ since a metamagnetic transition was found at 11.8 T. Two subsequent magnetic phases in $UNiSiH_{2.0}$ are ferromagnetic. High-pressure measurements showed an increase of T_N in $UPdSiH_{2.0}$ with pressure and significant decrease of T_C for $UNiSiH_{2.0}$. However, the estimate of the ordering temperatures in $UNiSiH_{2.0}$ based on the bulk moduli indicates that the pressure effect on magnetism in the hydrides goes beyond the simple volume effect.

4. Sample Preparation and Experimental Techniques

4.1. Hydrides Synthesis

The synthesis of hydrides was preceded by the preparation of respective intermetallic compounds. The samples were prepared by arc-melting of the stoichiomeric amount of metals of purity at least 99.9% under argon atmosphere. The check of the composition was performed preliminary by the estimation of weight losses and further by X-ray analysis.

Afterwards the ingot was crushed in to submillimeter particles and loaded in the reactor for hydrogenation. Fig. 4.1 shows a scheme of the hydrogenation equipment. Prior to hydrogenation, the surface of the powder was activated by heating up to T = 523 K for 2 hours in oil-free vacuum ($p < 1 \cdot 10^{-6}$ mbar) in order to desorb surface contaminants. The direct dependence was found between the quality of vacuum and the rate of the hydrogenation [80]. Hydrogenation was performed by exposing an activated material to H_2 (D_2) and subsequent thermal treatment. The synthesis conditions for every type of sample were optimized. The maximum pressure applied was 120 bar and the thermal cycling up to 923 K was performed. Under such conditions, hydrides of UCoSn, URuSn, $UCo_{1-x}Ru_xSn$, UCoSi, U_2Ni_2Sn, U_2Ni_2In, U_2Co_2Sn, U_2Co_2In, U_2Fe_2Sn, and U_2Pd_2In compounds were synthesized. Moreover, the hydride with lower hydrogen content for U_2Co_2Sn was synthesized at the hydrogen pressure of 35 bar and T = 773 K. It was observed for the U_2T_2X compounds that higher temperatures of synthesis lead to the partial decomposition of the sample and subsequent formation of UH_3 as spurious phase. Therefore for the U_2T_2X compounds, temperatures not higher than 773 K were applied, while the exposition time was extended. Hydrogen absorption was registered by a pressure drop, however

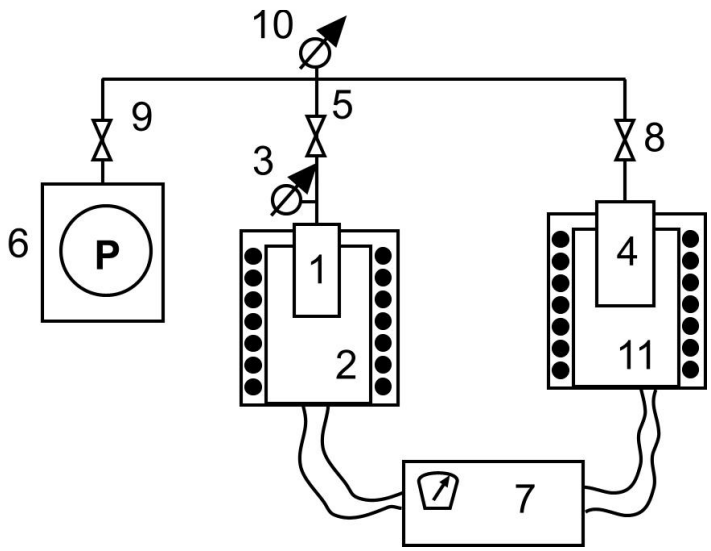

Fig. 4.1. The scheme of hydrogenation equipment: 1 – reactor; 2, 11 – furnaces; 3, 10 – vacuummeters; 4 – $LaNi_5$ container with H_2 or D_2; 5, 8, 9 – valves; 6 – vacuum pump; 7 – temperature control unit.

at such relatively high pressures it was impossible to determine the stoichiometry of the hydride with an acceptable accuracy (due to the thermal drift of the high-pressure gauge, etc.). To quantify the amount of absorbed hydrogen, samples of hydrides (typical mass 100 mg) were decomposed in vacuum in closed volume by heating up to 1173 K. By the amount of hydrogen released the stoichiometry of the hydride was determined. The error bar of the hydrogen content determined by volumetric method depends on the amount of the sample decomposed and typically does not exceed ±0.1 H/f.u. The synthesized hydrides were in a form of fine brittle powder, which might cause many undesirable problems, including high pyrophoricity, decreasing thermal conductivity or high risk of contamination [81]. Consequently, we were restricted in the further analysis to X-ray powder diffraction, neutron diffraction, magnetic measurements on randomly oriented powder, and Mössbauer spectroscopy. Additional treatment was necessary to make samples suitable for specific heat measurements.

4.2. X-ray Diffraction Studies and Crystal Structure Refinement

X-ray analysis was used for sample characterization and phase analysis: the diffraction patterns of intermetallic compounds were taken before and after hydrogenation. The data were collected on Siemens D500 (Co-K_α radiation), XRD-3003 (Seifert) and HZG-3 (both Cu-K_α radiation) diffractometers in a step regime (step 0.02º-0.05º of 2θ). The X-ray analysis is based on the on the properties of X-rays to penetrate to the matter and to scatter on the electrons with consequent diffraction. The diffraction can be considered as the reflection of X-ray beam from the atomic planes of the crystal and can be described by the Bragg law:

$$2d\sin\theta = n\lambda$$

where n – an integer, called the order of reflection;

d – the interplanar distance;

θ – an angle of reflection;

λ – wavelength of radiation.

The phase analysis was based on the comparison of the obtained patterns with the theoretically calculated ones (Powder Cell 2.4 software [82]) of the existing binary and ternary compounds and pure elements.

The crystal structure refinement, based on the analysis of X-ray powder patterns obtained in step regime, provides information on lattice parameters, atomic coordinates, coefficients of the

occupancy of particular positions, overall or individual isotropic thermal parameters. Moreover, it can give approximate estimate of strain and stress effects. A number of computing programs are applied for this purpose, which are based on the Rietveld algorithm [83], including FullProf software suite [84] by J. Rodriguez-Carvajal [85], which was used in the present work. This method allows the refinement of up to 8 phases simultaneously.

In the Rietveld refinement a mathematical model is assumed to represent the experimental pattern. In particular, when a structural model is available, then the intensity y_{io} observed at the ith step may be compared with the corresponding intensity y_{ic} calculated via the model. According to Rietveld, the model may be refined by minimizing by a least-squares process the residual

$$S = \sum w_i \left| y_{io} - y_{ic} \right|^2 \qquad (4.1),$$

where w_i, given by

$$\left(w_i\right)^{-1} = \sigma_i^2 = \sigma_{ip}^2 + \sigma_{ib}^2 , \qquad (4.2)$$

is a suitable weight. σ_{ip} is the standard deviation associated with the peak (usually based on the counting statistics) and σ_{ib} is that associated with the background intensity y_{ib}.

y_{ic} is the sum of the contributions from the neighbouring Bragg reflections and from the the background:

$$y_{ic} = s \sum_k m_k L_k \left| F_k \right|^2 G(\Delta\theta_{ik}) + y_{ib} , \qquad (4.3)$$

where s is a scale factor, L_k is the Lorentz-polarization factor for the reflection k, F_k is the structure factor, m_k is the multiplicity factor, $\Delta\theta_{ik} = 2\theta_i - 2\theta_k$, where $2\theta_k$ is the calculated position of the Bragg peak corrected for the zero-point shift of the detector, and $G(\Delta\theta_{ik})$ is the reflection profile function.

The parameters to adjust by refinement include unit cell, atomic positional and thermal parameters, and parameters defining the functions G and y_{ib}.

The quality of the agreement between observed and calculated patterns is measured by a set of the following nowadays conventional factors, based on Eqn. (4.1):

1. the profile $R_p = \sum \left| y_{io} - y_{ic} \right| / \left(\sum y_{io} \right)$;
2. the weighted profile $R_{wp} = \left[\sum w_i \left(y_{io} - y_{ic} \right)^2 / \sum w_i y_{io}^2 \right]^{1/2}$;
3. the Bragg $R_B = \sum \left| I_{ko} - I_{kc} \right| / \left(\sum I_{ko} \right)$. The values I_{ko} are obtained by partitioning the raw data in accordance with the I_{kc} values of the component peaks;

4. the expected $R_E = \left[(N-P)/\left(\sum w_i y_{io}^2\right)\right]^{1/2}$, where N and P are the number of profile points and refined parameters respectively;
5. the goodness of fit $GofF = \sum w_i \left(y_{io} - y_{ic}\right)^2 / (N-P) = \left(R_{wp}/R_E\right)^2$, which should approach the ideal value of unity.

The most meaningful indices for the progress of refinement are R_{wp} and $GofF$ since they contain the quantity being minimized in the numerator. Also R_B is of considerable use since it depends on the fit of structural parameters more than on the profile parameters [86].

Although X-ray diffraction is a convenient tool for immediate registration of lattice modification due to hydrogenation, the main disadvantage of the method is that light atoms, including hydrogen having just one electron, cannot be detected. Since X-rays interact with the electronic cloud of an atom, atoms with atomic number $Z < 13$ are almost "invisible" for X-rays and consequently an alternative method had to be chosen for the determination of hydrogen positions.

4.3. Neutron Diffraction

Neutrons as well as X-rays are used for the scattering experiments on materials. However, neutrons play a unique role due to their inherent properties. Being elementary particles with mass $m_n = 1.675 \cdot 10^{-27}$ kg, zero charge and carrying a spin of ½ which is accompanied by a magnetic dipole moment, the main advantages are the following:

- their dynamic dipole moment allows the investigation of the magnetic properties of materials;
- their large mass leads to a simultaneous sensitivity to the spatial and temporal scales that are characteristics of atomic distances and motions;
- neutrons interact differently with different isotopes of the same atomic species;
- neutrons can easily penetrate a thick material;
- the interaction of the neutron with a nucleus has a simple form (Born approximation) which facilitates the direct unambiguous theoretical interpretation of experimental data.

The scattering amplitude of an individual nucleus for neutrons at the scattering wave vector Q is:

$$a_{Nj}(Q) = b_j + c_j \sigma I_j \tag{4.4}$$

where $1/2\sigma$ is the neutron spin operator and I_j is the spin of nucleus. In the majority of cases the nuclear spins are randomly oriented (they may order at about 10^{-3} K), therefore, the second term does not contribute to the interference effect or coherent scattering. Then the scattering amplitude is equal to:

$$a_{Nj}(Q) = b_j. \tag{4.5}$$

It does not depend on the scattering vector and it is a constant value for each element. In the contrast to X-rays, the scattering amplitude b_j for neutrons does not follow any general tendency and can be even negative in the case of incoherent scattering. Actually hydrogen presents a certain limitation for neutrons, too, being the prime incoherent scatterer. However this problem can be avoided by the replacement of the hydrogen atoms by the atoms of deuterium. Due to similar bonding characters of both isotops we assume that there would be no significant difference in their atomic positions (small differences can be still expected due to different vibrational energies, diffussion rate, etc.).

The interaction of neutrons with a material is given by the scattering cross-section, which is equal to the number of neutrons scattered in a unit body angle. For a fully ordered crystal with atoms occupying positions r_j the scattering cross-section is proportional to the square of the modulus of the scattering amplitude:

$$\left(\frac{d\sigma}{d\Omega}\right)_N = \frac{(2\pi)^3}{V_0}\sum |F_N|^2 \delta(Q-\tau) \tag{4.6}$$

where τ are the positions of nodes in reciprocal space, and F_N is the nuclear structure factor:

$$F_N(Q) = \sum_j b_j e^{iQr_j} e^{-W_j} \tag{4.7}$$

with W – the Debye-Waller factor.

The dipolar interaction between the neutron magnetic moments and the magnetic moments of atoms/ions m_j leads to the magnetic neutron scattering in addition to the nuclear contribution. The magnetic scattering amplitude is:

$$a_{Mj}(\boldsymbol{Q}) = p\boldsymbol{\sigma}\cdot\boldsymbol{M}_{\perp j}(\boldsymbol{Q}) \tag{4.8}$$

where $½\boldsymbol{\sigma}$ is the spin operator of neutron, $\boldsymbol{M}_{\perp j}(\boldsymbol{Q})$ is the projection of vector $\boldsymbol{M}_j(\boldsymbol{Q})$ – the Fourier transform of the magnetisation density $\boldsymbol{M}_j(r)$ around nucleus – onto the plane perpendicular to the scattering vector Q, and:

$$p = \frac{\gamma e^2}{2m_e c^2} = \frac{\gamma r_0}{2} = 0.2696\cdot 10^{-10}\,\text{m}. \tag{4.9}$$

The magnetic stattering amplitude can be presented through the magnetic form factor $f_j(\boldsymbol{Q})$ and projection of the magnetic moment m_j onto the scattering plane by:

$$a_{Mj}(\boldsymbol{Q}) = p\boldsymbol{\sigma}\cdot f(\boldsymbol{Q})\boldsymbol{m}_{\perp j} \tag{4.10}$$

The magnetic scattering cross-section, similarly to the nuclear one, is proportional to the square of the corresponding scattering amplitude summed over all crystal:

$$\left(\frac{d\sigma}{d\Omega}\right)_M = \left|\sum_{lj} a_{Mj}(\boldsymbol{Q}) e^{i\boldsymbol{Q}\cdot\boldsymbol{R}_{lj}}\right|^2 = \frac{(2\pi)^3}{V_0}\sum_k\sum_\tau \left|F_{M\perp}(\boldsymbol{Q})\right|^2 \delta(\boldsymbol{Q}-\boldsymbol{k}-\boldsymbol{\tau}) \tag{4.11}$$

with $\boldsymbol{k}$ – the propagation vector coming from the Fourier expansion of the magnetic moment distribution on position j of cell l:

$$\boldsymbol{m}_{lj} = \sum_k \boldsymbol{m}_j^k e^{-ikl} \tag{4.12}$$

and the magnetic structure factor given by:

$$\boldsymbol{F}_M(\boldsymbol{Q}) = p\sum_j f_j(\boldsymbol{Q})\boldsymbol{m}_j^k e^{i\boldsymbol{Q}\cdot\boldsymbol{r}_j} e^{-W_j} \ . \tag{4.13}$$

It is worth to emphasize that the magnetic structure factor is a complex vector, while the nuclear structure factor is a complex scalar.

For unpolarised neutrons, the Bragg intensity of nuclear and magnetic neutron diffraction is simply an incoherent superposition:

$$I(Q) = I_N(Q) + I_M(Q) \sim |F_N(Q)|^2 + |\boldsymbol{F}_M(\boldsymbol{Q})|^2. \tag{4.14}$$

The analysis of magnetic structure starts with the determination of its periodicity with respect to the crystal structure. The identification of magnetic reflections is usually accomplished by the comparison of powder neutron patterns below and above the magnetic ordering temperature. The nuclear structure factors $F_N(Q)$ can be calculated from the known crystal structure and, applying proper scale factor of the data set, the absolute values of the magnetic structure factors $|\boldsymbol{F}_M(\boldsymbol{Q})|$ can be determined. The individual orientations of the magnetic moments m_j with respect to the basis vectors of the crystal lattice and their magnitudes are then to be calculated.

Powder diffraction data for $U_2Ni_2SnD_{1.8}$, $UCoSnD_{0.6}$ and $URuSnD_{0.6}$ deuterides were taken at Neutron Scattering Center, Hahn-Meitner-Institute, Berlin (E2 instrument – Flat-cone- and powder diffractometer). The measurements were performed at room temperature for $UCoSnD_{0.6}$ and $URuSnD_{0.6}$, and at T = 1.8 K and T = 120 K for $U_2Ni_2SnD_{1.8}$. The thickness of the sample was 8 mm and the container in the form of cylinder was used. The wavelength was chosen depending on the experiment and we used λ = 92 pm and 122 pm for crystal structure

determination and λ = 239.6 pm for magnetic structure studies. For the data analysis, FullProf Suite program [84] was used.

4.4. Magnetic Measurements

Measurements of AC and DC magnetization were performed on two instruments – Quantum Design PPMS extraction magnetometer and Quantum Design SQUID magnetometer – on randomly oriented fixed powder. The mass of the samples was between 50 and 150 mg.

Quantum Design PPMS extraction magnetometer, installed at the Joint Laboratory for magnetic studies, was used for the measurements of AC and DC susceptibility and magnetization curves of the synthesized hydrides. For comparison, the non-hydrogenated precursors were studied in the same experimental conditions. At the extraction method, the magnetized sample is moved through the detection coils and induces a voltage in the detection coil set. The amplitude of this signal is proportional to the magnetic moment and the speed of the sample during extraction. We have performed our measurements in the temperature range from 2 to 300 K, in external magnetic fields up to 14 T.

Additional measurements on deuterides were performed on SQUID magnetometer by Quantum Design, installed at the Institute of Physics of the Academy of Sciences of the Czech Republic. The SQUID magnetometer is a modification of the extraction magnetometer where the variation of magnetic flux due to the movement of the sample is transformed into voltage in the pick up coils. In order to increase the sensitivity, the coils are coupled via superconducting transformer to the detecting Superconducting Quantum Interference Device (SQUID), the operation of which is based on the Josephson effect. As the result, it is possible to register the magnetic moments as small as 10^{-11} Am^2. The magnetometer works in the temperature range 5-300 K and the applied external fields up to 5 T.

4.5. Specific Heat Measurements

The specific heat measurement of synthesized hydrides is non-trivial due to the fact that the samples were obtained in the form of fine powder or were extremely brittle. We implemented a method of measurement of pellets prepared from the powder by pressing by a hydraulic press. A special anvil cell with WC faces allowed to reach several hundreds MPa, which turned out sufficient to produce thin pellets. The samples of approximately 10 mg weight

and diameter not more than 3 mm, with a flat surface attached to the substrate by a small amount of APIEZON N grease, were used for the specific heat measurement.

This technique of the sample preparation has been already applied for the hydrides of $TbMn_2$ compound [87]. However, previously the mixing of the hydride powder with the micrometer-sized Cu (or Ag later on) was applied. The drawback of the method is that the contribution of the sample itself was found to be relatively small in comparison to the contribution from Cu and the addenda what implied some error in the high-temperature range. The samples of larger mass had to be measured in order to get sufficient accuracy. Our innovation was to try to prepare the samples without any additional admixture. We succeeded in preparing suitable pellets with good thermal conductivity and sufficient mechanical properties for specific heat measurements. Therefore we avoided the error due to the presence of another phase and did not have to restrict ourselves only to large samples.

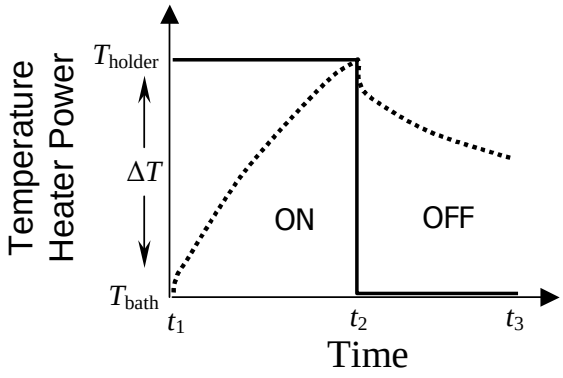

Fig. 4.2. Plot of temperature response in a relaxation measurement

The heat capacity measurements were performed using the PPMS measuring system in the temperature range 1.8-300 K. After the installation of the sample, high vacuum was reached within the chamber and sample was cooled down to the required temperature T. For measuring the specific heat of a material, a heat pulse Q(t) is supplied to the sample within the time interval (t_1-t_2), producing a change in temperature ΔT, as indicated on Fig. 4.2. The temperature of the sample then returns to its initial value with a relaxation time $\tau = C/\kappa$, where C is the specific heat of the sample and κ is the thermal conductance linking the sample to its surrounding. We can write heat-flow equation for one-dimensional case (the power loss through radiation is neglected):

$$C_{total}(T)\frac{dT}{dt} = Q(t) - \kappa_{wires}(T(t) - T_{bath}) \tag{4.15}$$

For the cooling curve we obtain:

$$T(t) = T_{bath} + (T_{holder} - T_{bath})\exp(-t/\tau) \tag{4.16}$$

T_{bath} is original temperature before heating process or is the temperature of the thermal bath. If poor thermal attachment of the sample to the platform produces a temperature difference between the two, the two-tau model is applied to measure the specific heat of the sample. This

model simulates the effect of heat flowing between the sample holder and sample, and the effect of heat flowing between the sample holder and puck (bath). The following equation evaluate two-tau model:

$$\begin{aligned} C_{holder}\frac{dT_{holder}}{dt} &= Q(t) - \kappa_{wires}(T_{holder}(t) - T_{bath}) + \kappa_g(T_{sample}(t) - T_{holder}(t)) \\ C_{sample}\frac{dT_{sample}}{dt} &= -\kappa_g(T_{sample}(t) - T_{holder}(t)) \end{aligned} \quad (4.17)$$

κ_g is the thermal conductance between the sample and sample holder due to the grease. C_{holder} is the heat capacity of the sample holder and $C_{total} = C_{sample} + C_{holder}$.

Solution of the set of Eqns (4.17) for cooling curve is:

$$T(t) = T_{bath} + (T_{holder}(t) - T_{bath})\exp(-t/\tau_1) - (T_{holder}(t) - T_{sample})\exp(-t/\tau_2) \quad (4.18)$$

The temperature of the sample changes exponentially with relaxation times τ_1, τ_2. For calculating specific heat, least-square fitting algorithm is applied. The sensitivity of the fit deviation to small variations in the fitting parameters is used to estimate the standard errors for the specific heat.

4.6. Mössbauer Spectroscopy

The peculiarities of magnetic structure of Sn-containing compounds were studied by Mössbauer spectroscopy. Mössbauer spectroscopy is based on the recoil-free γ-ray resonance emission and absorption in solids, called the Mössbauer effect. On practice, γ-rays from the radioactive source placed on a moving stage pass through a thin specimen and an absorption spectrum is recorded. The data are analyzed in the terms of the hyperfine interactions between the γ-absorbing nuclei in the specimen and the surrounding electrons. Useful information on the phases, the crystalline and bonding states, and the atomic, magnetic, electronic, and defect structures can be obtained.

Simple explanation of Mössbauer effect can be given applying the laws of moment (Eqn. (4.19)) and energy (Eqn. (4.20)) conservation:

$$MV = M(V+v) + \frac{E}{c} \text{ and} \quad (4.19)$$

$$\frac{MV^2}{2} + E_0 = \frac{M(V+v)^2}{2} + E\,. \quad (4.20)$$

When an excited nuclear state drops to the ground level by emitting a γ-ray, a recoil motion will reduce the γ-ray energy, E_0, by the amount of the recoil energy, $Mv^2/2$, where M is the nuclear mass and v the recoil velocity. V is the initial velocity of the nucleus prior to the emission, E is the energy of the emitted γ-ray which is different from E_0, c is the light velocity, and E/c is the γ-ray momentum. From the two equations, the decrease of the γ-ray energy is given as:

$$\delta E = E_0 - E = \frac{E^2}{2Mc} - \frac{EV}{c} \tag{4.21}$$

The first term on the right-hand side is the recoil energy and the last term is the Doppler effect produced by V.

The analysis of hyperfine structure includes at least three elements of hyperfine structure – the isomer shift, the quadrupole splitting, and the nuclear Zeeman splitting (Fig. 4.3). The isomer shift δ is a consequence of Coulombic interaction, which alters the energy separation between the ground state and the excited state of the nucleus, thereby causing a slight shift in the position of the observed resonance line:

$$\delta = \frac{C\Delta R}{R}(\left|\Psi_s(0)_A\right|^2 - \left|\Psi_s(0)_B\right|^2) \tag{4.22}$$

where C is a constant, ΔR is the difference between the nucleus radii in the excited and the ground states, A and B refer to absorber and source, respectively. $|\Psi_s(0)|^2$ is the s-electron density at the nucleus, and as such is affected not only by the s-electron population but also by the screening effects of p-, d-, and f-electrons, by covalency and bond formation, that is by the chemical bonding of the atom. If $\Delta R/R$ is positive, a positive δ corresponds to a higher s-electron density in the absorber nuclei relative to the source ones. The isomer shift can be measured as the deviations of the center of the absorption peak in the Doppler velocity scale.

The electric quadrupole and magnetic dipole interactions both generate multi-line spectra, and consequently provide more information. A nucleus with a spin state greater than ½ has a non-spherical charge distribution and therefore a non-zero quadrupole moment Q. When such a nucleus is placed in an electric field gradient, the electric quadrupole interaction splits the nuclear energy level. The amount of splitting is given by:

$$\Delta = 2\varepsilon = \pm\frac{eQV_{zz}}{2}\left(1+\frac{\eta^2}{3}\right)^{1/2} \tag{4.23}$$

where e is the electron charge, Q the nuclear quadrupole moment, V_{zz} the principal axis component of the field gradient, and η the asymmetry parameter ($0 \le \eta \le 1$).

Another important hyperfine interaction is the nuclear Zeeman effect, by which a nuclear level with a spin I is split into $(2I+1)$ levels when placed in a magnetic field. The eigenvalues of the splits are given by:

$$E_m = -\frac{\mu H_i m_I}{I} \tag{4.24}$$

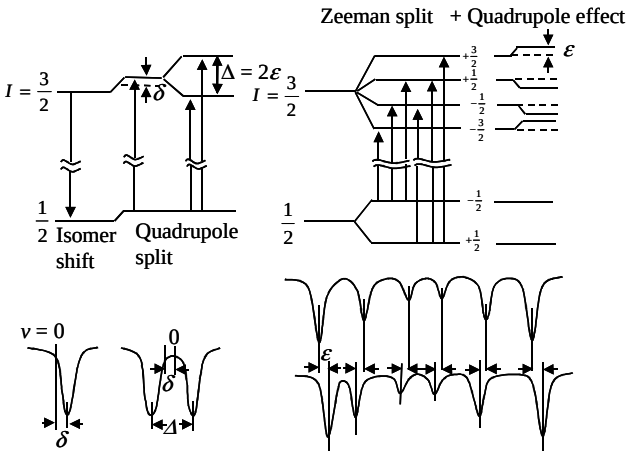

Fig. 4.3. Schematic representation of possible level transitions, Mössbauer parameters, and Mössbauer spectra expected.

where μ is the nuclear moment, H_i is the internal magnetic field, and m_I is the magnetic quantum number. The theoretically determined ratio for a randomly oriented sample of the intensities of the Zeeman spectrum consisting of 6 lines is 3:2:1:1:2:3.

Both the magnetic and quadrupole interactions are direction-dependent effects and the effect of a first-order quadrupole perturbation on a magnetic hyperfine spectrum leads to shifts of the 2 outer lines and the 4 inner lines of the magnetic sextet in opposite directions. When both the electric quadrupole and magnetic dipole interactions are of the same order of magnitude the exact Hamiltonian has to be solved in order to estimate the position and relative intensities of the absorption lines.

Mössbauer spectroscopy data were collected at the laboratory of Instituto Tecnólogico e Nuclear/CFMC-UL, Sacavém, Portugal. Mössbauer spectra were collected in transmission mode using a conventional constant-acceleration spectrometer and a 10 mCi ^{119m}Sn source in $CaSnO_3$; the velocity scale was calibrated using α-Fe foil. The absorbers were obtained by pressing the powdered samples into perspex holders. The absorber thickness was calculated on the basis of the corresponding electronic mass-absorption coefficients for the 23.9 keV radiation. For the data presented in this work, the isomer shifts (IS) are given relative to the $CaSnO_3$ source. For $E\gamma$= 23.875 keV γtransition in ^{119}Sn, 1mm/s corresponds to $7.963(2)\cdot 10^{-8}$ eV or 19.253(6) MHz. Low-temperature spectra were collected using a liquid-helium flow cryostat with a temperature stability of ± 0.5 K. The spectra were fitted to Lorentzian lines using a non-linear least-squares method [88]. The position and relative intensities of the absorption lines of the Sn atoms with nonzero transferred magnetic hyperfine field were calculated by solving the complete

Hamiltonian for the hyperfine interactions in both the excited and ground nuclear states of the ^{119}Sn nuclei, following the procedure described by Ruebenbauer and Birchall [89].

5. Results and Discussion

5.1. Hydrides of UTX Compounds

U*TX* compounds form a very wide group of uranium intermetallics and crystallize with a variety of structure types. In order to perform systematic studies, we restricted ourselves to two groups of isostructural compounds – crystallizing with hexagonal ZrNiAl and orthorhombic TiNiSi types of structure. Out of the former group two stanides UCoSn and URuSn were found to form stable hydrides and also the hydrides of the compound forming solid solution $UCo_{1-x}Ru_xSn$ were synthesized and studied. The only investigated gallide UCoGa did not absorb hydrogen up pressure 130 bar and temperature 923 K. Just one compound UCoSi was found to absorb hydrogen, in addition to the reported before UNiSi and UPdSi hydrides, out of the latter group. It was found that URuSi, URhSi and UPtSi do not absorb detectable amount of hydrogen up to pressure 130 bar and temperature 923 K.

5.1.1. Hydrides of UCoSn and URuSn Compounds: Crystal Structure and Magnetism

The studies of hydrides of uranium ternaries with ZrNiAl structure type were restricted to the studies of UNiAl hydrides. All the following attempts to obtain hydrides of other aluminides containing different transition metal were not successful. Therefore we tried another approach by changing the *p*-element. By substitution of Al by another *p*-element with larger radius the hydrogen absorption might become more favourable due to pure geometrical considerations – the expanded interstitials can allocate hydrogen atoms more easily. And indeed, we registered hydrogen absorption for two isostructural stanides – UCoSn and URuSn.

UCoSn and URuSn intermetallic compounds were used as starting materials for hydrogenation. The synthesis was performed at hydrogen pressure 120 bar and at temperture $T = 923$ K. Hydrides with the composition $UCoSnH_{1.4}$ and $URuSnH_{1.4}$ were formed. The stoichiometry was determined by the decomposition in closed volume and decomposition curves of the hydrides point to a single-stage decomposition process at $T \approx 500$°C.

Crystal structure of the initials compounds and of the synthesized hydrides was studied by X-ray powder diffraction. The X-ray powder patterns of UCoSn, URuSn and respective hydrides are presented in Appendix A and Appendix B. The structure data on UCoSn and URuSn are in good agreement with the literature data. Both $UCoSnH_{1.4}$ and $URuSnH_{1.4}$ hydrides

crystallize in the hexagonal ZrNiAl-type of structure similar to the initial compounds. Hydrogenation leads to a unit cell expansion in both cases, which is significantly larger for UCoSn: the volume expansion reaches 3.2% for UCoSn, while it is 1.2% for URuSn. The lattice expansion has pronounced anisotropy in both compounds. In the case of UCoSn the *a*-axis expansion dominates. This anisotropy is even more striking in URuSn. The lattice parameter *c* remains unaffected by hydrogenation within the experimental error and the observed lattice expansion is solely due to the modifications within the basal plane. The results of the crystal structure refinement of UCoSn and URuSn compounds and their hydrides are summarized in Table 5.1. The interuranium distances were calculated from the formula for hexagonal symmetry:

$$d = \sqrt{\left[a^2((\Delta x)^2 + (\Delta y)^2 - \Delta x \Delta y) + (c\Delta z)^2\right]}. \quad (5.1)$$

Taking into account the symmetry operations and the fact that uranium atoms are located at the same height (*i.e.* $\Delta z = 0$), Eqn. (5.1) can be simplified to:

$$d_{U-U} = a\sqrt{1 - 3x - 3x^2} \quad (5.2)$$

Hydrogen positions could not be specified from X-ray data.

Table 5.1. Comparison of crystal structure and magnetic susceptibility parameters of UCoSn, URuSn and their hydrides obtained in this work. Lattice parameters *a* and *c*, unit cell volume *V*, relative increase of lattice parameters (*a*, *c*) and volume change with respect to the parent compounds, internal structure parameters x_U and x_{Sn} for U and Sn atoms, respectively, inter-uranium spacing $d_{U\text{-}U}$, and Bragg *R*-factor R_B, parameters of the fit of the susceptibility in the modified Curie-Weiss regime (high *T*): effective moments μ_{eff}, paramagnetic Curie temperature Θ_p, the *T*-independent term χ_0 and the ordering Curie temperature T_C are given.

	UCoSn	$UCoSnH_{1.4}$	URuSn	$URuSnH_{1.4}$
a (pm)	714.59(7)	723.86(6)	735.09(8)	739.32(14)
c (pm)	399.43(6)	401.89(5)	394.96(7)	394.92(19)
V (10^8pm)	1.766	1.824	1.848	1.869
$\Delta a/a$ (%)	-	1.3	-	0.6
$\Delta c/c$ (%)	-	0.6	-	0.0
$\Delta V/V$ (%)	-	3.3	-	1.1
x_U	0.589(1)	0.600(1)	0.591(2)	0.591(2)
x_{Sn}	0.250(2)	0.257(2)	0.249(3)	0.261(3)
$d_{U\text{-}U}$ (pm)	374	383	384	387
$\mu_{eff.}$(μ_B/f.u.)	2.0	2.0	1.7	1.9
Θ_p (K)	77	97	49	42
χ_0 ($10^{-8}m^3$/mol)	1.3	1.1	1.5	1.2
T_C (K)	82	102	54	51

The studies of magnetic properties for UCoSn, URuSn and the respective hydrides were performed at PPMS measurement system in the temperature range 2-300 K and applying magnetic fiels up to 9 T. UCoSn and URuSn are known to be ferromagnets with ordering temperatures T_C = 80-88 K [35-38] and T_C = 51-55 K [38, 40-42], respectively. The values obtained in the present work correspond well to the reported data (Table 5.1). Hydrogenation does not change the type of magnetic ordering for both compounds, but modifies magnetic moments and ordering temperature (Fig. 5.1). Moreover, the change of magnetic properties upon hydrogenation has different character for the two compounds. According to the magnetic susceptibility measurements, the ordering temperature grows in the case of UCoSn from 82 K in the parent compound to 102.5 K in the hydride. The ordering temperature for the $UCoSnH_{1.4}$ hydride, was determined from the Arrott plot (Fig. 5.2), which showed a linear dependence for M^2 versus H/M in high field region. The value of 102.5 K appears to be the highest Curie temperature found for the equiatomic uranium ternaries so far. The spontaneous magnetic moment of uranium atoms, measured on fixed randomly oriented powder, increases from 0.64 μ_B/U-atom in UCoSn to 0.75 μ_B/U-atom in $UCoSnH_{1.4}$ (Fig. 5.3).

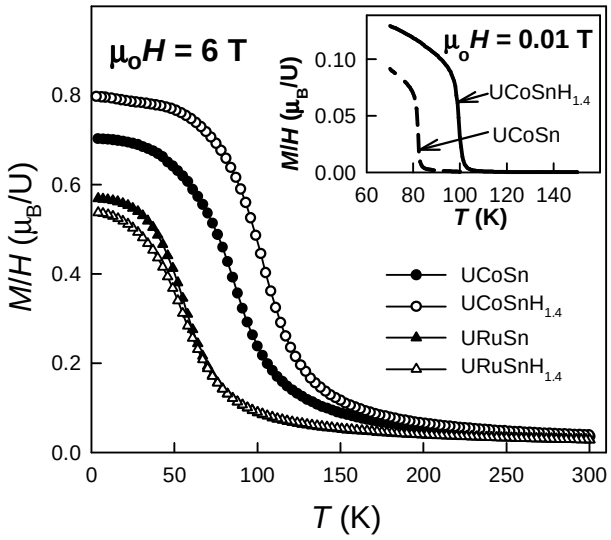

Fig. 5.1. Temperature dependence of the magnetic susceptibility $\chi(T)$ for UCoSn, URuSn and their hydrides, measured in $\mu_o H$ = 6 T. The inset shows the temperature dependence the of magnetic susceptibility for UCoSn and $UCoSnH_{1.4}$ in $\mu_o H$ = 0.01 T

Surprisingly, an opposite impact of hydrogenation on the magnetism is observed for URuSn. The ordering temperature decreases from 54 K in the initial compound to 51 K in the hydride. Unlike the majority of the uranium intermetallics studied, the hydrogenation weakens the ferromagnetic interactions, and the magnetic moment of the uranium atoms decreases from 0.53 μ_B/U-atom in the parent compound to 0.48 μ_B/U-atom in the hydride (Fig. 5.3).

The results of the analysis of in the paramagnetic region of the magnetic susceptibility of UCoSn and URuSn and the corresponding hydrides, described by modified Curie-Weiss law, are also summarized in Table 5.1.

Magnetization curves and susceptibility behaviour have a character, which does not change qualitatively between the parent compounds and their hydrides, and the lattice expansion

preserves the basic geometry of the lattice with the shortest U–U spacing within the basal plane. This geometry leads generally (for U intermetallics) to a strong uniaxial anisotropy with the magnetic moments aligned along the *c*-axis. Conseqently, the spontaneous magnetization obtained on randomly oriented powders corresponds to 50% of intrinsic U moments, and we can estimate the μ_U values as 1.50 μ_B for $UCoSnH_{1.4}$ and 0.96 μ_B for $URuSnH_{1.4}$.

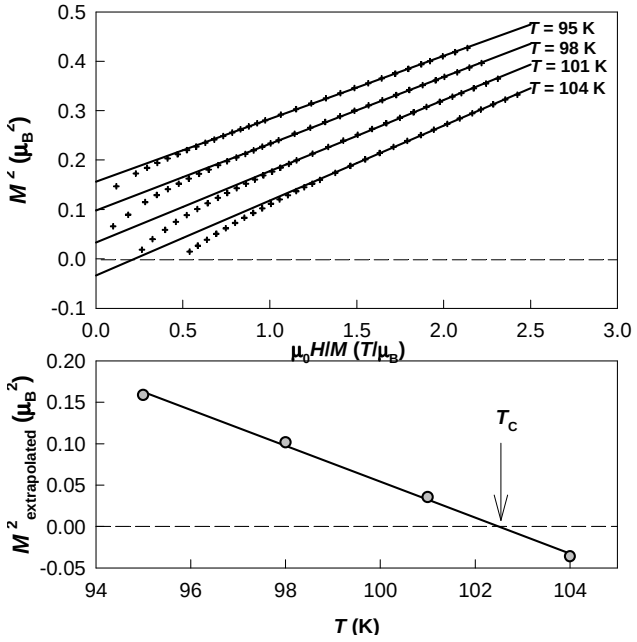

Fig. 5.2. Arrott plot for $UCoSnH_{1.4}$ hydride

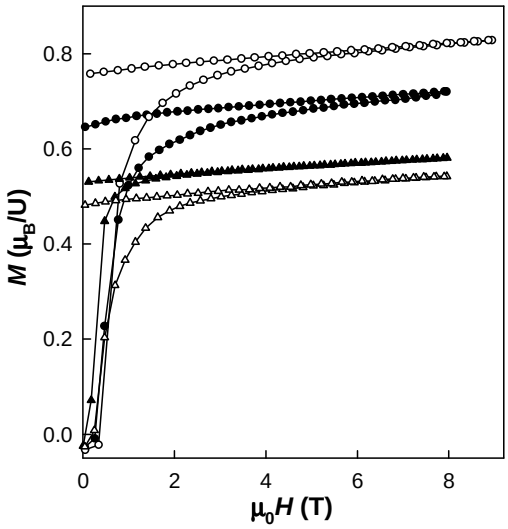

Fig. 5.3. Magnetization curves of UCoSn, URuSn and their hydrides measured at T = 2 K.

The values of T_C (102.5 K) and μ_U (1.50 μ_B/f.u.) found in $UCoSnH_{1.4}$ are record values among all U*TX* ferromagnets. Similar ordering temperature was only found for the antiferromagnet $UNiAlH_{2.3}$ (T_N = 99 K, μ_U could not be determined) [69]. The theory of hybridisation-mediated exchange interaction in light actinides assumes that magnetic moments are gradually reduced by the strengthening of the 5*f*-ligand hybridisation, which, though, mediates the exchange interaction. This model seems appropriate for narrow band systems with a moderate hybridisation. For magnetic systems with broader 5*f* bands we may assume the situation of a typical band magnetism, for which the ordering temperature and the size of magnetic moments are proportional to each other.

Hydrogen absorption can be expected as increasing the localization of the 5*f* states due to the reduction of the 5*f*-5*f* overlap (consequence of the lattice expansion). Comparing the properties of $UCoSnH_{1.4}$ with other ZrNiAl-structure compounds of the UCo*X* series one can see the gradual development of magnetism with a unit cell expansion (*i.e.* the U–U distance

increases): while UCoAl exhibits no magnetic ordering [90], T_C and μ_U increase with the volume in the sequence UCoGa – UCoSn – $UCoSnH_{1.4}$.

If hydrogen occupies positions close to the transition metal *T*, one can speculate that the bonding of the *d*-states of the transition metal with the hydrogen states withdraws partly the *d* states from the 5*f*–*d* hybridisation, leaving the 5*f* states less hybridised. The two strong reasons are the most plausible source of strengthening of the magnetism in light actinide hydride systems due to hydrogen absorption. They can be taken responsible for the variations of the UCoSn magnetism, which points to quite an itinerant character of its magnetism, resulting from a rather strong 3*d*–5*f* hybridisation.

The case of URuSn seems to be rather curious, not fitting into the context mentioned above. In fact, we are not aware of any analogous cases of a reduction of T_C and μ_s due to hydrogen absorption in U intemetallics. The degree of the 5*f* delocalization in URuSn should not differ dramatically from the UCoSn situation, as the 4*d* states hybridise less with the 5*f*'s than the corresponding 3*d* states, while the *d*-states of the Fe subgroup are closer to the Fermi level than for the Co subgroup, and thus overlap more with the 5*f* states in the *k*-space, contributing to a stronger delocalization. Consequently, the anomalous tendency in the URuSn hydride looks incompatible with the two general mechanisms. The smaller lattice expansion for a comparable H content may point to different interstitial positions occupied in this case. We may speculate then about a predominant effect of a reduction of the density of states at the Fermi level, $N(E_F)$, which may tend to suppress the magnetism.

To obtain more information on the different behaviour of UCoSn and URuSn hydrides, the studies of hydrogenation of pseudoternary system $UCo_{1-x}Ru_xSn$ and its impact on magnetism were carried out.

5.1.2. Hydrides of $UCo_{1-x}Ru_xSn$ Compounds: Crystal Structure and Magnetism

Hydrogen absorption properties of $UCo_{1-x}Ru_xSn$ were studied on 5 compounds with x = 0.1, 0.3, 0.5, 0.7, and 0.9. We assume that all compounds absorb 1.4 H atoms per formula unit similar to UCoSn and URuSn, what was checked on the hydride of the compound with the composition $UCo_{0.5}Ru_{0.5}Sn$. X-ray powder diffraction studies showed that ZrNiAl strucure type is preserved both for the initial compounds and for the hydrides throughout the whole series. The main crystal structure parameters can be found in Table 5.2.

$UCo_{1-x}Ru_xSnH_{1.4}$ hydrides do not exhibit monotonous changes of the lattice parameters *a* and *c* upon hydrogenation and the Vegard's law is not fulfilled (Fig. 5.4, *a*). The *a* parameter

increases from UCoSn to URuSn, but not linearly. There is an abrupt reduction along the *c* direction with the minimum value around the composition $UCo_{0.33}Ru_{0.67}SnH_{1.4}$, while for UCoSn-URuSn solid solution the minimum value of the lattice parameter *c* around the composition $UCo_{0.33}Ru_{0.67}Sn$ was registered. The concentration dependence of the unit cell volume for $UCo_{1-x}Ru_xSnH_{1.4}$ hydrides clearly shows two regions with different behaviour. One observes a pronounced discontinuity around the composition $UCo_{0.33}Ru_{0.67}SnH_{1.4}$ (Fig 5.4, *b*), while the non-hydrogenated compounds are characterized by the change of the slope of the dependence of the unit cell volume, explained by the preferable occupation of one transition metal sites and only consequent occupation of the remaining one.

Table 5.2. Crystallografic data – lattice parameters *a*, *c* and unit cell volume *V* – and ferromagnetic ordering temperature T_C, determined from AC susceptibility measurements, of $UCo_{1-x}Ru_xSn$ compounds and respective hydrides.

Compound	*a* (pm)	*c* (pm)	*V* (10^8pm^3)	Δ*a*/*a* (%)	Δ*c*/*c* (%)	Δ*V*/*V* (%)	T_C (K)
$UCo_{0.9}Ru_{0.1}Sn$	719.4(3)	395.9(2)	1.774(1)	-	-	-	82*
$UCo_{0.9}Ru_{0.1}SnH_{1.4}$	726.3(3)	401.5(2)	1.834(1)	0.97	1.41	3.38	104
$UCo_{0.7}Ru_{0.3}Sn$	725.8(4)	392.5(4)	1.790(2)	-	-	-	82*
$UCo_{0.7}Ru_{0.3}SnH_{1.4}$	729.4(6)	401.4(5)	1.850(3)	0.50	2.27	3.35	104
$UCo_{0.5}Ru_{0.5}Sn$	729.5(5)	391.0(4)	1.802(3)	-	-	-	82*
$UCo_{0.5}Ru_{0.5}SnH_{1.4}$	733.2(4)	399.7(3)	1.861(2)	0.51	2.22	3.27	94
$UCo_{0.3}Ru_{0.7}Sn$	731.7(5)	390.7(3)	1.811(2)	-	-	-	80*
$UCo_{0.3}Ru_{0.7}SnH_{1.4}$	736.4(5)	392.2(4)	1.842(2)	0.64	0.38	1.71	78
$UCo_{0.1}Ru_{0.9}Sn$	733.7(3)	393.3(2)	1.834(2)	-	-	-	71*
$UCo_{0.1}Ru_{0.9}SnH_{1.4}$	738.2(3)	394.2(3)	1.861(2)	0.61	0.23	1.47	68

*Reference [44]

The concentration dependence of the volume expansion exhibits two characteristic regions, therefore (Fig. 5.4, *c*): for $x = 0 \div 0.5$ the volume expansion is almost constant and for $x = 0.7 \div 1.0$ the absolute value of volume expansion is considerably lower and there is moderate decrease with the increase of ruthenium content. The anisotropy of lattice expansion is changed throughout the series. Even small addition of Ru to UCoSn results in the dominant lattice expansion along the *c*-direction, but in the Ru-rich region the basal-plane lattice expansion prevails.

The Curie temperature slightly increases for moderate substitution of Co by Ru in UCoSn ($x = 0 \div 0.3$) and reaches its maximum at $T = 104$ K according to the AC magnetization measurements (Fig. 5.5, *a*). Another characteristic region is the Ru-rich area ($x = 0.7 \div 1.0$), which is characterized by the relative decrease of the Curie temperature (Fig. 5.5, *b*). Apparently there is a continuous decrease of the Curie temperature between $x = 0.5$ and $x = 0.7$.

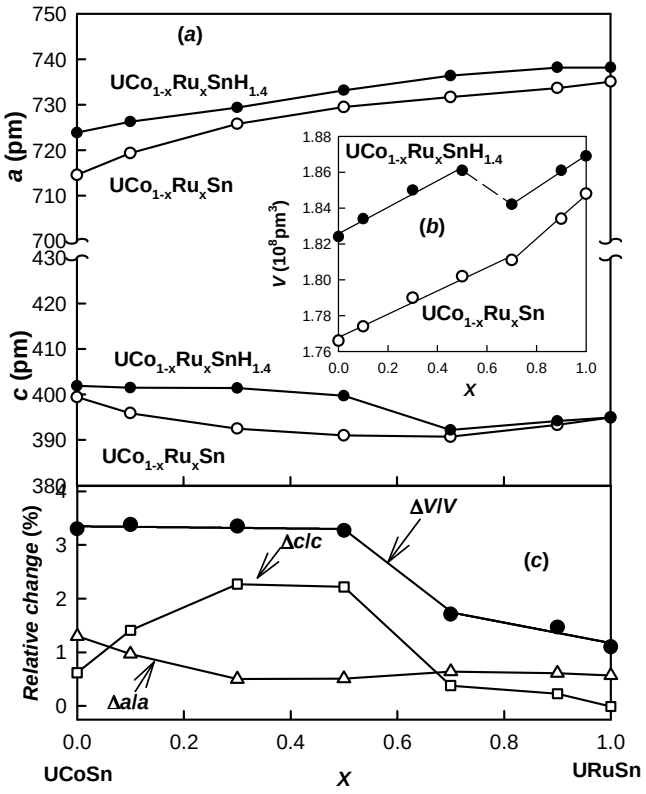

Fig. 5.4. The concentration dependence of the lattice parameters *a* and *c* (*a*), unit cell volume *V* (*b*) for $UCo_{1-x}Ru_xSn$ compounds and respective hydrides, and relative linear expansion along the *a*, $\Delta a/a$, and *c*, $\Delta c/c$, directions and relative volume expansion, $\Delta V/V$ (*c*).

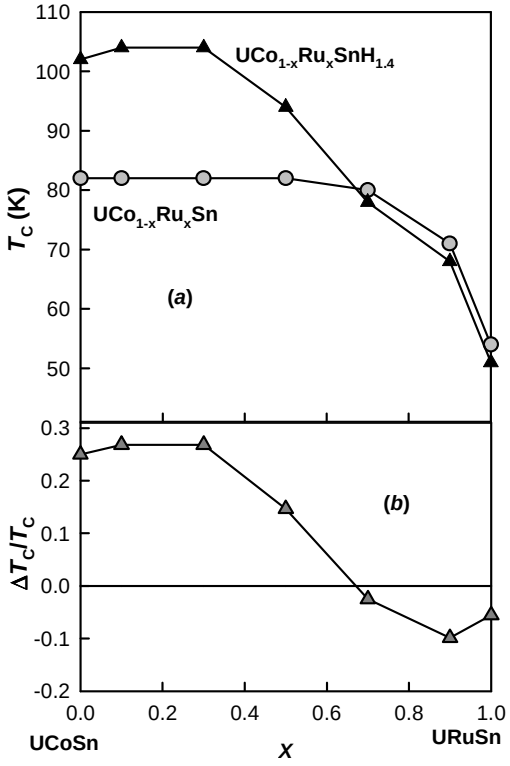

Fig. 5.5. The concentration dependence of the Curie temperature T_C for $UCo_{1-x}Ru_xSn$ compounds (*a*) and the relative change for the ordering temperature $\Delta T_C/T_C$ (*b*).

If one compares the plots of the concentration dependence of crystal structure parameters and the Curie temperature, it is evident that hydrogenation emphasizes the existence of the critical concentration of 66.6% of Ru and such a difference both at structure and magnetic parameters let us assume that hydrogen atoms occupy different positions in UCoSn and URuSn hydrides. However this can be taken as an indirect but still not evidences and therefore the respective deuterides of UCoSn and URuSn have been synthesized. It allowed to try to determine deuterium (hydrogen) positions by means of neutron diffraction.

5.1.3. Deuterides of UCoSn and URuSn

Both deuterides of UCoSn and URuSn were prepared by the same technique, as their analogues with hydrogen. The synthesis was performed at hydrogen pressure 120 bar and at temperture $T = 923$ K. The phase composition of the initial samples and of deuterides was checked by X-ray powder diffraction.

a) X-ray diffraction and magnetic measurements

The X-ray powder diffraction patterns of the initial intermetallics showed the presence of the UCoSn and URuSn major phases and small amount of the spurious phases in both cases – $U_2Co_3Sn_4$ in the case of UCoSn and an unidentified one in the case of URuSn. The spurious phases remain unaffected by deuteration, as was seen from the diffraction pattern of the samples after deuteration. The crystal structure parameters for the synthesized deuterides are given in Table 5.3.

For the deuteride of UCoSn the crystal structure parameters are very close to those, obtained for $UCoSnH_{1.4}$. However, for URuSn, which behaves somewhat anomalous upon hydrogenation, the deuteration leads to different results. The lattice expansion is 2.5 times larger for URuSn deuteride comparing to $URuSnH_{1.4}$, but again the lattice expansion only in the basal plane is observed. Taking into consideration the same character of the lattice expansion, we suppose that larger lattice expansion does not necessarily mean different positions of hydrogen and deuterium atoms. Moreover, we tend to assume that in this case we deal with the isotope effect of the substitution of hydrogen atoms for deuterium, which changes the interactions with the metal atoms.

An interesting fact was revealed by the decomposition studies of the the UCoSn deuteride. The decomposition in vacuum by heating up to 1023 K resulted in the stoichiometry of 0.7(1) D atoms per formula unit. The possible reason could be partial decomposition with time (no structure data were obtained on the sample directly before decomposition), however, it will be shown later, that neutron diffraction data, obtained on “fresh” sample contradict this assumption.

The magnetic measurements were performed in the temperature range 5-300 K in magnetic fields 0.01 T, 2 T, and 4 T. Both deuterides order ferromagnetically similar to the hydrides and the initial compounds. In the paramagnetic range the susceptibility curves for both compounds are described by modified Curie-Weiss law (Fig. 5.6 (*a*, *b*)) and the respective parameters are given in Table 5.3. For UCoSn the paramagnetic Curie temperature is slightly

higher comparing to the hydride and the effective moment can be considered as unchanged. The inverse susceptibility plots show that there is a slight shift of the susceptibility values to the higher temperatures. In more details it can be seen on the low-field susceptibility curves ($\mu_0 H$ = 0.01 T) (Fig. 5.6 (*c*)), which show that the transition is approximately 2 K higher for $UCoSnD_{0.7}$ comparing to $UCoSnH_{1.4}$. This effect can be attributed, however, to small but non-zero homogeneity region due to the non-stoichiometric composition of the hydride or to the difference in experimental setup. But the proximity of both structural and magnetic parameters for the hydride and deuteride let us assume that the structure data obtained for deuteride would be also valid for the hydride.

Table 5.3. Comparison of crystal structure and magnetic susceptibility parameters of the deuterides of UCoSn and URuSn (stoichiometry is taken from neutron diffraction results which will be discussed later). Lattice parameters *a* and *c*, unit cell volume *V*, relative increase of lattice parameters (*a*, *c*) and volume change with respect to the parent compounds, free atomic parameters x_U and x_{Sn} for U and Sn atoms, respectively; inter-uranium spacing $d_{U\text{-}U}$, parameters of the fit of the susceptibility in the modified Curie-Weiss regime (high *T*): effective moments μ_{eff}, paramagnetic Curie temperature Θ_p, the *T*-independent term χ_0 are given.

	$UCoSnD_{0.6}$	$URuSnD_{0.6}$
a (pm)	723.45(6)	745.30(22)
c (pm)	402.33(5)	395.04(15)
V (10^8pm)	1.824	1.900
$\Delta a/a$ (%)	1.2	1.4
$\Delta c/c$ (%)	0.7	0.0
$\Delta V/V$ (%)	3.3	2.8
x_U	0.601(1)	0.595(1)
x_{Sn}	0.251(3)	0.254(3)
$d_{U\text{-}U}$ (pm)	383	393
$\mu_{eff.}$(μ_B/f.u.)	2.1	1.6
Θ_p (K)	102	58
χ_0 ($10^{-8}m^3$/mol)	1.1	1.6

The situation is different for URuSn. $URuSnD_{0.6}$ is characterised by slight increase of the Curie temperature compared not only to $URuSnH_{1.4}$ but to URuSn as well (Fig. 5.6 (*d*)). The variations are insignificant, therefore the possibility of non-stoichiometry and the difference in the experimental setup should be considered like in the case of UCoSn. It is evident that the variations are more modest as they could be expected comparing to UCoSn, for which the ordering temperature increase reaches 20 K. For URuSn the ordering temperature increases by less then 2 K only. This observation leads us to a hypothesis that the increase of the ordering temperature for UCoSn is mainly due to the lattice expansion along the *c* axis, because the

expansion within the basal plane for $URuSnD_{0.6}$ even exceeds the expansion observed for $UCoSnD_{0.6}$. This agrees well with the results of the studies of the hydrides of the $UCo_{1-x}Ru_xSn$ compounds. For both UCoSn and URuSn compounds each uranium atom has 5 nearest transition metal neighbours – 1 transition metal atom in the same atomic plane and 4 atoms in two adjacent atomic planes. For UCoSn these five distances are equal within the experimental error, and for URuSn the distance to the Ru atoms in the adjacent planes is slightly smaller.

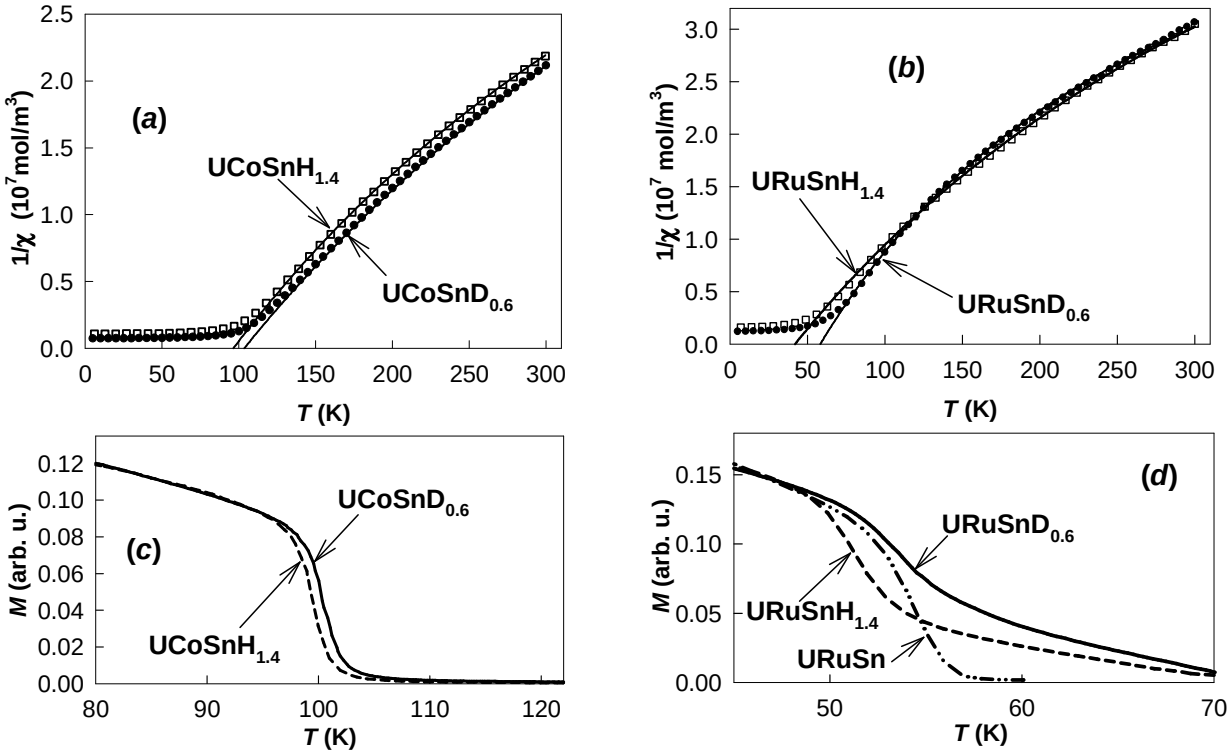

Fig. 5.6. Temperature dependence of the inverse susceptibility of $UCoSnH_{1.4}$ measured in the magnetic field 6 T and of $UCoSnD_{0.6}$ measured in the magnetic field 4 T (*a*), temperature dependence of the inverse susceptibility of $URuSnH_{1.4}$ measured in the magnetic field 6 T and URuSnD measured in the magnetic field 4 T (*b*), temperature dependence of magnetization of $UCoSnH_{1.4}$ and $UCoSnD_{0.6}$ measured in the magnetic field 0.01 T (*c*) and temperature dependence of magnetization of $URuSnH_{1.4}$, $URuSnD_{0.6}$ and URuSn measured in the magnetic field 0.01 T (*d*).

Hydrogenation/deuteration and consequent lattice expansion has larger effect on the distances between the atoms in the adjacent planes in the case of UCoSn and uranium atoms turn to have one nearest *T* neighbour in the same atomic plane. This might result in the weakening of the interaction with the four remaining nearest neighbours, and hereafter – the decrease of the degree of 5*f*-3*d* hybridisation. The effect is opposite for URuSn, for which hydrogenation/deuteration does not affect the lattice parameter *c* and 4 nearest Ru atoms in the neighbouring atomic planes remain the nearest neighbours of uranium atoms. This is a possible reason why hydrogenation/deuteration has almost no impact on the magnetic properties of URuSn.

b) Neutron diffraction studies

The neutron powder patterns for both UCoSn and URuSn deuterides were obtained at room temperature using germanium monochromator (λ = 122 pm) in the angular range 2θ = 5–84.6º with the step 0.2 degrees. The main task was to determine the deuterium positions in these compounds.

The neutron diffraction pattern of $UCoSnD_{0.6}$ is shown on Fig. 5.7. The crystal structure refinement showed that the metal atoms form the ZrNiAl structure type similar to the initial compound and deuterium atoms occupy the 4*h* position inside the U_3Ni tetrahedra. The crystal structure parameters are given in Table 5.4. The interatomic distances are presented in Appendix C. The crystallographic stoichiometry was refined as $UCoSnD_{0.58(3)}$, what is smaller comparing to the stoichiometry determined by volumetric method (0.7(1) D atoms/f.u.) but both values are comparable within the error bars. This structure was found already for $UNiAlD_{0.7}$ [75] – an unsaturated hydride of isostructural UNiAl. The crystal structure of $UCoSnD_{0.6}$ is presented on Fig. 5.8. Fig. 5.9 represents the position of deuterium atoms projected to the network of uranium atoms.

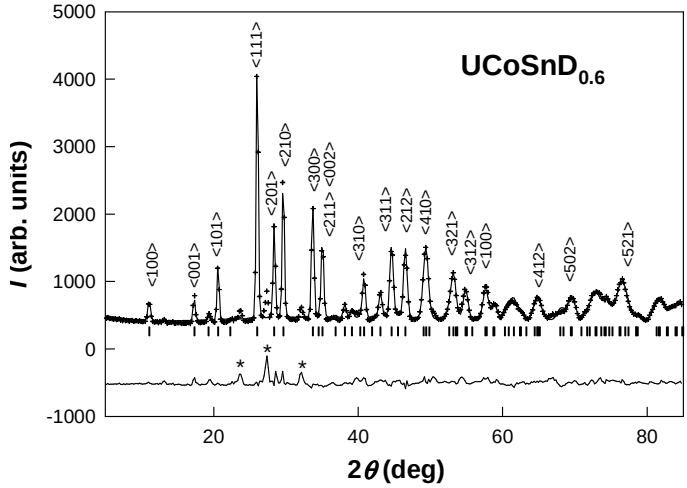

Fig. 5.7. Neutron diffraction pattern of $UCoSnD_{0.6}$ (λ = 122 pm). The observed values are shown by crosses and calculated by solid line. The impurity contribution is starred at the difference curve. R_B = 6.05%

The U_3Ni tetrahedra, which allocate deuterium atom, share a face. The distance between

Table 5.4. Rietveld refined atomic parameters for $UCoSnD_{0.6}$: internal parameters *x*, *y*, *z*, and the coefficients of the site occupancy *n*, obtained from neutron diffraction at room temperature (R_B = 6.05 %).

Atom	Site	*x*	*y*	*z*	*n*
U	3*g*	0.596(1)	0	0.5	1
Co1	1*b*	0	0	0.5	1
Co2	2*c*	1/3	2/3	0	1
Sn	3*f*	0.259(1)	0	0	1
D	4*h*	1/3	2/3	0.445(9)	0.44(2)

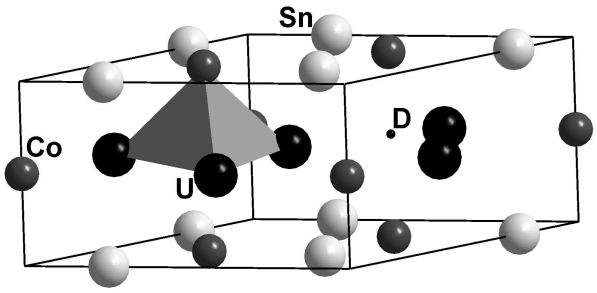

Fig. 5.8. Crystal structure of $UCoSnD_{0.6}$.

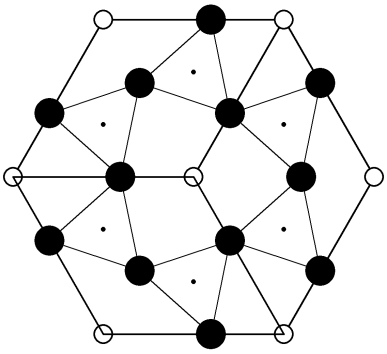

Fig. 5.9. Atomic arrangement for $UCoSnD_{0.6}$ projected on uranium plane. Uranium atoms are represented as filled circles, nickel atoms – empty circle, and deuterium atoms – black dots.

two deuterium positions (44 pm) does not allow simultaneous occupancy of the neighbouring sites. However, the full occupancy of this site would give the stoichiometry of 1.33 deuterium (hydrogen) atoms per formula unit – the value observed for the hydride of UCoSn. The necessary condition is the value of $z_H < 0.3$. Therefore we may speculate about slightly shorter Co-H distance comparing to Co-D distance which would make it possible to occupy both neighbouring tetrahedra and yield the composition $UCoSnH_{1.33}$. Such structure was already observed for $RE_3Ni_3In_3D_4$ deuterides (*RE* = La, Ce, and Nd) [91], which where characterized by anomalously short hydrogen-hydrogen distance of 160 pm.

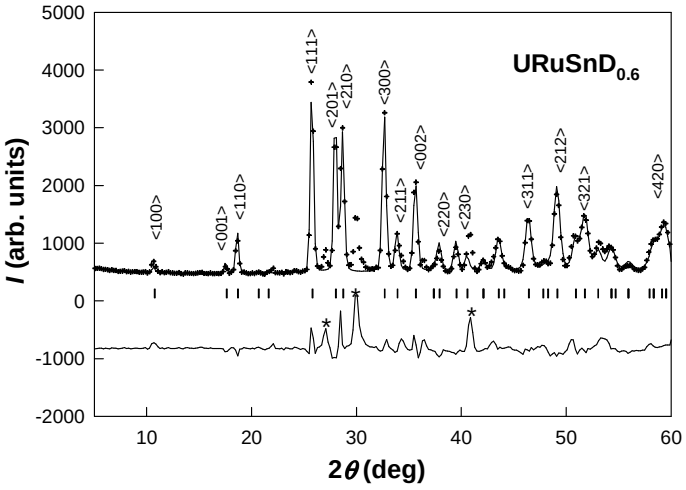

Fig. 5.10. Neutron diffraction pattern of $URuSnD_{0.6}$ (λ = 122 pm). The observed values are shown by crosses and calculated by solid line. The impurity contribution is starred at the difference curve. R_B = 11.4%

The crystal structure model solved for $UCoSnD_{0.6}$ did not however work for the URuSn deuteride. The neutron diffraction pattern is shown on Fig. 5.10. The metal atoms form the initial ZrNiAl structure type as well, and two additional deuterium positions were found. The crystal structure parameters are given in Table 5.5. The list of interatomic distances is given in Appendix D. The calculated

Table 5.5. Rietveld refined atomic parameters for $URuSnD_{0.6}$: internal parameters *x*, *y*, *z*, and the coefficients of the site occupancy *n*, obtained from neutron diffraction at room temperature (R_B = 11.4 %).

Atom	Site	*x*	*y*	*z*	*n*
U	3*g*	0.598(3)	0	0.5	1
Ru1	1*b*	0	0	0.5	1
Ru2	2*c*	1/3	2/3	0	1
Sn	3*f*	0.253(5)	0	0	1
D1	2*d*	1/3	2/3	0.5	0.68(3)
D2	3*g*	0.215(35)	0	0.5	0.14(2)

crystallographic stoichiometry of the deuteride is $URuSnD_{0.59(4)}$.

Deuterium atoms occupy 2*d* and 3*g* positions. The 2*d* position is very close to the 4*h* position observed for $UCoSnD_{0.6}$. The difference is that deuterium atoms are not shifted out from the uranium plane, like for $UCoSnD_{0.6}$, but they are placed between the uranium atoms at $z = 0.5$. The coordination sphere of deuterium is the triangular bipyramid U_3Ru_2 (Fig. 5.11). The atomic environment of deuterium atoms in 3*g* position can be considered as a distorted octahedra consisting of three uranium atoms, two tin atoms and one nickel atom. The occupancy of this site is relatively small (14%). Both deuterium sites lay at $z = 0.5$ and the representation of this atomic plane is given on Fig. 5.12. This fact explains why lattice expansion along the *c*-direction is not observed for URuSn deuteride. Besides, the 2*d* position of deuterium implies weaker interaction with Ru than if deuterium occupied 4*h* position, as in case of UCoSn. It agrees well with the results of the magnetization studies – indeed the impact of deuterium absorption on *f-d* hydridization is not so pronounced. The lattice expansion within the basal

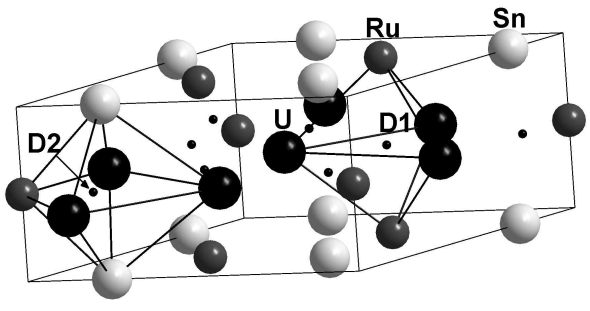

Fig. 5.11. Crystal structure of $URuSnD_{0.6}$.

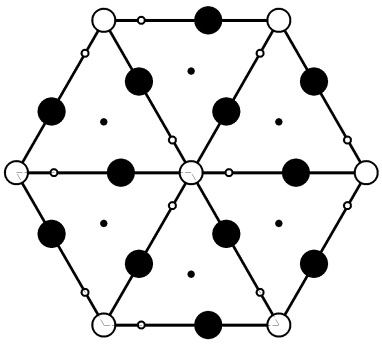

Fig. 5.12. The atomic plane at $z = 0.5$ for $URuSnD_{0.6}$. Uranium atoms are represented as large filled circles, nickel atoms – large empty circle, and deuterium D1 atoms – black small circles, and deuterium D2 atoms – empty small circles.

plane modifies the inter-uranium distance perpendicular to the *c*-axis, while the lattice parameter *c* remains practically constant. From the analysis of interatomic distances one can see that the distance between the uranium atoms in the basal plane reaches very close (within the experimental error) the distance along the *c*-direction. Such structure is very untypical for other U*TX* compounds with ZrNiAl structure type, for in almost all the cases the shortest inter-uranium distance is found in the basal plane, leading to strong uniaxial anisotropy. What remains still unclear is why the observed deuterium content is twice smaller comparing to the respective hydride.

To conclude, we proved by neutron diffraction experiment that our assumption about different hydrogen positions for the hydrides of UCoSn and URuSn is justified. Moreover, the determined crystal structures suggest why for UCoSn the effect of hydrogenation is much more pronounced than for URuSn.

c) Specific heat studies

For both $UCoSnD_{0.6}$ and $URuSnD_{0.6}$ deuterides the specific heat measurements were performed down to the $T = 2.2$ K. Both compounds show magnetic phase transitions, *i.e.* at $T = 98$ K for $UCoSnD_{0.6}$ and $T = 52$ K for $URuSnD_{0.6}$. The anomalies at specific heat are found at somewhat lower temperatures than obtained from the magnetic studies. The anomaly is more pronounced for $UCoSnD_{0.6}$, while for $URuSnD_{0.6}$ it is almost smeared out (Fig. 5.13).

The linear extrapolation of C_P/T vs T^2 dependence to $T = 0$ K let us estimate the γ coefficient of specific heat, which is connected with the density of states at the Fermi level $N(E_F)$ via the relationship:

$$\gamma = \frac{\pi^2}{3} N(E_F) k_B^2 .$$

For both compounds the γ coefficient increases upon deuteration and reaches 103 mJ/mol K^2 for $UCoSnD_{0.6}$ (compare to 61 mJ/mol K^2 for UCoSn [41]) and 75 mJ/mol K^2 for $URuSnD_{0.6}$ (50 mJ/mol K^2 for URuSn [41]). For $UCoSnD_{0.6}$ the linearity is observed in the range of T^2 between 20 K^2 and 280 K^2. Below $T^2 = 20$ K^2 a downturn is observed which would reduce the γ coefficient down to 79 mJ/mol K^2. However the lack of the data below $T = 2.2$ K does not allow us to be conclusive about the nature of this downturn. For $URuSnD_{0.6}$ C_P/T exhibits linear behaviour versus T^2 from the lowest measured temperatures up to $T^2 = 180$ K^2.

The information which was extracted from the specific heat measurement results does not give answers for the questions why deuteration has such diverse impact on both compounds, since in both cases it results in the increase of the density of states at the Fermi level. The reason

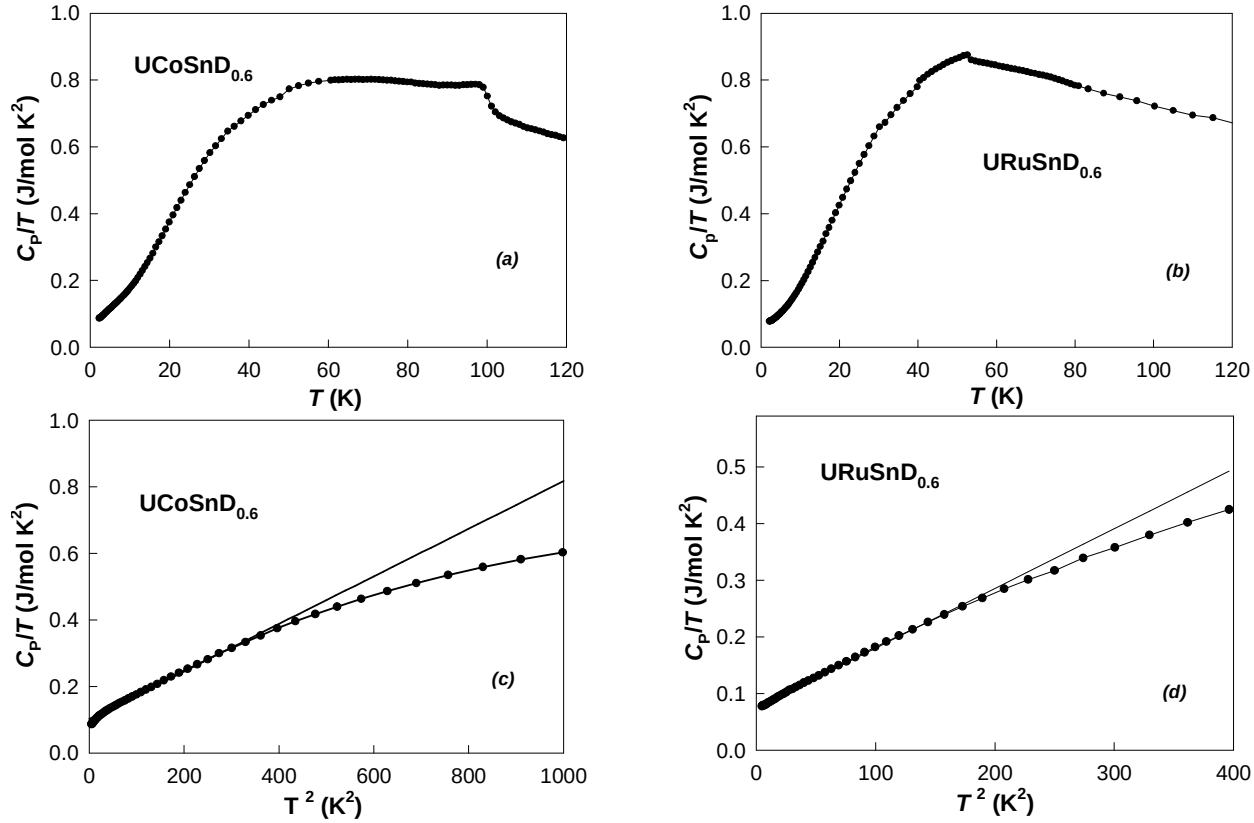

Fig. 5.13. Temperature dependence of specific heat C_P for $UCoSnD_{0.6}$ (a) and $URuSnD_{0.6}$ (b) and the dependence of C_P/T vs T^2 including the linear extrapolation to $T = 0$ K for $UCoSnD_{0.6}$ (c) and $URuSnD_{0.6}$ (d).

can be further localisation of the electronic levels (but one has to keep in mind that the experimental γ-value reflects $N(E_F)$ in the magnetically split state), the additional contribution of deuterium atom to the total density of states or the shift of the peaks of the electronic density (what might be an explanation for UCoSn).

d) Mössbauer spectroscopy studies

Mössbauer spectra for both $UCoSnD_{0.6}$ and $URuSnD_{0.6}$ were collected at room temperature and at $T = 4.2$ K, *i.e.* in the paramagnetic region and in the magnetically ordered state.

The room temperature Mössbauer spectra for both deuterides consist of absorption peaks shown on Fig. 5.14. The observed peaks could not be described by single lines. Therefore, a quadrupole splitting had to be considered in agreement with the low local symmetry of Sn atoms. The hyperfine parameters extracted from the fit, describing two Lorentzians with equal line widths and relative areas, are given in Table 5.6.

The hyperfine parameters of $UCoSnD_{0.6}$ and $URuSnD_{0.6}$ are close to the values obtained for the corresponding non-deuterated intermetallics. Both lines of the quadrupole doublets are unresolved since the corresponding widths are higher than the quadrupole splitting. The line-broadening for URuSn and $URuSnD_{0.6}$, which was measured at the same temperature is insignificant.

Table 5.6. Estimated hyperfine parameters (isomer shift *IS*, quadrupole splitting *QS* and line-width *Γ*) from the ^{119}Sn Mössbauer spectra of UCoSn, URuSn and respective deuterides obtained above the magnetic ordering temperature.

	T (K)	*IS* (mm/s)	*QS* (mm/s)	*Γ* (mm/s)
UCoSn[a]	80	1.75	0.56	0.93
$UCoSnD_{0.6}$[b]	300	1.78(1)	0.64(1)	0.96(2)
URuSn[a]	70	1.76	0.40	0.91
URuSn[b]	300	1.76(1)	0.42(2)	0.98(3)
$URuSnD_{0.6}$[b]	300	1.76(4)	0.39(2)	1.00(2)

[a] Data from Ref. 40. The isomer shift *IS* is relative to the $Ba^{119m}SnO_3$ source.
[b] Present work. The isomer shift *IS* is relative to the $Ca^{119m}SnO_3$ source.
Quadrupole splitting *QS* was calculated as $QS = \frac{1}{2} e^2 Q V_{zz}$.

The resonance spectra obtained at $T = 4.2$ K are shown on Fig. 5.15. The Mössbauer spectrum of $UCoSnD_{0.6}$ shows that besides the main phase with a well-defined magnetic hyperfine field there is a contribution from an impurity

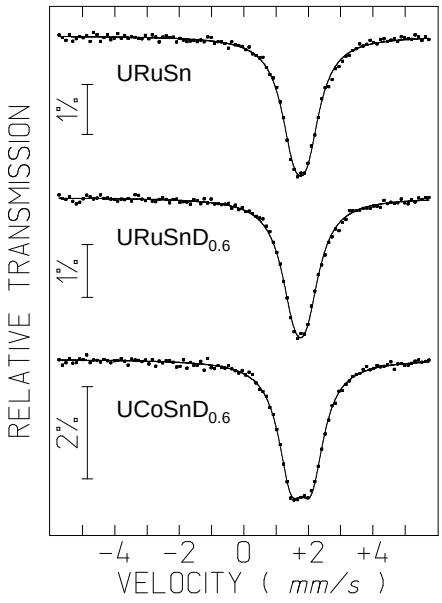

Fig. 5.14. ^{119}Sn Mössbauer spectra of URuSn, $URuSnD_{0.6}$ and $UCoSnD_{0.6}$ taken at room temperature. The calculated fit is shown by solid line.

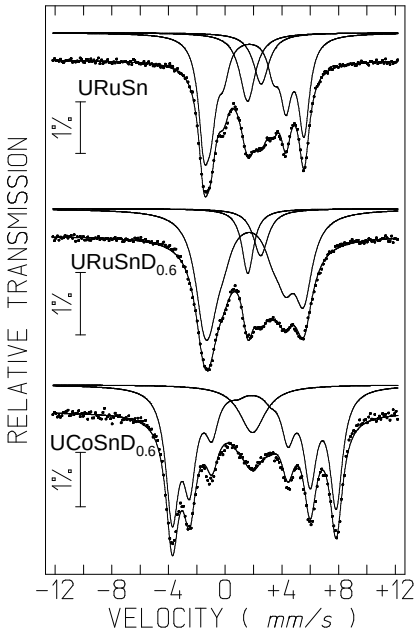

Fig. 5.15. ^{119}Sn Mössbauer spectra of URuSn, $URuSnD_{0.6}$ and $UCoSnD_{0.6}$ taken at $T = 4.2$ K. The calculated fit is shown by solid line.

phase in the middle of the spectra. Therefore it was necessary to reproduce the shape of the impurity component prior to the determination of the magnetic hyperfine field contributions of the main phase. The hyperfine interaction parameters for $UCoSnD_{0.6}$, obtained after this procedure, are presented in Table 5.7. In the magnetically ordered state, similar to the initial UCoSn compound, magnetic hyperfine field is found on the Sn site. Deuteration does not have well pronounced impact on the value of magnetic hyperfine field B_{hf}, while the values of quadrupole splitting and isomer shift are changed. The increase in IS between room temperature and 4 K obtained for the present data is expected due to the second order Doppler effect. The values of isomer shift for all compounds (including those discussed later) are significantly lower comparing to β-Sn (2.78(5) mm/s), which corresponds to lower *s*-state density at Sn nuclei. This could be understood as due to involvement of Sn states in the hybridisation. Then we can speculate that the increase of IS from UCoSn to $UCoSnD_{0.6}$ is due to the reduced hybridisation in the deuteride. The increase of the line width is more pronounced than for the samples measured at room temperature and might point to a higher degree of disorder in the deuteride or certain homogeneity region. The changes were observed for the parameters of electric field gradient (EFG). The direction of the main principal axis of EFG is not changed, but the remaining two principal axes are interchanged. For the Co-containing compound a slight improvement of the goodness of fit parameter was registered for the values of $\theta = 73^{o}$ and $\varphi = 23^{o}$. This improvement however is not significant and therefore there is not enough evidence to suggest a deviation of the direction of the main axes of the EFG that might be attributed to the presence of deuterium atoms in the crystal lattice. In fact, as they are not nearest neighbours of Sn atoms their presence should not have a strong effect on the EFG at the Sn nuclei.

Table 5.7. Estimated hyperfine parameters (hyperfine magnetic field B_{hf}, quadrupole splitting *QS*, asymmetry parameter of electric field gradient (EFG) η, isomer shift *IS*, angles θ and φ specifying the direction of B_{hf} with respect to the main principal axis of the EFG tensor, and line-width Γ) from the ^{119}Sn Mössbauer spectra of UCoSn, URuSn and respective deuterides obtained at $T = 4.2$ K.

	B_{hf} (T)	*QS* (mm/s)	η	*IS* (mm/s)	θ (deg)	φ (deg)	Γ (mm/s)
UCoSn[a]	8.40	-0.55	0.22	1.765	90	90	0.76
$UCoSnD_{0.6}$[b]	8.56(1)	-0.93(3)	0.36	1.89(4)	90	0	1.08(1)
URuSn[a]	5.16	+0.39	0.44	1.762	0	[c]	0.82
URuSn[b]	5.31(5)	+0.39(2)	0.45	1.84(3)	0	[c]	0.94(1)
$URuSnD_{0.6}$[b]	5.30(1)	+0.39(1)	0.35	1.81(1)	0	[c]	1.51(1)

[a] Data from Ref. 40. The isomer shift *IS* is relative to the $Ba^{119m}SnO_3$ source.
[b] Present work. The isomer shift *IS* is relative to the $Ca^{119m}SnO_3$ source.
[c] Undetermined value.

The fraction of Sn atoms in impurity phases in the Ru-containing samples was larger than in the $UCoSnD_{0.6}$. It should be noted that these impurities were already present in URuSn sample before deuteration. The comparison of hyperfine field parameters of URuSn and $URuSnD_{0.6}$ at T = 4.2 K showed that the influence of deuteration on their values is practically negligible. The only parameter, which is increased upon deuteration, is the line-width what can be explained by increased degree of disorder in deuteride. These results agree well with previous results – the intrusion of deuterium to the URuSn lattice does not affect hyperfine interactions either; therefore no dramatic changes of the magnetic properties could be expected.

5.1.4. Hydride of UCoSi: Crystal Structure and Magnetism

UCoSi has been chosen as a material for hydrogenation after successful studies of other compounds crystallizing in orthorhombic TiNiSi structure type UNiSi and UPdSi. Magnetic properties of these compounds are strongly affected by hydrogenation. UCoSi was reported to be a weak paramagnet, undoubtedly mainly due to a strong 5*f*-3*d* hybridization. This is contrasting with the magnetic order found in UNiSi and UPdSi, in which magnetic ordering temperatures increase upon hydrogenation. Therefore, it has been of certain interest to check whether hydrogenation and associated lattice expansion would not result in establishing of the magnetic order in UCoSi due to a 5*f* band narrowing.

UCoSi intermetallic compound was used as starting material for hydrogenation. The reaction was performed at hydrogen pressure 130 bar, and the thermal cycling up to T = 923 K was applied. For UCoSi-H, we performed two types of controlled decomposition experiments, during which the sample was annealed with a constant heating rate up to T = 923 K. In the first case, it was heated in dynamic vacuum, while in the second the sample was decomposed in a closed volume, which allowed to estimate the the maximum hydrogen content as (1.4±0.1) atom per formula unit. It is somewhat lower value than for UNiSi and UPdSi, for which the same

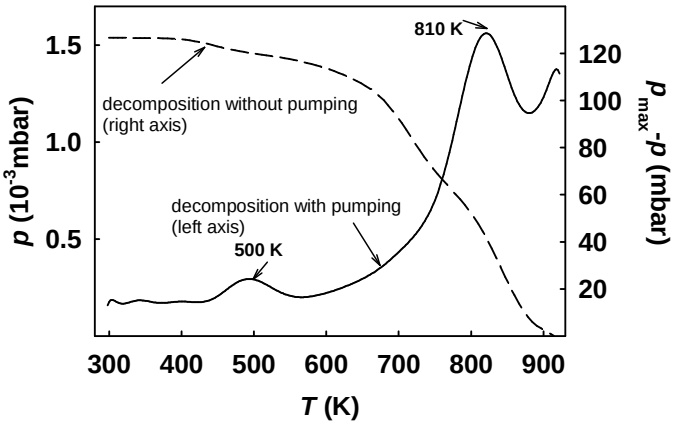

Fig. 5.16. Thermal desorption curve of $UCoSiH_{1.4}$ during heating in dynamic vacuum (solid line – left axis) and in closed volume (dashed line – right axis).

procedure leads to about 2.0 H atom per f.u.

As seen from Fig. 5.16, there are several characteristic stages of hydrogen desorption. The experiment in dynamic vacuum demonstrates each of them more clearly. The first desorption peak is located at T = 500 K, and the second, more pronounced one, at about 810 K. Moreover, there is a sign of a third desorption stage at even higher temperature, but it could not be completed due to limitations of the present experimental set-up.

Knowing the desorption characteristics, we prepared two intermediate hydrides by stopping the desorption after each decomposition maximum. The first intermediate hydride, obtained by the decomposition up to T = 573 K, has the stoichiometry $UCoSiH_{1.2}$, and the second one, obtained at T = 873 K, contains less than 0.1 H/f.u. (the sample is hereafter denoted as $UCoSiH_x$).

The structure of the parent compound UCoSi, as well as of all hydrides, was studied by means of X-ray diffraction on Siements D500 diffractometer (Co-K_α radiation). The X-ray powder patterns are presented on Fig. 5.17. The crystal structure analysis was performed using fullprofile Rietveld refinement. Its results are summarized in Table 5.8. In each sample small amounts of UCo_2Si_2 and another unidentified impurity phase were present.

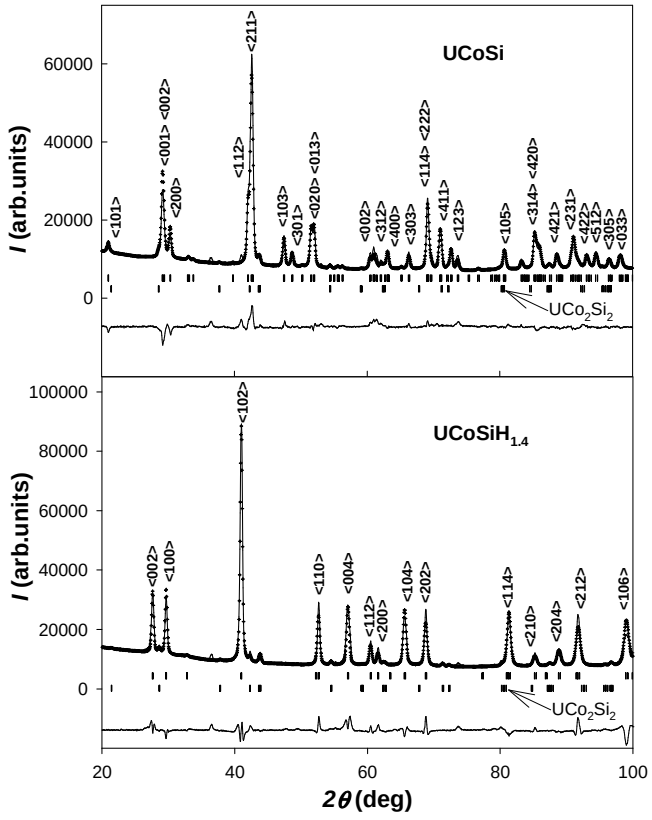

Fig. 5.17. X-ray powder patterns of UCoSi and $UCoSiH_{1.4}$ (Co-$K\alpha$ radiation).

Upon hydrogenation, UCoSi undergoes the same type of structure modification that was observed for UPdSi and UNiSi. The crystal symmetry increases, and $UCoSiH_{1.4}$ and $UCoSiH_{1.2}$ hydrides crystallize in the ZrBeSi structure type (space group $P6_3/mmc$). Another intermediate hydride $UCoSiH_x$ (x<0.1) has already the same structure type as the initial compound – orthorhombic TiNiSi type. Both ZrBeSi and TiNiSi structure types can be derived from the AlB_2 type. The relationship between the two types is illustrated on Fig. 5.18.

Both TiNiSi and ZrBeSi structure types consist of the layers of

uranium atoms and atoms of the transition metal and *p*-element in between. *T* and *X* atoms are located on the same height exactly between the uranium layers in ZrBeSi structure type, but they are shifted in TiNiSi structure type to opposite directions. Another displacement occurs within the uranium layers – they are arranged so to form the hexagonal unit cell in ZrBeSi structure type. In more details these transformations and the relationships between structures can be found in reference [78].

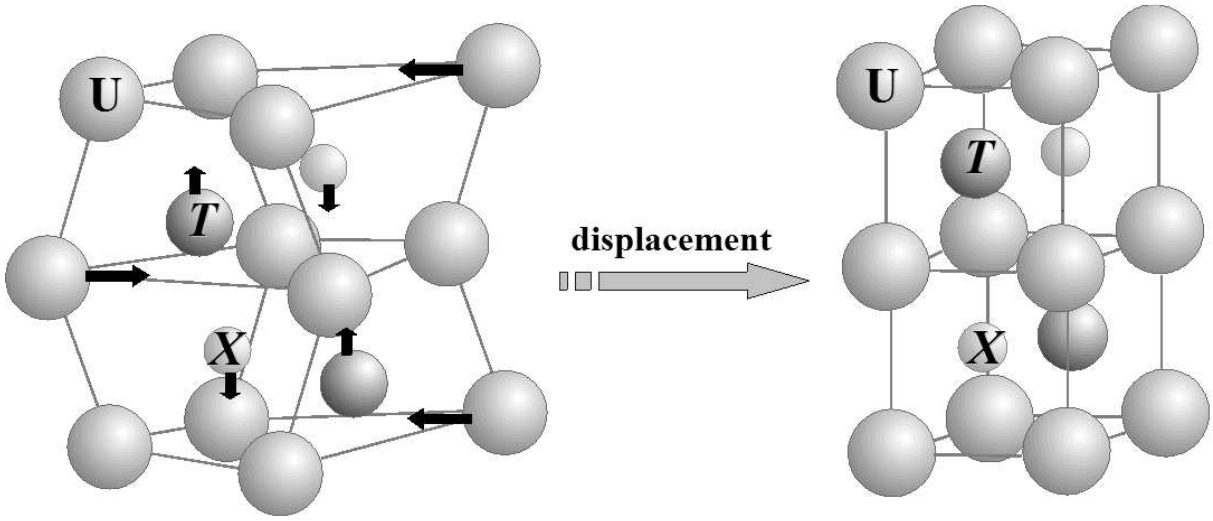

Fig. 5.18. The relationship between TiNiSi (*left*) and ZrBeSi (*right*) structure types.

Table 5.8. Comparison of crystal structure and magnetic susceptibility parameters of UCoSi and its hydrides. It gives lattice parameters *a*, *b*, and *c*, volume per formula unit, relative increase of volume with respect to UCoSi, inter-uranium spacing $d_{U\text{-}U}$, and parameters of the fit of the susceptibility in the modified Curie-Weiss regime (high *T*): effective moments μ_{eff}, paramagnetic Curie temperature Θ_p, and the *T*-independent term χ_0.

	$UCoSiH_{1.4}$	$UCoSiH_{1.2}$	$UCoSiH_x$ (x<0.1)	UCoSi
Structure type	ZrBeSi (hexagonal)	ZrBeSi (hexagonal)	TiNiSi (orthorhombic)	TiNiSi (orthorhombic)
a (pm)	403.78(4)	404.00(3)	684.17(5)	684.28(4)
b (Å)	-	-	411.48(4)	411.64(2)
c (Å)	749.76(6)	746.24(5)	705.48(7)	705.57(4)
Volume per f.u. (10^8pm)	52.93	52.74	49.65	49.69
$\Delta V/V$ (%)	6.52	6.14	-	-
$d_{U\text{-}U}$ (Å)	3.75	3.73	3.47	3.48
$\mu_{eff.}$(μ_B/f.u.)	2.2	1.2	1.3	1.6
Θ_p (K)	-98	-39	-110±20	-240±20
χ_0 ($10^{-8}m^3$/mol)	0.5	1.5	1.3	1.3

Magnetic susceptibility of UCoSi, $UCoSi_{1.4}$ and both intermediate hydrides was studied in various magnetic fields, using the Quantum Design PPMS extraction magnetometer. The

grains of the samples were fixed in random orientation. A small amount of ferromagnetic impurity existing already at T = 300 K was detected in all samples. The data presented here are corrected already for this impurity, the magnetization of which is only weakly increasing with decreasing T (Fig. 5.19).

The temperature dependence of magnetic susceptibility $\chi(T)$ of UCoSi exhibits more details compared to data published previously [49]. In the new data, we can distinguish three characteristic regions. In the high temperature range, i.e. for T > 100 K, $\chi(T)$ follows a modified Curie-Weiss (CW) behaviour with rather low effective moment μ_{eff} = 1.6 μ_B/f.u., and high negative paramagnetic Curie temperature $\Theta_p \approx$ -230 K. A temperature-independent term $\chi_0 = 1.3 \cdot 10^{-8}$ m^3/mol accounts for the curvature of $1/\chi$ vs. T. Below 100 K the susceptibility levels off, and this quite flat part extends down to 30 K, followed by an upturn, at which point the susceptibility starts to be field dependent. Higher fields tend to suppress the upturn.

The susceptibility exhibits more pronounced temperature dependence upon the hydrogenation for the synthesized hydrides. A detailed analysis shows, however, that the development is mainly quantitative. The Θ_p value shifts to less negative values (to about -100 K for $UCoSiH_{1.4}$), while the effective moment remains constant or somewhat increases (to about 2.1 μ_B/U in $UCoSiH_{1.4}$). One should be aware that the T-independent term in the CW law may in fact account for an anisotropy in the paramagnetic state, introducing thus an uncertainty in $\mu_{\text{eff.}}$ and θ_p values. Assuming that the susceptibility of a randomly oriented powder is given by averaging susceptibilities along main crystallographic directions, even if these are of purely CW type, the average can deviate from the CW dependence, leading to the type of bending of $1/\chi$ vs. T observed in our

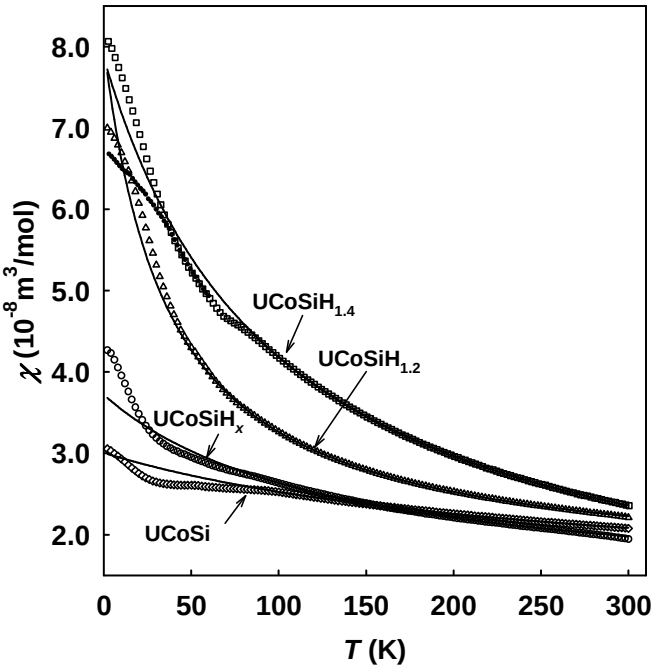

Fig. 5.19. Temperature dependence of magnetic susceptibility $\chi(T)$ for UCoSi and its hydrides, measured in $\mu_o H$ = 4 T. The solid lines represent the fits to modified Curie-Weiss law, mentioned in the text. For $UCoSiH_{1.4}$ also the susceptibility corrected for the low-T ferromagnetic impurity (small full dots) is displayed.

case. Then the parameters obtained by fitting are not fully physically meaningful. Another type of ambiguity can originate form the fact that the partially decomposed hydrides need not be fully homogeneous, and the hydrogen content can vary to some extent depending e.g. on the grain size.

The intermediate flat part of $\chi(T)$ shrinks with the increasing H concentration and the low-temperature upturn becomes emphasized.

An additional low-field AC susceptibility study (AC-field 0.01 T, frequency 1000 Hz) performed for UCoSi and $UCoSiH_{1.4}$ reveals ferromagnetic impurity with $T_C \approx 20$ K, which accounts for a part of the spontaneous magnetization (≈ 0.01 μ_B/f.u.) seen in Fig. 5.20. Correcting $\chi(T)$ for this impurity removes a large part of the upturn seen in $UCoSiH_{1.4}$, and we observe a saturation tendency in the low-T limit.

The magnetization curves shown in Fig. 5.20 exhibit one interesting feature, a downward curvature ($\frac{\partial^2 M}{\partial H^2} < 0$) developing gradually with increasing H concentration. Such phenomenon can be generally attributed either to spin fluctuations, suppressed by increasing field due to the Zeeman energy, or to the presence of few large weakly interacting paramagnetic ions contributing to the total magnetization by the Brillouin function. The existence of this curvature makes any correction for a ferromagnetic impurity rather tricky. It was therefore performed only for $UCoSiH_{1.4}$, for which the susceptibility was studied for many different field values.

Lower hydrogen content in the UCoSi hydride comparing to UNiSi and UPdSi, 1.4 H atoms per f.u., seems to be suggestive that we are close to the limits of hydrogen-absorbing area in the system of U*T*Si compounds for the given pressure range. Comparing with the U*T*Al compounds, we see that in both these cases the hydrogen absorbing area is restricted to *T* from the upper right corner of the transition-metal series. In the system of silicides, hydrogenation (also requiring high pressure) was confirmed for *T* = Ni, Pd, and Co, but probably does not extend

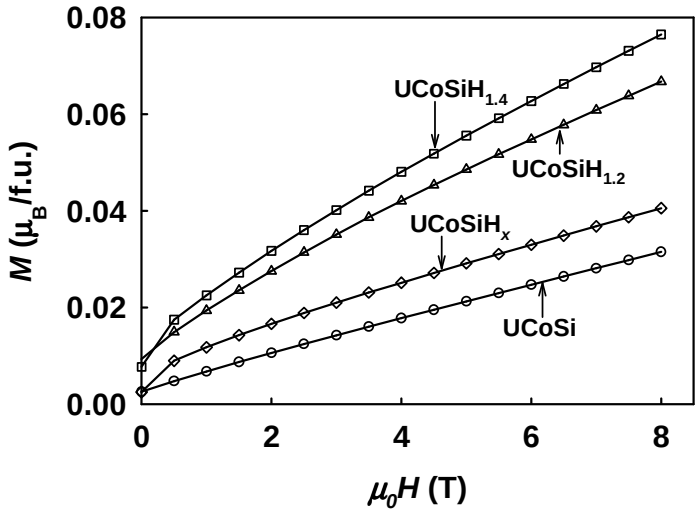

Fig. 5.20. Magnetization curves of UCoSi and its hydrides measured at $T = 2$ K with decreasing magnetic field.

further (UFeSi was not tested).

Our structure data can be also compared with rare-earth isotypes exhibiting similar structure transformations. As examples we can use TbNiSi, absorbing 1.78 D atoms per f.u. [92], $LaNiSnD_2$ [93], $CeIrGaH_{1.7}$ [94], $CeIrAlH_{2.0}$ [95], or $CeNiSnH_{1.8}$ [26]. Saturated hydrides of all these intermetallics contain about 2 H atoms/f.u. This corresponds to the maximum theoretical occupation of the R_3Ni tetrahedra. The hydrogen content of 1.4 for UCoSi evinces a lower affinity to hydrogen of this compound. We tend to attribute this difference, as compared to rare earth counterparts, to the 5*f*-*d* hybridisation and consequent bonding (which is more favourable comparing to bonding with H) rather than to the geometry of the lattice.

The decomposition study of $TbNiSiD_{1.78}$ shows only a single peak at $T = 470$ K [92]. Since two peaks were found for $UCoSiH_{1.4}$, it is not clear whether we could use this rare-earth system as full analogy for U*T*SiH_x, and we have therefore to assume details of the hydrogen positions as unknown.

Investigations of magnetic properties of UCoSi hydrides showed that even the full hydrogenation up to 1.4 H/f.u., and the related volume expansion by 6.5 %, are not sufficient to induce a magnetic ordering. One of the prominent factors in the 5*f* magnetism is the U-U spacing, which must be large enough to avoid formation of a broad 5*f* band. The change of the volume ΔV and the U-U spacing $\Delta d_{U\text{-}U}$ is less significant for UCoSi upon hydrogenation ($\Delta V = 6.5\%$, $\Delta d_{U\text{-}U} = 7.6$ %), than for UNiSi ($\Delta V = 8.2\%$, $\Delta d_{U\text{-}U} = 10.2$ %) and UPdSi ($\Delta V = 6.6\%$, $\Delta d_{U\text{-}U} = 19.8$ %), which may point to a weaker influence of hydrogenation on its magnetic behaviour. On the other hand, the U-U spacing of 3.7 Å is normally sufficient to allow a magnetic ordering of U lattice provided weak 5*f*-ligand hybridization. But the UCoSi hydrides remain paramagnetic, although their susceptibility becomes enhanced. This stresses the importance of the hybridisation in the whole UCoSi–H system.

A detailed analysis of $\chi(T)$ points to spin fluctuation phenomena. First, it is the large negative Θ_p of the Curie-Weiss term, which can be roughly associated with the characteristic energy of spin fluctuations $k_B T_{sf}$ [96]. Another gauge of spin-fluctuation effect is the characteristic temperature of the deviation from the modified CW law. Both parameters are reduced upon hydrogenation, pointing to an enhanced stability of U magnetic moments. Increasing stability of U moments is also corroborated by enhanced effective moment in the hydride. One should notice that except for very Co-rich systems, we usually do not consider Co moments in intermetallics containing U and Co, since the Co 3*d* states are filled to a much larger

extent in compounds with more electropositive elements. The filling of the 3d band reduces the density of the 3*d* states at the Fermi level below the level necessary for the 3*d* magnetism.

The development of magnetic properties can be followed in intermediate steps of the partly decomposed hydrides. In this case, the fitting parameters are not fully relevant, because the way of preparation does not guarantee a homogeneous distribution of hydrogen in the whole volume of the grains. But still the semi-quantitative comparison indicates a more or less monotonous development in the dependence on H content.

The studies of UCoSi completed the studies of the series of U*TX* hydrides. It was shown that the transition metal nature most probably determines the possibility of hydrogen absorption. The lattice modifications observed for UCoSi were not sufficient to induce the magnetic order in the synthesized hydrides.

5.2. Hydrides of U_2T_2X Compounds

The hydrogenation of U_2T_2X compounds was not studied before, but our choice was not accidental. The investigation of this group of compounds was initiated by the observation of hydrogen absorption for U_2Co_2Sn compound, which was found as a spurious phase during one of the early experiments on UCoSn. After it was discovered that the hydrogenation easily proceeds at available conditions and leads to relatively large lattice expansion and non-trivial changes of the magnetic properties of U_2Co_2Sn, we checked other compounds out of this series for hydrogen absorption, as well. Our further studies revealed hydrogen absorption also for U_2Ni_2Sn, U_2Ni_2In, U_2Co_2In, U_2Fe_2Sn, and U_2Pd_2In. Besides, it was found that U_2Pt_2In, U_2Ru_2Sn, U_2Ir_2Sn, and U_2Rh_2Sn do not absorb hydrogen under available conditions.

5.2.1. Hydrides of U_2Co_2Sn

U_2Co_2Sn intermetallic compound was used as starting material for hydrogenation. The main problem of the synthesis was to adjust the synthesis conditions, *i.e.* hydrogen pressure and temperature. The conventional synthesis at hydrogen pressure of 115 bar and T = 920 K resulted in the formation of two hydride phases with different lattice parameters.

The X-ray powder diffraction studies showed that both synthesized hydrides crystallize with the Mo_2FeB_2 structure type similar to the initial compound. Both AC- and DC-magnetization measurements were performed in the PPMS measurement system in the temperature range 2-300 K and in magnetic fields up to 9 T. Two magnetic transitions were

observed – an antiferromagnetic one at $T = 27$ K (determined as maxima on the susceptibility curve) and ferromagnetic one at approximately 33 K (a sharp peak at AC-susceptibility curve and remanent magnetization on magnetization curves below this temperature). We could conclude from the observation of the hydride with smaller hydrogen content as a spurious phase in UCoSn already that the ferromagnetic transition should be attributed to this phase, while the antiferromagnetic transition will be a feature of the hydride with higher hydrogen content. However, in order to study the properties of both hydrides, our prime task was to synthesize each hydride in pure state.

5.2.1.1. α-$U_2Co_2SnH_x$

It is rather uneasy task to prepare a homogeneous α-hydride, which is normally a solid solution of hydrogen in a mother compound, having hydrogen concentration variable up to a limit value, above which a β-phase starts to form. Therefore if too much hydrogen is introduced, β-phase forms as a spurious phase. Too small amount of hydrogen may cause the formation of the α-phase, but the modification may be not sufficient to induce the magnetic order. Therefore the prime task was to optimize the synthesis conditions.

One synthesis of α-$U_2Co_2SnH_x$ was performed at hydrogen pressure of 35 bar and with thermal treatment up to $T = 773$ K. Hydrogen content could not be determined precisely by decomposition in vacuum because it was on the verge of the error of the method, less then 0.1 H atoms/f.u., therefore we will represent the hydride as α-$U_2Co_2SnH_x$.

X-ray powder diffraction pattern showed that α-$U_2Co_2SnH_x$ crystallizes with Mo_2FeB_2 structure type similar to the initial compound. Small amount (≈10%) of hydride with larger volume expansion was detected. The crystal structure parameters are given in Table 5.9.

One synthesis of α-$U_2Co_2SnH_x$ was performed at hydrogen pressure of 35 bar and at thermal treatment up to $T = 773$ K. Hydrogen content could not be determined precisely by decomposition in vacuum because it was on the verge of the error of the method, less then 0.1 H atoms/f.u., therefore we will represent the hydride as α-$U_2Co_2SnH_x$.

X-ray powder diffraction pattern showed that α-$U_2Co_2SnH_x$ crystallizes with Mo_2FeB_2 structure type similar to the initial compound. Small amount (≈10%) of hydride with larger volume expansion was detected. The crystal structure parameters are given in Table 5.9.

α-$U_2Co_2SnH_x$ shows moderately anisotropic lattice expansion, which prevails along the *c*-axis. The shortest inter-uranium distance is along the *c*-axis and is equal to the lattice

Table 5.9. Structure and magnetic parameters of U_2Co_2Sn and its hydrides. Lattice parameters *a* and *c*, unit cell volume *V*, relative lattice expansion along a direction $\Delta a/a$, along *c* direction $\Delta c/c$ and relative volume expansion $\Delta V/V$ are given. $d_{U\text{-}U} \parallel c$ and $d_{U\text{-}U} \perp c$ are the nearest-neighbour U-U distances along the *c* axis and perpendicular to it, respectively. In all systems the shortest $d_{U\text{-}U}$ is along the *c*-axis. Parameters of the fit of the susceptibility in the modified Curie-Weiss (MCW) regime (high *T*): effective moments μ_{eff}, paramagnetic Curie temperature Θ_p, and the *T*-independent term χ_0.

	U_2Co_2Sn	α-$U_2Co_2SnH_x$	β-$U_2Co_2SnH_{1.4}$
a (pm)	729.1(1)	732.1(2)	751.0(2)
c (pm)	350.9(1)	353.2(1)	358.2(1)
V (10^8 pm^3)	1.866	1.893	2.020
$\Delta a/a$ (%)	-	0.4	3.0
$\Delta c/c$ (%)	-	0.6	2.1
$\Delta V/V$ (%)	-	1.4	8.2
x_U	0.171(1)	0.172(1)	0.176(1)
x_{Co}	0.373(2)	0.367(2)	0.379(3)
$d_{U\text{-}U} \perp c$ (Å)	352.6(10)	356.2(10)	363.1(10)
$d_{U\text{-}U} \parallel c$ (pm)	350.9(1)	353.2(1)	358.1(1)
μ_{eff} (μ_B/U)	1.6	1.1*	1.4*
θ_P (K)	-53	11*	35*
χ_0 (10^{-8}m^3/mol)	2.2	2.6*	2.3*

* MCW parameters should be considered rather qualitatively due to the phase inhomogeneities and magnetic inhomogeneities caused by chemical disorder on atomic scale.

parameter *c*. The inter-uranium distances are on the verge of the onset of magnetic order, *i.e.* within the Hill limit range similar to the initial compounds, but it may serve in the first approximation as a favourable factor for qualitative changes of magnetic properties.

The magnetic measurements for the initial compound and for both synthesized hydrides were performed in the temperature range 2-300 K and in the magnetic fields up to 9 T. All compounds exhibit modifies Curie-Weiss fit in the paramagnetic region and the corresponding parameters are given in Table 5.9. The data obtained for U_2Co_2Sn agree well with the literature data [53]. Magnetic susceptibility curve for α-$U_2Co_2SnH_x$ shows that it orders ferromagnetically

around 33 K with a very small detected moment (Fig. 5.21). The susceptibility curve did not reveal the features of the impurity phase, which was presumably antiferromagnetic.

The magnetization curve measured at $T = 2$ K (Fig. 5.22) on randomly oriented fixed powder indicated the presence of small spontaneous magnetic moment $\mu_s = 0.06\ \mu_B$/f.u., therefore we can use the label weak ferromagnetism for α-$U_2Co_2SnH_x$. Temperature dependence of magnetic susceptibility exhibits no tendency for saturation at low temperatures, what may indicate an inhomogeneity-related distribution of T_C values. This assumption was confirmed by AC-susceptibility measurements, which revealed a sharp maximum at 33 K and a broad peak in the temperature range of 2-30 K (Fig. 5.23). The broad peak at low temperatures did not appear, however, at the AC-susceptibility measurements performed for the sample synthesized at more rigid conditions (higher temperature and higher hydrogen pressure) containing both α-$U_2Co_2SnH_x$ (≈23%) and β-$U_2Co_2SnH_{1.4}$ (≈77%) (Fig. 5.24). For this sample a sharp well-pronounced peak is observed with maximum at 33 K. However, the presence of the second hydride phase does not allow us to evaluate with reasonable reliability structure parameters and

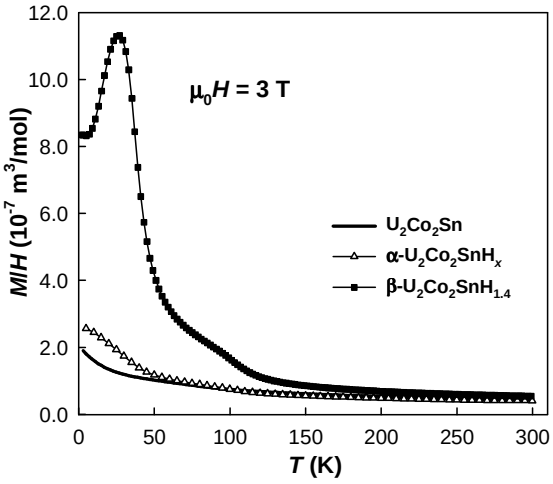

Fig. 5.21. Temperature dependence of magnetic susceptibility of U_2Co_2Sn, α-$U_2Co_2SnH_x$ and β-$U_2Co_2SnH_{1.4}$ in magnetic field 3 T after cooling in field. (The anomaly at $T \approx 100$ K corresponds to the Curie point of the $UCoSnH_{1.4}$ impurity phase.)

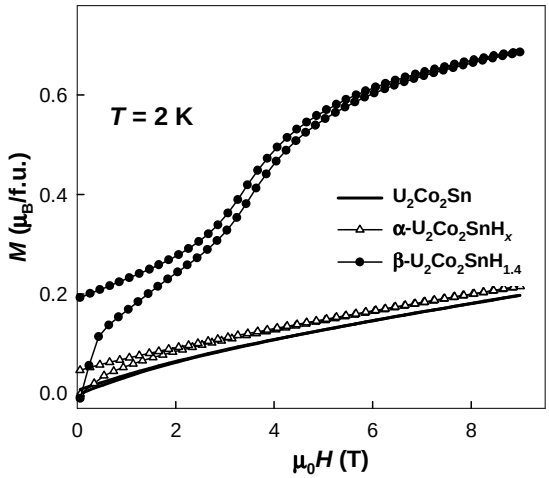

Fig. 5.22. Magnetization curves of U_2Co_2Sn, α-$U_2Co_2SnH_x$ and β-$U_2Co_2SnH_{1.4}$ measured at temperature $T = 2$ K.

remaining magnetic parameters. That's why the optimization of the synthesis process was particularly required.

The precise value of T_C was determined by the Arrott plot method (Fig. 5.25). The dependence of M^2 versus H/M exhibits linear fit at higher fields and the values of the

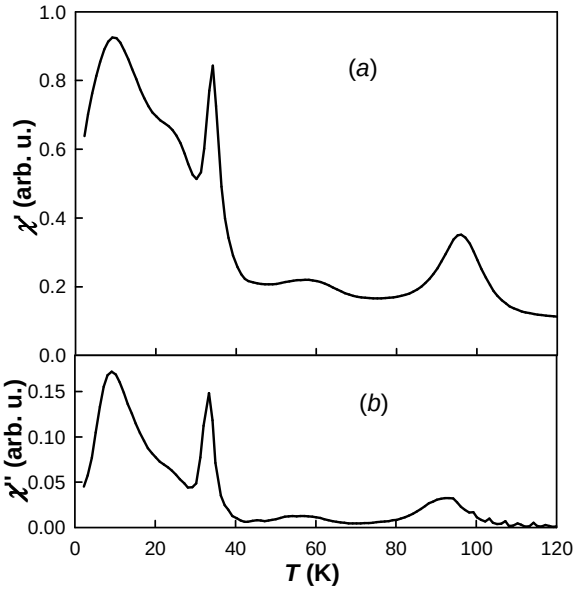

Fig. 5.23. Real (*a*) and imaginary (*b*) part of *ac*-susceptibility for α-$U_2Co_2SnH_x$ synthesized at hydrogen pressure 35 bar and temperature 773 K, measured at external field $\mu_0 H = 0$ T, AC-field 0.01 T, frequency 1000 Hz. (The anomaly at $T \approx 100$ K corresponds to the Curie point of the $UCoSnH_{1.4}$ impurity phase.)

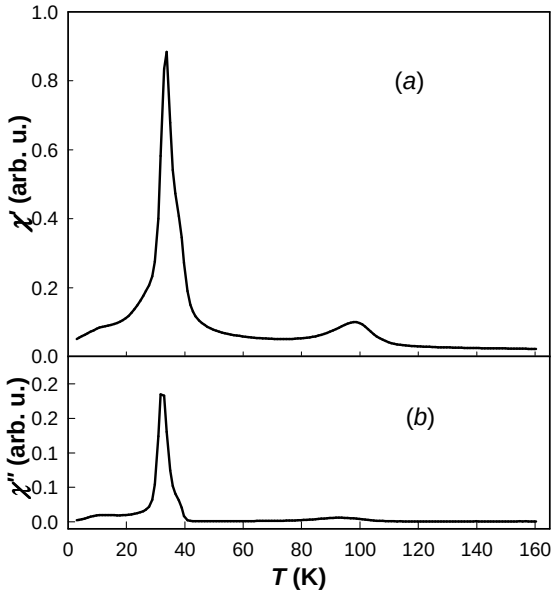

Fig. 5.24. Real (*a*) and imaginary (*b*) part of *ac*-susceptibility of a sample containing both α-$U_2Co_2SnH_x$ and β-$U_2Co_2SnH_{1.4}$, synthesized at hydrogen pressure 115 bar and temperature 920 K, measured at external field $\mu_0 H = 0$ T, AC-field 0.01 T, frequency 1000 Hz. (The anomaly at $T \approx 100$ K corresponds to the Curie point of the $UCoSnH_{1.4}$ impurity phase.)

extrapolated values of M^2 to zero field show linear dependence as well. The latter dependence yields the value of the Curie temperature $T_C = 33.5$ K.

Being ferromagnetic, α-$U_2Co_2SnH_x$ hydride occupies special place among other U_2T_2X compounds, since all magnetically ordered U_2T_2X compounds known are antiferromagnets. U_2Co_2Sn, being non-magnetic in non-hydrogenated state, is definitely at the verge of ferromagnetism, which has to influence the type of its spin fluctuations and features of the non-Fermi liquid physics. The moderate lattice expansion due to the formation of α-

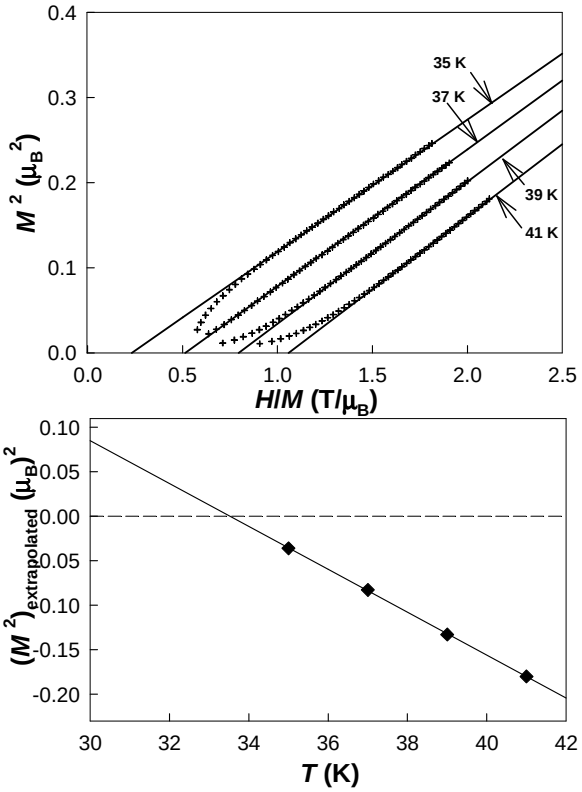

Fig. 5.25. Arrott plot for α-$U_2Co_2SnH_x$ hydride

hydride, let us assume that it is not primary pure volume effect which is responsible for dramatic changes in the magnetism of U_2Co_2Sn, but we conjecture that the contribution of small amount of hydrogen helps to stabilize existing interactions in the initial U_2Co_2Sn compound.

5.2.1.2. β-$U_2Co_2SnH_{1.4}$

β-$U_2Co_2SnH_{1.4}$ was prepared under hydrogen pressure of 120 bar and applying repeatedly thermal cycling up to T = 923 K. However, even under such conditions, the single phase sample was not obtained. The admixture of about 13% of α-$U_2Co_2SnH_x$ was detected by X-ray analysis. The hydrogen content was estimated by the decomposition in closed volume heating up to 923 K. Hydrogen desorption takes place at $T \approx 473$ K in one step (Fig. 5.26). The admixture of α-hydride prevented us from the determination of the exact amount of the absorbed hydrogen. The rough estimate of the H content for β-hydride gives 1.4(1) H atom/f.u.

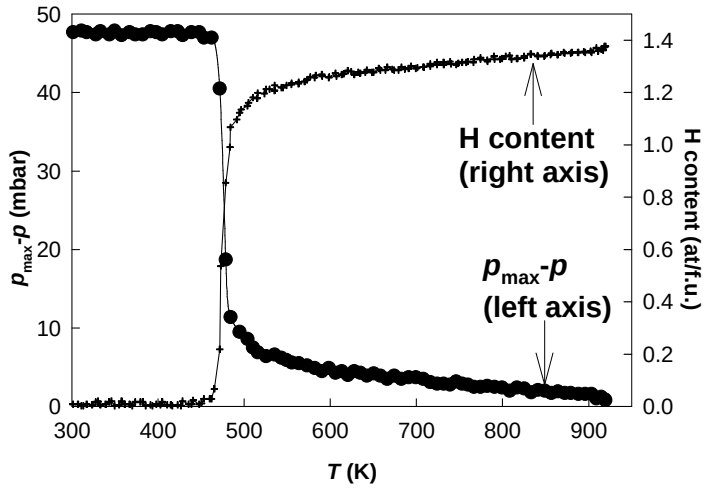

Fig. 5.26. Thermal decomposition curve of β-$U_2Co_2SnH_{1.4}$ measured in closed volume. The pressure drop in the system is showed by filled black circles (left axis). The consequent hydrogen content in the hydride is represented by crosses (right axis).

X-ray powder diffraction analysis showed that β-$U_2Co_2SnH_{1.4}$ crystallizes in Mo_2FeB_2 structure type similar to the initial compound, too. The crystallographic characteristics are given in Table 5.9. The lattice expansion is considerable – 8.2% with prevailing basal plane expansion. The shortest inter-uranium distance is equal to the lattice parameter c (358.1 pm), and this value may be sufficient for the formation of magnetic order.

Temperature dependence of magnetic susceptibility exhibits a pronounced maximum at T= 27 K, which can be attributed to an antiferromagnetic transition (Fig. 5.21). Antiferromagnetic order is typical for other magnetically ordered non-hydrogenated U_2Co_2Sn compounds. The magnetization curve (Fig. 5.22) has typical shape for an antiferromagnet, indicating a metamagnetic transition around 4 T at T = 2 K. The spontaneous magnetization

cannot be attributed solely to the presence of ferromagnetic α-$U_2Co_2SnH_x$ as an additional phase. Major part should be rather a consequence of highly defected structure due to large concentration of structure defects, effects of the strains on the grain boundaries, all probably consequently to the conditions of synthesis. Therefore the spontaneous magnetization may result from the existence of the uncompensated spins, in particular at the grain boundaries.

The onset of antiferromagnetic order in β-$U_2Co_2SnH_{1.4}$ can be attributed to the volume effect. The comparison of β-$U_2Co_2SnH_{1.4}$ and U_2Rh_2Sn [53, 58] can serve as a strong support for this assumption. U_2Rh_2Sn belongs to the same Mo_2FeB_2 structure type and crystallizes with lattice parameters a = 752.4 pm and c = 366.0 pm. These values are close to the values of lattice parameters for β-$U_2Co_2SnH_{1.4}$. The Néel temperature of U_2Rh_2Sn is 24 K, what is slightly lower than the ordering temperature of β-$U_2Co_2SnH_{1.4}$. Therefore we may conclude that for β-$U_2Co_2SnH_{1.4}$ the lattice expansion is the decisive factor determining the onset of the antiferromagnetic order.

The studies of the hydrides of U_2Co_2Sn compound were extremely important in several aspects. Firstly, origin was given to a new large group of uranium-based intermetallic hydrides. Secondly, it was shown how sensitive can be the magnetic properties of a certain compound to the perturbation and how qualitative can change the type of interactions in the compound, depending on the strength of perturbation. And finally, we showed, that although all magnetically ordered U_2T_2X compounds are antiferromagnets, small amount of hydrogen can stabilize ferromagnetic order in otherwise non-magnetic U_2Co_2Sn.

5.2.2. $U_2Ni_2SnH_{1.8}$ and $U_2Ni_2InH_{1.9}$ Hydrides

U_2Ni_2Sn and U_2Ni_2In intermetallic compounds were used as starting materials for hydrogenation. Hydrogenation of U_2Ni_2Sn was performed at hydrogen pressure 110 bar and applying thermal treatment up to T = 573 K for 3.5 hours. It was found that lower temperatures but longer exposition time prevented from the formation of UH_3 as a spurious phase. Hydrogenation of U_2Ni_2In was performed at hydrogen pressure 110 bar and applying thermal treatment up to T = 923 K.

Hydrogen content was determined by the decomposition in the closed volume and for both compounds the dynamics of hydrogen desorption looks almost similar. Hydrogen desorption starts at T = 420-450 K for both U_2Ni_2Sn (Fig. 5.27) and U_2Ni_2Sn (Fig. 5.28) hydrides and for both compounds the process of hydrogen desorption is complete by T = 600 K. The

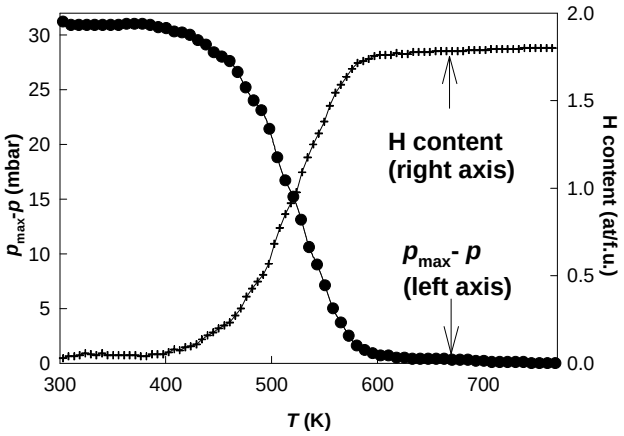

Fig. 5.27. Thermal decomposition curve of $U_2Ni_2SnH_{1.8}$ measured in closed volume. The pressure drop in the system is showed by filled black circles (left axis). The consequent hydrogen content in the hydride is represented by crosses (right axis).

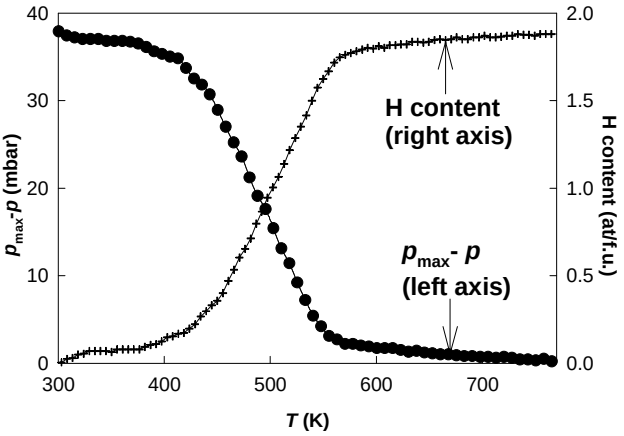

Fig. 5.28. Thermal decomposition curve of $U_2Ni_2InH_{1.9}$ measured in closed volume. The pressure drop in the system is showed by filled black circles (left axis). The consequent hydrogen content in the hydride is represented by crosses (right axis).

amount of hydrogen released was estimated as 1.8 H/f.u. for U_2Ni_2In and 1.9 H/f.u. for U_2Ni_2Sn. Taking into account the obtained stoichiometry, we assume that in an ideal case the composition should be $U_2Ni_2XH_2$.

X-ray powder diffraction experiment showed that for both compounds structure type does not change upon hydrogenation (Appendix E). U_2Ni_2Sn sample contained an unidentified phase which does not undergo any modifications upon hydrogenation. No additional phases have been found either for U_2Ni_2In or its hydride. The crystallographic parameters for U_2Ni_2Sn, U_2Ni_2In and respective hydrides are summarized in Table 5.10. The lattice expansion is large for both compounds and reaches 7.0% and 6.8% for U_2Ni_2Sn and U_2Ni_2In, respectively. In both cases lattice expansion is anisotropic, but for U_2Ni_2Sn it prevails in the basal plane, while for U_2Ni_2In lattice expands more along the *c*-direction. U_2Ni_2Sn takes a special place among other U_2T_2X compounds, since the shortest inter-uranium distance is found in the basal plane. The anisotropy of lattice expansion is not sufficient enough to change the direction of the shortest inter-uranium distance, but it brings the inter-uranium distance very close to the value of the lattice parameter *c* (*i.e.* the shortest inter-uranium distance perpendicular to the basal plane).

Magnetic measurements were performed on randomly oriented fixed powder in the magnetic fields up to 9 T for U_2Ni_2Sn and its hydride and up to 14 T for U_2Ni_2In and its hydride. The results obtained for the non-hydrogenated compounds agree well with the reported data, except for the effective moment for U_2Ni_2Sn, which was reported as 2.3 μ_B/U. Such a disagreement can be explained by the peculiarities of modified Curie-Weiss fit, which makes the

Table 5.10. Structure and magnetic parameters of U_2Ni_2Sn, U_2Ni_2In and respective hydrides. Lattice parameters *a* and *c*, unit cell volume *V*, relative lattice expansion along a direction $\Delta a/a$, along *c* direction $\Delta c/c$ and relative volume expansion $\Delta V/V$ are given. $d_{U\text{-}U} \parallel c$ and $d_{U\text{-}U} \perp c$ are the nearest-neighbour U-U distances along the *c* axis and perpendicular to it, respectively. The shortest inter-uranium distance is starred. Parameters of the fit of the susceptibility in the modified Curie-Weiss (MCW) regime (high *T*) (effective moment μ_{eff}, paramagnetic Curie temperature Θ_p, and the *T*-independent term χ_0) and Néel temperature T_N are listed.

	U_2Ni_2Sn	$U_2Ni_2SnH_{1.8}$	U_2Ni_2In	$U_2Ni_2InH_{1.9}$
a (pm)	726.2(1)	744.5(2)	739.1(1)	754.7(1)
c (pm)	369.5(1)	376.4(1)	357.6(1)	366.2(1)
V (10^8 pm^3)	1.949(1)	2.086(1)	1.953(1)	2.086(1)
$\Delta a/a$ (%)	-	2.5	-	2.1
$\Delta c/c$ (%)	-	1.9	-	2.4
$\Delta V/V$ (%)	-	7.0	-	6.8
x_U	0.173(1)	0.177(1)	0.171(1)	0.177(1)
x_{Ni}	0.378(3)	0.376(3)	0.358(4)	0.375(1)
$d_{U\text{-}U} \perp c$ (pm)	355.3(10)*	372.7(11)*	359.6(10)	377.8(11)
$d_{U\text{-}U} \parallel c$ (pm)	369.5(1)	376.4(1)	357.6(1)*	366.2(1)*
μ_{eff} (μ_B/U)	2.6	2.2	2.2	2.2
θ_P (K)	-137	-36	-87	-56
χ_0 (10^{-8}m^3/mol)	0.7	1.2	1.5	1.6
T_N (K)	26	87	14	60

parameter very sensitive to the fitting procedure. The value of the effective moment shows that synthesized hydrides are still below the localization limit and paramagnetic Curie temperature remains negative as should be expected for antiferromagnets without any preferable ferromagnetic coupling between the nearest neighbours. The magnetic measurements showed that both hydrides order antiferromagnetically similar to the initial compounds. The ordering temperature was determined as the position of maximum on the susceptibility curve (Fig. 5.29). The considerable increase of the ordering temperature is observed for both hydrides: the Néel temperature reaches 87 K for $U_2Ni_2SnH_{1.8}$ comparing to 26 K for U_2Ni_2Sn and 60 K for $U_2Ni_2InH_{1.9}$ comparing to 14 K for U_2Ni_2In. The susceptibility curve of $U_2Ni_2SnH_{1.8}$ is characterized by upturn at lower temperatures not typical for antiferromagnets, which can be

explained by the existence of non-compensated magnetic moments or clusters, which behave like paramagnets still below the ordering temperature. Also some tendency for saturation is observed with the decrease of temperature. There is trace of ferromagnetic UH_3 in the $U_2Ni_2InH_{1.8}$ sample what can be seen from the anomaly at 180 K. The ordering temperatures for both $U_2Ni_2SnH_{1.8}$ and $U_2Ni_2InH_{1.9}$ exceed much those for the non-hydrogenated antiferromagetic U_2T_2X compounds.

The variations of the magnetization curves upon hydrogenation have different character for the two hydrides (Fig. 5.30). Magnetization curve of $U_2Ni_2SnH_{1.8}$ at T = 2 K shows a more pronounced stronger field dependence than in the non-hydrogenated state. Magnetization curve shows a broad S-shape, however it is still far from the saturation at $\mu_0 H$ = 9 T. The field of presumable metamagnetic transition of around 4 T is close to the value observed before for β-$U_2Co_2SnH_{1.4}$. Such a behaviour can be considered from the point of view of structure modifications. The antiferromagnetic coupling gets weaker due to certain frustrations because the shortest inter-uranium distance is not so pronounced in the hydride as in U_2Ni_2Sn. The existing interactions may be possibly disturbed by the concomitant interactions in the perpendicular direction due to the proximity of uranium atoms.

For $U_2Ni_2InH_{1.9}$ the situation is opposite. The magnetization curve at T = 2 K is less field dependent comparing to U_2Ni_2In. It can point out that antiferromagnetic coupling gets stronger.

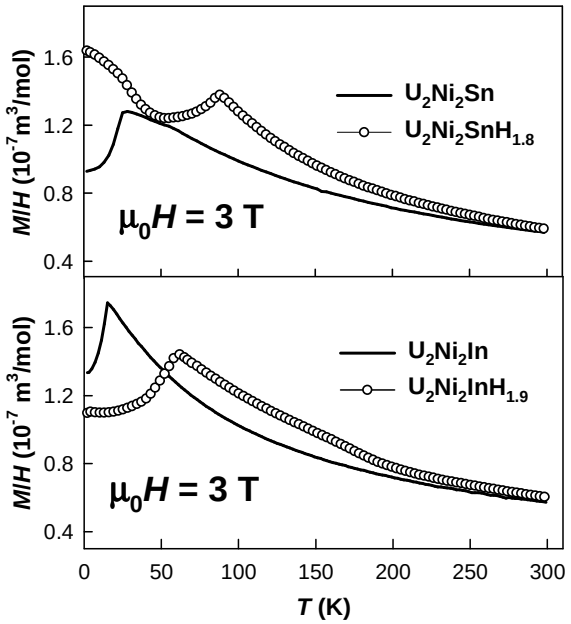

Fig. 5.29. Temperature dependence of magnetic susceptibility for U_2Ni_2Sn and $U_2Ni_2SnH_{1.8}$ (upper panel) and U_2Ni_2In and $U_2Ni_2InH_{1.9}$ (lower panel) measured in magnetic field 3 T.

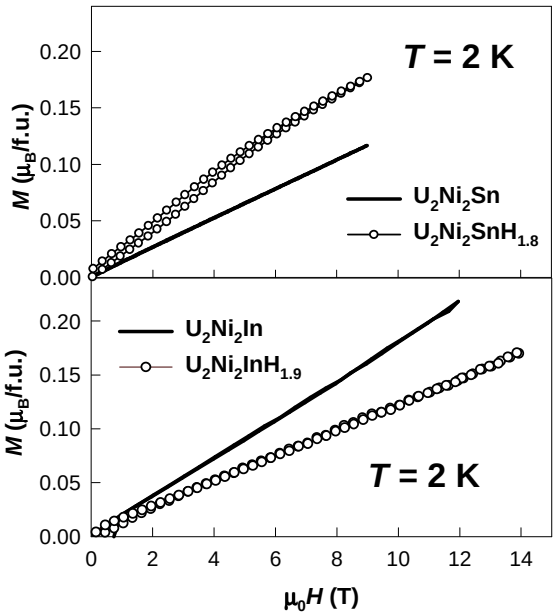

Fig. 5.30. Magnetization curves of U_2Ni_2Sn and $U_2Ni_2SnH_{1.8}$ (upper panel) and U_2Ni_2In and $U_2Ni_2InH_{1.9}$ (lower panel) measured at temperature 2 K.

There is no trace of any metamagnetic transition, which is probably shifted still to higher field than 27 T found for U_2Ni_2In, or any tendency for saturation up to magnetic field 14 T.

The discovery of U_2Ni_2X hydrides expanded the series of known hydrides of U_2T_2X compounds. It was shown that although hydrogenation does not force any qualitative changes in the magnetic properties of U_2Ni_2X, it has very considerable quantitative impact. The increase of the ordering temperatures by the factor of 3-4 and the absolute values exceeding the ordering temperatures for the known U_2T_2X compounds can be partly explained by the large volume effect of 7.0% for U_2Ni_2Sn and 6.8% for U_2Ni_2In. The lattice expansion leads to the enhanced U–U spacing, reducing the 5*f*-5*f* overlap and/or reducing the 5*f*–3*d* hybridisation. However, the comparison with the volume expansion $\Delta V/V$ 8.2% observed for β-$U_2Co_2SnH_{1.4}$ leads to the conclusion that hydrogen absorption does not result in mere lattice expansion. The bonding of hydrogen atoms with transition metal atoms via the formation of 1*s*-*d* bond and consequent partial withdrawal of *d*-states from the hybridised band leads to decrease of the strength of 5*f*-3*d* hybridisation. Our observations showed that the volume effect for Co compounds is larger comparing to the Ni compounds even in spite of somewhat smaller hydrogen content. Taking into account that the strength of 5*f*-3*d* hybridisation increases as we move to the left through the transition metal series, *i.e*. in a sequence Ni–Co–Fe, we conclude that the decrease of the strength of 5*f*-3*d* hybridisation plays an important role in the localization of the uranium magnetic moments and in the modifications of the properties of synthesized hydrides. And consequently, it provides also a ground for the assumption that U_2Co_2In and U_2Fe_2Sn can exhibit extraordinary modifications upon hydrogenation.

5.2.3. $U_2Ni_2SnD_{1.8}$ Deuteride

The main reason for the synthesis of deuteride of U_2Ni_2Sn was to carry out the powder neutron diffraction experiment. The obtained data can provide us an important information on the crystal (deuterium positions) and magnetic (the arrangement of magnetic moments) structure.

U_2Ni_2Sn intermetallic compound was used as starting material for deuteration. The synthesis procedure was the same like for hydrogenation, except for longer activation time due to larger surface area and longer time of thermal cycling (in total 10 hrs) because of considerably larger amount of the sample (over 10 g). The pressure of deuterium introduced was 92 bar. A small part of the sample was decomposed in the closed volume for the estimation of the amount of absorbed deuterium. The deuterium concentration reached 1.8±0.1 H (D) atoms per formula unit, similar to the respective hydride.

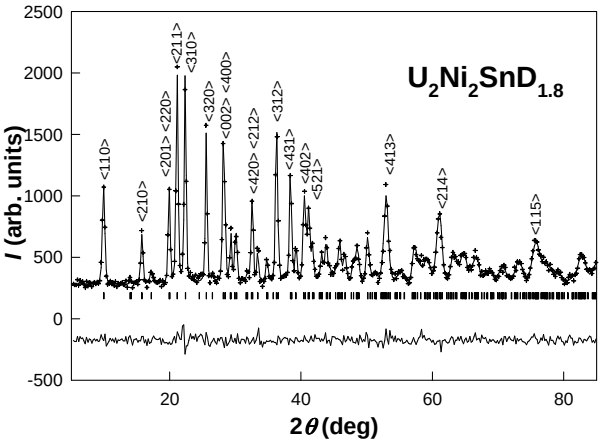

Fig. 5.31. Neutron diffraction pattern of $U_2Ni_2SnD_{1.9}$ (λ = 92 pm). The observed values are shown by crosses and calculated by solid line. Difference diffraction pattern is presented. R_B = 4.22%

Prior to the neutron diffraction experiment the phase composition and crystal structure was studied by X-ray powder diffraction (Cu-$K\alpha$ radiation). The pattern showed small amount of spurious unidentified phase, which is not modified upon hydrogenation. The lattice parameters, listed in Table 5.11, are very close to the values observed for $U_2Ni_2SnH_{1.8}$.

Neutron powder diffraction pattern for crystal structure determination (Fig. 5.31) was obtained using a copper monochromator (λ = 92 pm) in the angle range 2θ = 5–84.6º at T = 120 K (*i.e.* above the antiferromagnetic transition). Taking into account just metallic atoms, $U_2Ni_2SnD_{1.8}$ crystallizes in the tetragonal Mo_2FeB_2 structure type similar to the initial compound and to $U_2Ni_2SnH_{1.8}$. The refinement of the diffraction pattern revealed that the additional position for the deuterium atom is 8*k* site inside the U_3Ni tetrahedral (Table 5.11). Two neighbouring tetrahedra are coupled by the shared face. However, simultaneous occupation of both neighbouring (8*k*) sites would contradict at least two known rules: the distance between two sites is 25 pm what is an order of magnitude lower, than empirically determined minimal distance between the hydrogen atoms of 210 pm, and secondly – according to the "Shoemaker's exclusion rule" two tetrahedra

Table 5.11. Lattice parameters *a* and *c*, unit cell volume *V*, relative lattice expansion along the *a* direction $\Delta a/a$, along the *c* direction $\Delta c/c$, relative volume expansion $\Delta V/V$ of $U_2Ni_2SnH_{1.8}$ and $U_2Ni_2SnD_{1.8}$ measured at room temperature, and internal parameters *x*, *y*, *z*, thermal parameters *B* and the coefficients of the site occupancy *n*, obtained from neutron diffraction of $U_2Ni_2SnD_{1.8}$ at 120 K (R_B = 4.22 %).

U_2Ni_2Sn		a = 726.3(1) pm	c = 369.5(1) pm		$V = 1.949\cdot10^8$ pm^3	
$U_2Ni_2SnH_{1.8}$		a = 744.5(1) pm	c = 376.4(1) pm		$V = 2.086\cdot10^8$ pm^3	
		$\Delta a/a$ = 2.5 %	$\Delta c/c$ = 1.9 %		$\Delta V/V$ = 7.0 %	
$U_2Ni_2SnD_{1.8}$		a = 743.5(1) pm	c = 376.1(1) pm		$V = 2.079\cdot10^8$ pm^3	
		$\Delta a/a$ = 2.4 %	$\Delta c/c$ = 1.8 %		$\Delta V/V$ = 6.7 %	
Atom	Site	x	y	z	B (10^6 pm^3)	n
U	4*h*	0.1788(6)	0.6788(6)	0.5	0.33	1
Ni	4*g*	0.3747(5)	0.8747(5)	0	0.58	1
Sn	2*a*	0	0	0	0.24	1
D	8*k*	0.3859(10)	0.8859(10)	0.5338(63)	0.92	0.448(6)

sharing the same face cannot be occupied simultaneously. This agrees well with the value of the coefficient of site occupancy which shows that the deuterium sites are occupied less for one half. Therefore we assume that only one of two neighbouring tetrahedra is randomly occupied and in the ideal case the occupancy of (8k) site would reach 50%. Any attempts to fit the powder pattern with deuterium atoms at (4*h*) position (*x*; *x*+0.5, 0.5) with triangular bipyramid consisting of three uranium and two nickel atoms as coordination sphere were unsuccessful and the goodness of fit was unsatisfactory. Besides, in the terms of the suggested structure it is better understood the lattice expansion both in the basal plane and along the *c* axis. In case deuterium atoms occupied the 4*h* position, there would be no evident reason for the lattice expansion along the *c*-axis. The representation of the crystal structure of $U_2Ni_2SnD_{1.8}$ is shown on Fig. 5.32. The table of interatomic distances is given in the Appendix F. As it is seen the nearest neighbour of deuterium atom is nickel, what could support the idea of the formation of 1*s*-*d* bond. And for deuteride the proximity of the inter-uranium distances within the basal plane and perpendicular to it is even more pronounced than for the hydride.

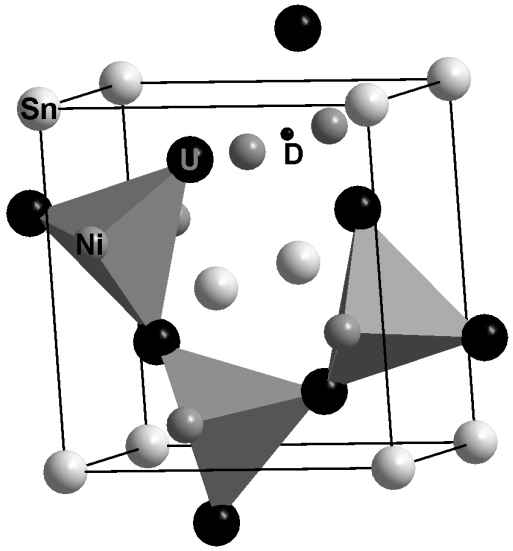

Fig. 5.32. Crystal structure of $U_2Ni_2SnD_{1.8}$. Coordination sphere of deuterium atoms is constructed.

The crystallographic stoichiometry obtained from the Rietveld refinement yields the value of 1.79(2) hydrogen atoms per formula unit, what agrees well with the results of the volumetric method.

Magnetic measurements were performed by means of the SQUID magnetometer in the temperature range 5-300 K and in the magnetic field up to 5 T. It was show that $U_2Ni_2SnD_{1.8}$ orders antiferromagnetically at $T_N = 87$ K (determined as maximum in $\chi(T)$) similar to $U_2Ni_2SnH_{1.8}$ (Fig. 5.33). The upturn at low temperatures, which was attributed to non-compensated spins at grain boundaries or structure defects, is less pronounced for the deuteride. It may be a consequence of larger grain size. The susceptibility of $U_2Ni_2SnD_{1.8}$ is shifted up compared to $U_2Ni_2SnH_{1.8}$ due to the presence of a small amount of UD_3 ($T_C \approx 180$ K) as a spurious phase. We can conclude that magnetic properties of U_2Ni_2Sn hydride and deuteride are practically identical, which means that all structure information obtained for the deuteride represents also the hydride.

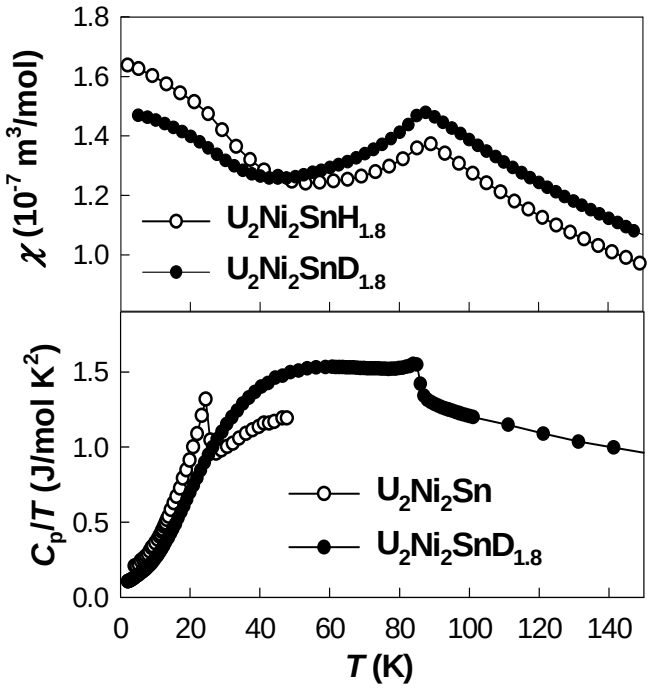

Figure 5.33. Temperature dependence of magnetic susceptibility for $U_2Ni_2SnH_{1.8}$ (μ_0H = 3 T) and $U_2Ni_2SnD_{1.8}$ (μ_0H = 4 T, upper panel), and specific heat C_p of U_2Ni_2Sn and $U_2Ni_2SnD_{1.8}$ (lower panel).

The neutron diffraction powder pattern for the magnetic structure studies was measured at T = 1.8 K (below the ordering temperature) using graphite monochromator (λ = 239.6 pm). The results were compared with the same data obtained at T = 120 K (i.e. above the T_N). The diffraction patterns are presented on Fig. 5.34. Surprisingly, unlike pure U_2Ni_2Sn, which exhibited additional magnetic reflection (1/2, 1/2, 1/2) in neutron diffraction pattern collected in the ordered state [54], no additional reflections were observed for $U_2Ni_2SnD_{1.8}$ at T = 1.8 K. This means that deuterition results in the modifications of the magnetic structure and the unit cell doubling along *c*, indicated at U_2Ni_2Sn, is lost in the deuteride.

The analysis of the magnetic structure was based on the measured bulk properties (*i.e.* antiferromagnetic coupling) and on the fact that the magnetic and crystallographic unit cells have to be identical. Fig. 5.35 presents the possible magnetic structures, derived from the group theory. Two collinear structures – ferromagnetic (FC) and antiferromagnetic (AFC) – contain uranium magnetic moments parallel to the *c*-axis. Four noncollinear structures are characterized by magnetic moments lying in the basal plane. The collinear ferromagnetic structure FC (*a*) was disregarded taking into account the magnetisation measurements. And for

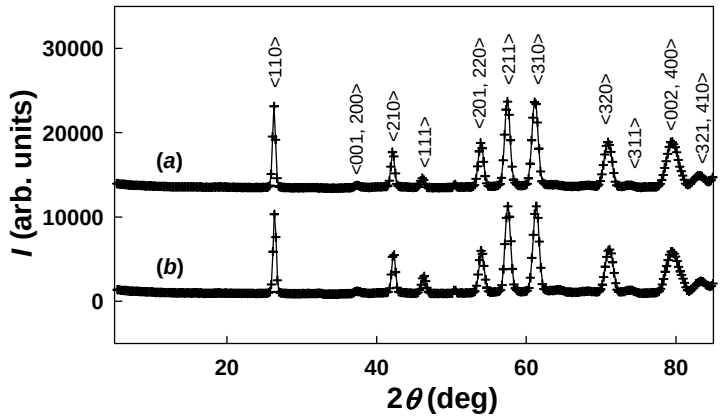

Fig. 5.34. Neutron powder diffraction patterns (λ = 239.6 pm) of $U_2Ni_2SnD_{1.8}$ measured at T = 120 K (*a*) and 1.8 K (*b*).

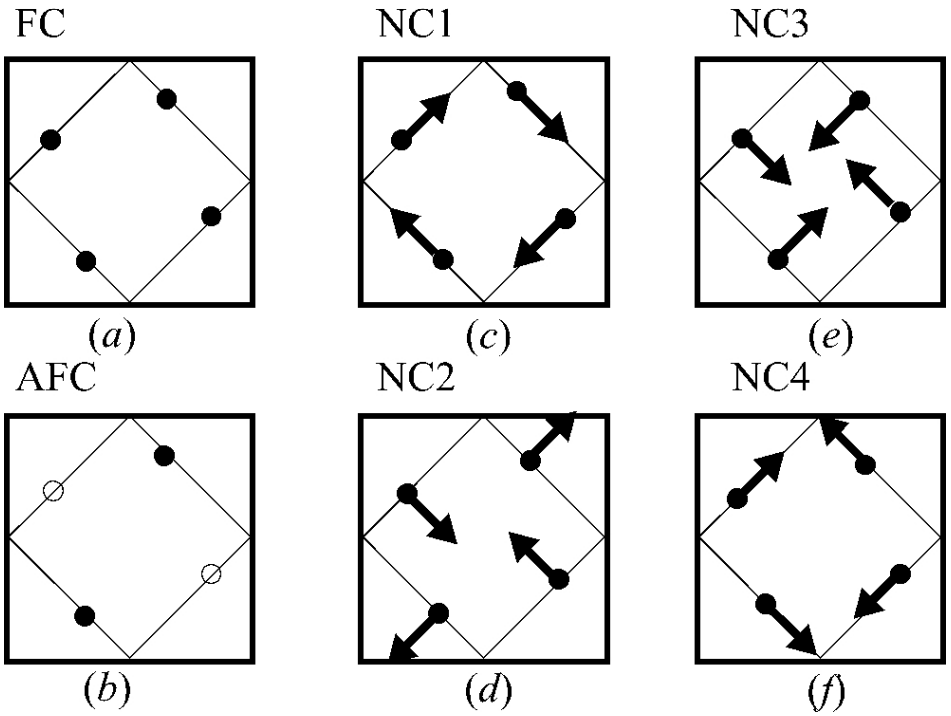

Fig. 5.35. Projections on the tetragonal plane of two collinear Shubnikov subgroups – *c*-axis ferromagnetic FC (*a*) and *c*-axis antiferromagnetic AFC (*b*), and four non-collinear Shubnikov subgroups (*c*-*f*) for the uranium 4*h* sites (space group *P4/mbm*). The magnetic moments are represented as full circles if the moments are pointing out of the plane of paper and as empty circles for the moments pointing into the plane of paper.

the collinear antiferromagnetic structure, which has uranium, moments along *c*-axis (AFC) the quality of the fit was at least twice worse than for the other models allowed by symmetry (*c*-*f*). No significant difference was observed between the goodness of fit parameters for four non-collinear structures, the value of magnetic *R*-factor reached 15-16%. Therefore we can conclude that the best fit was found for the model having non-collinear uranium moments of 0.8(3) μ_B within the basal plane. The size of the moments can be thus somewhat smaller than in U_2Ni_2Sn, which is characterized by uranium magnetic moment of 1.05 μ_B. Similar magnetic structure was found for U_2Pd_2In [60], for which the NC4 structure was determined as the correct one (Fig. 5.35, *f*), and we accept this structure as the most probable due to somewhat better goodness of fit (magnetic *R*-factor 15.1%). This structure yields ferromagnetic coupling between the layers of uranium atoms (along the *c* direction) and antiferromagnetic coupling within the layer.

The ^{119}Sn Mössbauer spectroscopy studies were performed in order to confirm the suggested magnetic structure. Mössbauer spectra consist of an absorption peak, shown on Fig. 5.36. Trying to fit this peak with a single Lorentzian leads to a very poor adjustment between the calculated curve and the experimental points. In fact the observed absorption peak is a quadrupole doublet, consistent with Sn occupying a crystallographic site with non-cubic

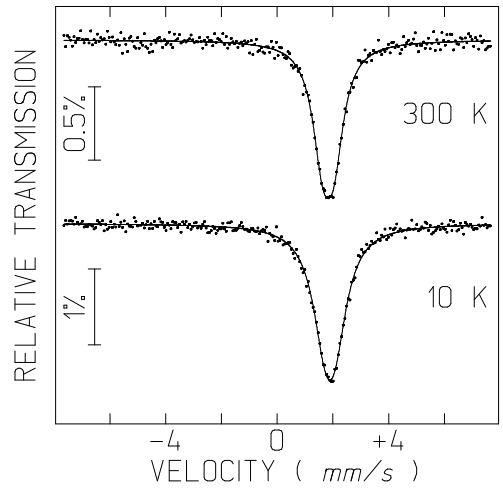

Fig. 5.36. ^{119}Sn Mössbauer spectra of $U_2Ni_2SnD_{1.8}$ taken at room temperature and 10 K. The calculated function plotted on the experimental points is a quadrupole doublet (estimated parameters in table 5.12)

symmetry, and similar to that observed in the non-hydrogenated U_2Ni_2Sn [54]. The estimated hyperfine parameters in Table 5.12 are obtained performing the refinement with two Lorentzians with equal line widths and relative areas. Both lines of the quadrupole doublet are unresolved as the corresponding width is larger than the quadrupole splitting. IS and QS values are similar to those reported for U_2Ni_2Sn while line widths are slightly larger which may be related to a higher degree of disorder caused by deuteration.

As in U_2Ni_2Sn, in the present deuterated compound there is no resulting magnetic hyperfine field B_{hf} at the Sn atoms even at temperatures as low as 10 K. This implies that the sum of the U magnetic moments surrounding the Sn atoms is zero at the Sn atom site. The ordered magnetic structure of $U_2Ni_2SnD_{1.8}$ is therefore consistent with this observation.

Specific heat measurements were performed using the PPMS measuring system in the temperature range 1.8-300 K. $U_2Ni_2SnD_{1.8}$ showed a pronounced magnetic anomaly at $T = 85$ K (Fig. 5.33). Although the magnetic entropy could not be evaluated exactly due to a non-Debye-like phonon specific heat, the comparison of the anomaly with U_2Ni_2Sn (data taken from Ref. 55) reveals that it remains a small fraction of $R\ln 2$, meaning that the itinerant character of magnetism is preserved. The γ coefficient obtained from the linear extrapolation of C/T to $T = 0$ K is 105 mJ/mol f.u. K^2, *i.e.* lower than the

Table 5.12. Estimated parameters from the ^{119}Sn Mössbauer spectra of $U_2Ni_2SnD_{1.8}$ obtained at different temperatures

T (K)	IS (mm/s)	QS (mm/s)	Γ(mm/s)
297	1.83	0.40	0.88
110	1.87	0.37	0.90
80	1.89	0.37	0.92
70	1.88	0.41	0.91
55	1.89	0.39	0.99
40	1.89	0.38	1.06
10	1.89	0.36	1.09

IS isomer shift relative to $CaSnO_3$ at 295 K; QS quadrupole splitting; Γ line-widths. Estimated errors are ≤ 0.02 mm/s for IS and QS, ≤ 0.06 mm/s for Γ.

value for U_2Ni_2Sn – 172 mJ/mol f.u. K^2. This observation points to the reduction of the density of states on the Fermi level, what might be a consequence of the localization tendency of the uranium electronic states.

To conclude, the studies of $U_2Ni_2SnD_{1.8}$ provided us with important information on the crystal and magnetic structure, which contributes to the understanding of the dramatic impact of hydrogenation on the magnetism of U_2T_2X compounds. The position of H(D) atoms within the U_3Ni tetrahedra suggests that besides the moderate lattice expansion, also the variations of the 5*f* hybridisation with nickel 3*d* states can be responsible for the dramatic increase of T_N. Based on the available crystallographic data for other U_2T_2X hydrides (*i.e.* the tendencies of lattice expansion), we believe that these structure data are valid for other hydrides of the series as well.

Hydrogenation (deuteration) of U_2Ni_2Sn leads to the reorientation of magnetic moments of uranium. Since in U_2Ni_2Sn the shortest inter-uranium distances are easily found in the basal plane, the uranium moments are directed perpendicularly, i.e. along the *c*-direction. The anisotropic expansion due to hydrogenation has a larger effect on the inter-uranium distances in the basal plane and these distances approach the U-U distances along the *c*-direction. As there is no geometrical preference on the type of anisotropy, the moments directions are likely to be determined by the anisotropy of exchange interactions.

5.2.4. $U_2Co_2InH_{1.9}$ and $U_2Fe_2SnH_{1.7}$ Hydrides

U_2Co_2In and U_2Fe_2Sn intermetallic compounds were used as starting materials for hydrogenation. Hydrogenation of both compounds was performed at hydrogen pressure 110 bar and applying thermal treatment up to $T = 923$ K. Hydrogen content was determined by decomposition in closed volume and it reached 1.9 H atoms/formula unit for U_2Co_2In and 1.7 H atoms/formula unit for U_2Fe_2Sn. For both compounds the decomposition curves look similar to those observed for other hydrides of U_2T_2X compounds. Decomposition takes place in one step starting at approximately 420 K and completes up to $T = 600$ K.

The phase composition on the samples before and after hydrogenation was studied by X-ray powder diffraction. Initial U_2Co_2In sample contained small amount (≈6%) of In-metal as a spurious phase, which was given in excess in order to avoid the non-stoichiometric composition due to the evaporation of indium. Hydrogenated sample contained U_2Co_2In hydride and non-modified In metal. The crystal structure parameters are given in Table 5.13. The X-ray powder pattern of U_2Fe_2Sn proved that the synthesis of this compound is more difficult comparing to other studied U_2T_2X compounds, what has been reported already before [97, 98]. The authors of

Ref. 97 demonstrated that certain homogeneity range for U_2Fe_2Sn exists and they could not avoid the formation of small amount of ferromagnetic U_5Sn_4 as a spurious phase. The most apparent reason is that U_2Fe_2Sn is not formed from the melt and therefore arc-melting is not the most suitable method for the synthesis. The X-ray powder diffraction pattern exhibits some additional peaks, which could be attributed to UO_2 and another unidentified phase. The lattice parameters of U_2Fe_2Sn agree well with the reported values [98]. The structure parameters for both U_2Fe_2Sn and $U_2Fe_2SnH_{1.7}$ are given in Table 5.13.

Table 5.13. Structure and magnetic parameters of U_2Co_2In, U_2Fe_2Sn and respective hydrides. Lattice parameters *a* and *c*, unit cell volume *V*, relative lattice expansion along a direction $\Delta a/a$, along *c* direction $\Delta c/c$ and relative volume expansion $\Delta V/V$ are given. $d_{U\text{-}U} \parallel c$ and $d_{U\text{-}U} \perp c$ are the nearest-neighbour U-U distances along the *c*-axis and perpendicular to it, respectively. For all compounds the shortest interuranium distnce is equal to the lattice parameter *c*.

	U_2Co_2In	$U_2Co_2InH_{1.9}$	U_2Fe_2Sn	$U_2Fe_2SnH_{1.7}$
a (pm)	736.5(1)	759.0(2)	729.7(3)	752.5(3)
c (pm)	343.4(1)	350.7(1)	344.6(1)	354.9(2)
V (10^8 pm^3)	1.863(1)	2.020(1)	1.835(1)	2.009(1)
$\Delta a/a$ (%)	-	3.1	-	3.1
$\Delta c/c$ (%)	-	2.2	-	3.0
$\Delta V/V$ (%)	-	8.4	-	9.5
x_U	0.169(1)	0.175(1)	0.170(1)	0.177(1)
x_{Ni}	0.377(3)	0.376(2)	0.373(5)	0.373(5)
$d_{U\text{-}U} \perp c$ (pm)	352.1(10)	375.7(11)	350.9(10)	376.7(11)
$d_{U\text{-}U} \parallel c$ (pm)	343.4(1)	350.7(1)	344.6(1)	354.9(1)

For U_2Co_2In the lattice expansion upon hydrogenation is anisotropic with dominating basal plane component, unlike for U_2Ni_2In in which the lattice expansion along the *c*-axis dominates. Relative lattice expansion of 8.4% is higher than the value observed for U_2Ni_2In (6.8%) what resembles much the tendency observed U_2Co_2Sn and U_2Ni_2Sn hydrides – *i.e.* that the hydrogenation leads to a larger volume effect for the Co compound, which is characterized by a stronger 5*f*-3*d* hybridisation. U_2Fe_2Sn exhibits the largest volume expansion out of the studied U_2T_2X hydrides. It reaches 9.5% and is nearly isotropic with very slight predomination in the basal plane component. For both hydrides of U_2Co_2In and U_2Fe_2Sn, the shortest inter-uranium distances vary within the Hill limit, but as it has been shown on the example of U_2Co_2Sn, a dramatic effect on magnetism can be expected due to hydrogenation.

Magnetic studies of U_2Co_2In, U_2Fe_2Sn and respective hydrides were performed using the PPMS system in the temperature range 1.8-300 K and in magnetic fields up to 9 T. U_2Co_2In exhibits no magnetic order and the susceptibility curve is almost temperature independent yielding the value $\chi \approx 3 \cdot 10^{-8}$ m^3/mol (Fig. 5.37). Hydrogenation has a dramatic impact on the magnetism of U_2Co_2In and leads to the enhancement of magnetic interactions in the hydride. After performing the correction procedure to eliminate the contribution of ferromagnetic UH_3, which was found as a spurious phase, we can describe the behaviour of $U_2Co_2InH_{1.9}$ by modified Curie-Weiss fit with the parameters $\mu_{eff} = 1.6\ \mu_B$/U, $\theta_P = 3$ K, $\chi_0 = 4.4 \cdot 10^{-8}$ m^3/mol. The positive value of θ_P suggests that some ferromagnetic interactions are present in this compound. Detailed analysis of the low-temperature part showed the presence of maximum on the susceptibility curve at $T = 2.4$ K. It could be attributed either to the antiferromagnetic order or to the spin-fluctuation behaviour. Magnetization curve, measured at $T = 2$ K, showed the shape typical for antiferromagnet with metamagnetic transition at 2 T (Fig. 5.38). This value is close to the value observed for β-$U_2Co_2SnH_{1.4}$. The remanent magnetization observed can be attributed to the presence of ferromagnetic UH_3 and to the structure defects leading to the uncompensated spins on the grain boundaries. The studies of the magnetization curves at different temperatures showed that the metamagnetic transition is shifted to the higher fields with the temperature increase (Fig. 5.39). The value of the

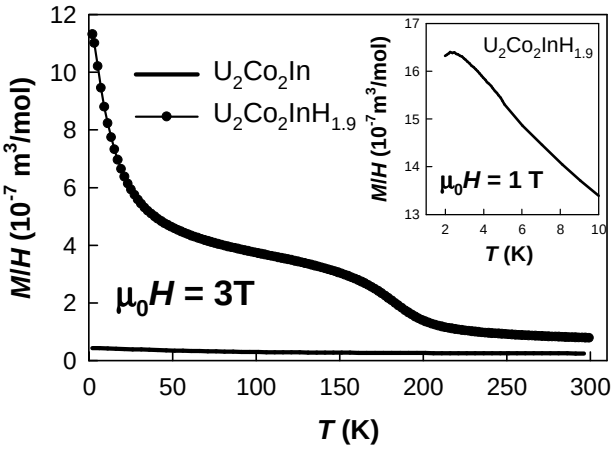

Fig. 5.37. Temperature dependences of the magnetic susceptibility of U_2Co_2In and $U_2Co_2InH_{1.9}$ measured in the magnetic field $\mu_0 H = 3$ T. The anomaly at $T = 180$ K can be attributed to a small amount of UH_3. The inset shows the low-temperature measurements in the magnetic field $\mu_0 H = 1$ T.

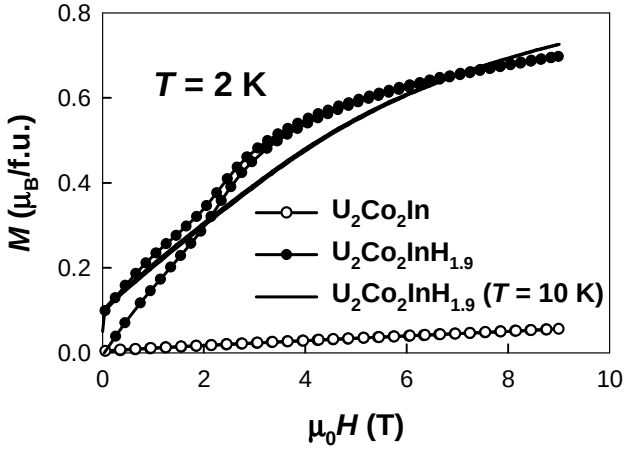

Fig. 5.38. Magnetization curves of U_2Co_2In and $U_2Co_2InH_{1.9}$ measured at $T = 2$ K. The solid line shows magnetization curve of $U_2Co_2InH_{1.9}$ measured at $T = 10$ K.

metamagnetic field was determined by the maximum of the first derivative dM/dH. However, the temperature dependence of the metamagnetic field does not show the typical behaviour for spin-fluctuator, i.e. the square dependence of the critical field versus temperature. Therefore we tend to assume that $U_2Co_2InH_{1.9}$ is an antiferromagnet (T_N = 2.4 K) similar to other magnetically ordered U_2T_2X compounds. The increase of the metamagnetic field with the temperature increase may indicate on the complicated character of the magnetic phase diagram with several magnetically ordered phases.

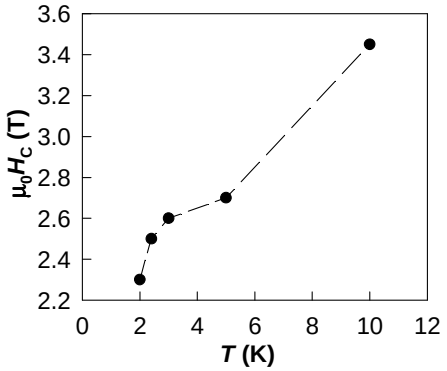

Fig. 5.39. Temperature dependence of critical metamagnetic field for $U_2Co_2InH_{1.9}$.

Magnetic properties of $U_2Fe_2SnH_{1.7}$ remain the least clear case among all studied. The susceptibility of U_2Fe_2Sn shows that the sample is strongly inhomogeneous with at least two spurious ferromagnetic phases (Fig. 5.40). The transition at approximately T = 150 K can be attributed to UFe_2, for which the Curie temperatures between 147 K and 162 K were reported depending on the composition [99], and another small anomaly at about 60 K can be attributed to U_5Sn_4 with $T_C \approx 64$ K, which has been already reported to coexist with U_2Fe_2Sn [97]. The character of the susceptibility for $U_2Fe_2SnH_{1.7}$ is even more complicating. Although showing the enhancement of the magnetic interactions, no clear magnetic transition could be distinguished. Moreover, no tendency for saturation at lower temperatures was observed either. This might indicate at highly inhomogeneous sample. The magnetization curve exhibits stronger field dependence comparing

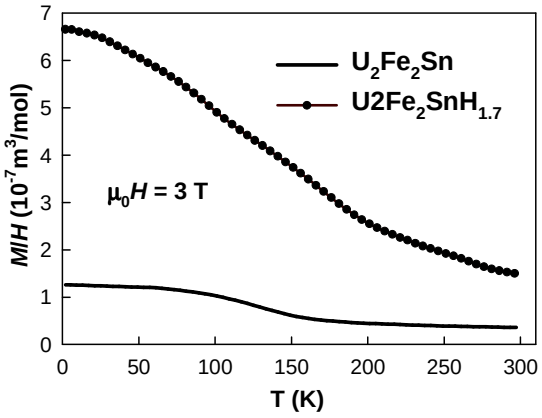

Fig. 5.40. Magnetic susceptibility curves of U_2Fe_2Sn and $U_2Fe_2SnH_{1.7}$ measured in the magnetic field μ_0H = 3 T.

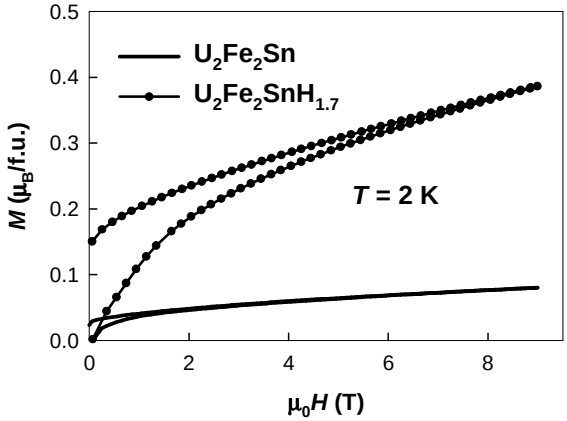

Fig. 5.41. Magnetization curves of U_2Fe_2Sn and $U_2Fe_2SnH_{1.7}$ measured at T = 2 K.

to the initial compound with increased value of the remanent magnetization, which we tent to assume to be an intrinsic feature (Fig. 5.41). However, we can't be really conclusive, therefore, the only message from the magnetic studies of $U_2Fe_2SnH_{1.7}$ is that hydrogenation leads to the enhancement of magnetic interactions in this case too.

To conclude, we showed that two non-magnetic compounds, U_2Co_2In and U_2Fe_2Sn, turned out to be very sensitive to hydrogenation. In both cases hydrogenation led to pronounced enhancement of magnetic interactions. The Néel temperature for $U_2Co_2InH_{1.9}$ is very low comparing to other U_2T_2X compounds and their hydrides. No information on the peculiarities of the onset of magnetic order in $U_2Fe_2SnH_{1.7}$ is available. But nonetheless, the studies of U_2Co_2In and U_2Fe_2Sn fit well to the picture of 5*f*-*d* hybridisation-mediated magnetic properties of U_2T_2X compounds.

5.2.5. Hydrogenation of U_2Pd_2In

Hydrogenation of U_2Pd_2In stands apart from other hydrogen-absorbing U_2T_2X compounds. The intermetallic U_2Pd_2In compound was used for the hydrogenation. The hydrogenation was performed at hydrogen pressure 110 bar and at temperature T = 923 K. The initial sample and the products of the reaction were studied by X-ray powder diffraction analysis. The amount of hydrogen absorbed was determined by decomposition in the closed volume. Hydrogen absorption leads to the decomposition of part of the U_2Pd_2In sample according to the reaction in several steps starting at T = 473 K:

$$2U_2Pd_2In + 3H_2 \rightarrow 2UH_3 + 2UPd_2In$$

Decomposition studies revealed that decomposition took place in several stages and finally pointed to the amount of 1.2 H atoms absorbed per formula unit of U_2Pd_2In. Taking it into account together with the quantitative X-ray phase analysis of the products of hydrogenation, we concluded that ≈40% of U_2Pd_2In are decomposed while the rest of the sample did not interact with hydrogen. Surprisingly, after decomposition the initial U_2Pd_2In phase is fully recovered. The phenomenon, which we observed, is called hydrogenation-decomposition-desorption-recombination (HDDR) process. This process was especially widely studied on ferromagnetic Nd-Fe-B alloys [100] due to its commercial application.

Although we can not foresee any practical application of HDDR process for U_2Pd_2In, an important message is that for U_2T_2X compounds, similar to U*TX* compounds, hydrogen absorption area is not restricted only to 3*d* metals, but it comprises the upper right corner of the transition metal section of the periodic table, including Pd – a heavy 4*d* metal.

6. Conclusions

The studies of two groups of compounds prove that the magnetic properties of uranium intermetallics are very sensitive to the hydrogen absorption. Several general tendencies can be observed based on the data available. The systematics of the occurrence of hydrides of uranium ternary intermetallics containing transition metal is in all cases more or less restricted to the upper right corner of the transition-metal series of the periodic table. This is also the area where a magnetic order can appear, due to the weaker 5*f*-ligand hybridisation. In all compounds studied, hydrogen absorption leads, with one exception, to stronger magnetic interactions.

These tendencies are clearly manifest also for the U_2T_2X-H systems, the largest group in which the hydrogenation was so far successful (see Fig. 6.1). The hydrides are formed for all the compounds of 3*d* transition metals and hydrogen absorption was registered for one compounds with Pd (although the hydride was not synthesized, the affinity to hydrogen was demonstrated). Meanwhile, none of the investigated compounds with the transition metal from the lower right part of the transition metal series was found to absorb hydrogen. The variations of magnetism of U_2T_2X compounds upon hydrogenation are really strong. For example, the Néel temperatures of $U_2Ni_2SnH_{1.8}$ and $U_2Ni_2InH_{1.9}$ considerably exceed those of all known U_2T_2Sn and U_2T_2In compounds. Moreover, two non-magnetic compounds U_2Co_2In and U_2Co_2Sn, exhibit magnetic

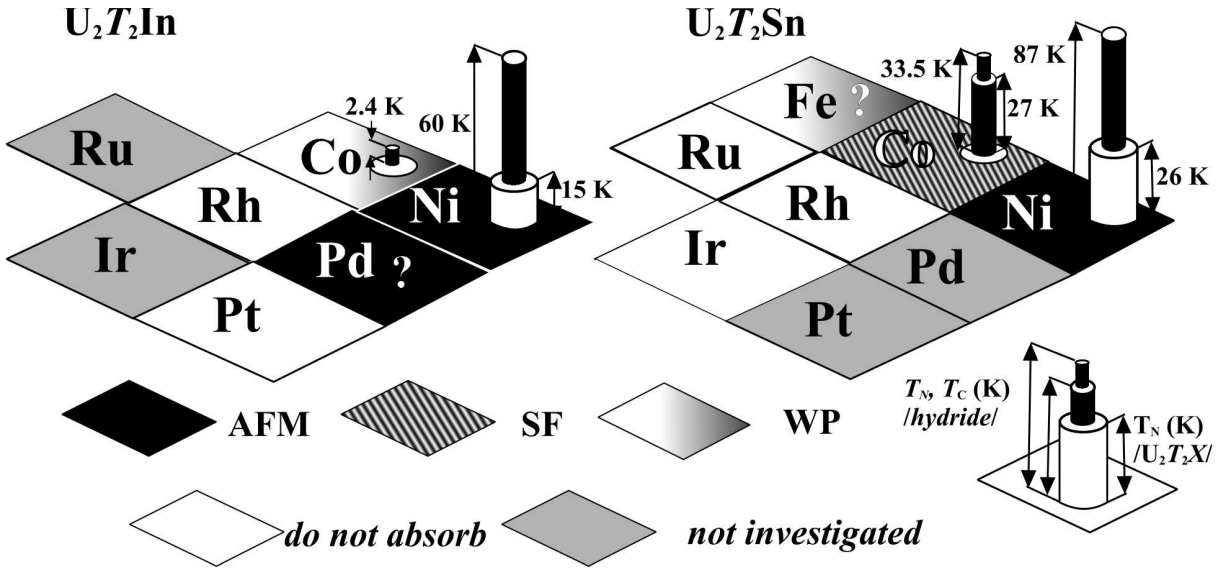

Fig 6.1. Review of the results of hydrogenation of U_2T_2X compounds. The type of ground state of the initial compounds is indicated: AFM - antiferromagnetic, SF - spin fluctuator, WP - weak paramagnet. T_N, T_C - magnetic ordering temperature. White rods show the ordering temperature of the compounds before hydrogenation, black rods - the ordering temperature of the corresponding hydrides.

order after hydrogenation. In general it can be attributed to enhanced U-U spacing, reducing the 5*f*-5*f* overlap. But more quantitative considerations (e.g. the pressure variations of magnetic ordering temperatures in U*T*Si hydrides) suggest that reducing the 5*f*-*d* hybridization, withdrawing partly the *d*-states due to the *d*-1*s* bonding, can play also a significant role.

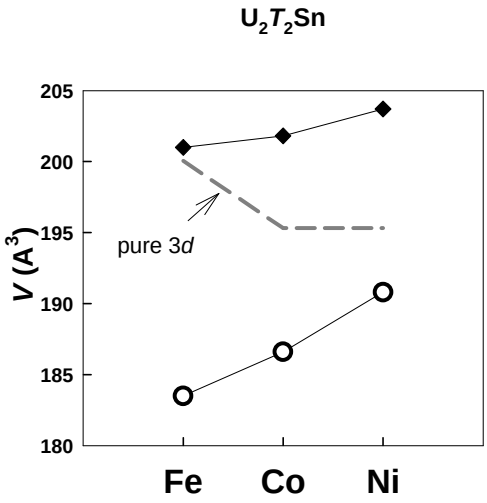

Fig. 6.2. The dependence of the unit cell volume of the U_2T_2Sn (empty circles) and U_2T_2Sn hydrides (filled squares) on the nature of transition metal. The atomic radii of the transition metals are shown by dashed line in relative scale.

The proof for our conjecture can be easily obtained from the analysis of the lattice parameters of U_2T_2Sn hydrides (Fig. 6.2). Although atomic volume of decreases in the raw Fe–Co–Ni, the unit cell volume increases in the raw U_2Fe_2Sn–U_2Co_2Sn–U_2Ni_2Sn. Consequently the effective atomic radius of the transition metal increases in the raw Fe–Co–Ni. The explanation is the 5*f*-3*d* hybridization which is the most pronounced for Fe, then Co and then Ni. The unit cell volume also increases in the sequence $U_2Fe_2SnH_{1.7}$ – $U_2Co_2SnH_{1.4}$ – $U_2Ni_2SnH_{1.8}$. However, the dependence is less steep comparing to the non-hydrogenated compounds and relative volume expansion decreases from Fe to Ni. If we assume that the lattice expansion due to the presence of hydrogen should be the same for all three compounds, since the stoichiometry is close for all of them, we might conclude that the additional volume increase upon hydrogenation is observed for compounds in which the 5*f*-*d* hybridisation is stronger. Such mechanism could be effective especially if the hydrogen sites are primarily surrounded by transition metal atoms. This was the case proved by neutron diffraction studies on $U_2Ni_2SnH_{1.8}$.

For orthorhombic U*TX* compounds two above-mentioned tendencies are observed, as well. The hydrogen absorption area of the transition metal series can be limited to the triangle Co–Ni–Pd. UCoSi is a non-magnetic compound and hydrogen absorption although leads to the enhancement of magnetic interactions, but it is not sufficient enough to induce magnetic order.

On the example of the group of the hexagonal U*T*Sn compounds we demonstrated how diverse may the influence of hydrogen be. The behaviour of UCoSn fits well to the picture described above. Firstly, in all the investigated groups the compounds with Co were good candidates for the formation of hydrides. Secondly, the enhancement of magnetic interactions agrees well with the behaviour of other uranium intermetallics upon hydrogenation. On the other

hand – URuSn is the only exception from all the stated rules. The nature of the transition metal did not predefine the hydrogen absorption ability for the compound and the synthesized hydride did not display the typical behaviour upon hydrogenation.

As a main conclusion, we have demonstrated that the hydrogen absorption can be used as a control parameter to tune magnetic properties of uranium ternary intermetallics. Cases can be found in which the hydrogenation drives a system over an onset of magnetic ordering. As complex many-body phenomena occur in this regime, conceived as a quantum critical point, and therefore very fine modifications can result in tremendous effects.

References

[1] Hubbard J, *Proc. R. Soc. A* 276 (1963) 238.

[2] Stoner E.C., *Proc. R. Soc. A* 154 (1936) 656.

[3] Stoner E.C., *Proc. R. Soc. A* 165 (1938) 372.

[4] Mohn P, Magnetism in the Solid State. An Introduction, Spinger, Berlin, 2003.

[5] K. K. Murata and Doniach S., *Phys. Rev. Letters* 29 (1972) 285.

[6] Moriya T., Spin Fluctuations in Itinerant Electron Magnetism, Springer, Berlin, 1985.

[7] Cooper B.R., Sieman R. Yang D. Thayamballi P. Banerjea A., *in: Handbook on the Physics and Chemistry of the Actinides*, ed. by A.A. Freeman and G.H. Lander, vol. 2, Elsevier, Amsterdam (1985) pp. 435-500.

[8] Fukai Y., The Metal-Hydrogen Systems. Basic Bulk Properties, Springer-Verlag, Berlin, 1993

[9] Binary Alloys Phase Diagrams, Ed. by Massalski T.B., Okamoto H., Subramanian P.R.; Kacprzak L., American Society for Metals, Materials Park, 1996.

[10] Hydrogen in Metals II. Application-Oriented Properties, Ed. by G. Alefeld and J. Volkl, Vol. 29, Springer-Verlag, Berlin, 1978

[11] Oats W.A. and Stoneham A.M., *J. Phys. F* 13 (1983) 2427.

[12] Switendick A.C., *Z. Phys. Chem. N. F.* 117 (1979) 89.

[13] Westlake D.G., *J. Less-Common Met.* 75 (1980) 177.

[14] Westlake D.G., *J. Less-Common Met.* 90 (1983) 251.

[15] Westlake D.G., *J. Less-Common Met.* 91 (1983) 1.

[16] Westlake D.G., *J. Less-Common Met.* 91 (1983) 275.

[17] Lundin C.E., Lynch F.E. and Magee C.B., *J. Less-Common Met.* 56 (1977) 19.

[18] Hjörvarsson B., Guo J.-H., Ahuja R., Ward R.C.C., Andersson G., Ericsson O., Wells M.R., Sathe C., Agui A., Butorin S.M. and Nordgren J., *J. Phys.: Condens. Mater* 11 (1999) L119.

[19] Shoemaker D.P. and Shoemaker C.B., *J. Less-Common Met.* 68 (1979) 43.

[20] Wang X.W. and Chen C.F., *Phys. Rev. B* 56 (1997) R7049.

[21] Feenstra R, de Groot D.G., Griessen R., Burger J.P. and Menovski A., *J. Less-Common Met.* 130 (1987) 375.

[22] Jacob I., Beeri O. and Elish E., *J. Alloys Compds.* 221 (1995) 129.

[23] Switendick A.C., *J. Less-Common Met.* 74 (1980) 199.

[24] Wiesinger G. and Hilscher G., *in: Handbook of Magnetic Materials*, ed. by K.H.J. Buschow, Elsevier, Amsterdam (1991) pp. 511-584.

[25] Chevalier B., Kahn M.L., Bobet J.-L., Pasturel M. and Etourneau J., *J. Phys.: Condens. Mater* 14 (2002) L365-L368.

[26] Chevalier B., Bobet J.-L., Pasturel M., Bauer E., Weill F., Decourt R. and Etourneau J., *Chem. Mater.* 15 (2003) 2181.

[27] Mulford R.N.R., Ellinger F.H. and Zachariasen W.H., *J. Am. Chem. Soc.* 76 (1954) 297.

[28] Rundle R.E., *J. Am. Chem. Soc.* 69 (1947) 1719.

[29] Rundle R.E., *J. Am. Chem. Soc.* 73 (1951) 4172.

[30] Ward J.W., *Physica B* 130 (1985) 510.

[31] Switendick A.C., *J. Less-Common Met.* 88 (1982) 257.

[32] Gouder T., Eloirdi R., Wasten F., Colineau E., Rebizant J. and Kolberg D., Huber F., *Phys. Rev. B* 70 (2004) 235108.

[33] Fernandes J.C., Continentino M.A. and Guimaraes A.P., *Solid State Commun.* 55 (1985) 1011.

[34] Dwight A.E., *in: Development in the Structural Chemistry of Alloy Phases*, ed. by B.C. Giessen, Plenum, New York, 1969.

[35] Andreev A.V. and Bartashevich M.I., *Phys. Met. Mettalogr.* 62 (1986) 50.

[36] Sechovsky V, Havela L., Hilscher G., Pillmayr N., Andreev A.V., Veenhuizen P.A. and de Boer F.R., *J. Appl. Phys.* 63 (1988) 3070.

[37] Tran V.H. and Troc R., *J. Magn. Magn. Mater.* 102 (1991) 74.

[38] Tran V.H., Troc R. and Badurski D., *J. Alloys Compds.* 219 (1995) 285.

[39] Andreev A.V., *Phys. Met. Mettalogr.* 60 (1985) 193.

[40] Kruk R., Kmiec R., Latka K., Tomala K., Troc R. and Tran V.H., *Phys. Rev. B* 55 (1997) 5851.

[41] Sechovsky V, Havela L., Neuzil L., Andreev A.V., Hilscher G. and Schmitzer C., *J. Less-Common Met.* 121 (1986) 169.

[42] Sechovsky V, Havela L., Nozar P., Bruck E., de Boer F.R., Menovsky A., Buschow K.H.J. and Andreev A.V., *Physica B* 163 (1990) 103.

[43] Krylov V.I., Andreev A.V., Sechovsky V and Havela L., *Hyperfine Interact.* 59 (1990) 391.

[44] Andreev A.V., Aruga Katori H., Goto T., Sechovsky V and Havela L., *J. Magn. Magn. Mater.* 140-144 (1995) 1383.

[45] Brück E., Hybridization in cerium and uranium intermetallic compounds, PhD thesis, University of Amsterdam, 1991.

[46] Canepa F., Manfrinetti P., Pani M. and Palenzona A., *J. Alloys Compds.* 234 (1996) 225.

[47] Lloret B., Chevalier B., Gravereau P., Darriet B. and Etourneau J., *J. Phys. (Paris)* 49 (1988) 487.

[48] Prokeš K., Buschow K.H.J., Brück E., de Boer F.R., Svoboda P. and Sechovsky V, *Physica B* 230-232 (1997) 39.

[49] Troc R. and Tran V.H., *J. Magn. Magn. Mater.* 73 (1988) 389.

[50] de Boer F.R., Bruck E., Sechovsky V, Havela L. and Buschow K.H.J., *Physica B* 163 (1990) 175.

[51] Peron M.N., Kergadallan Y., Rebizant J., Meyer D., Winand J.M., Zwirner S., Havela L., Nakotte H., Spirlet J.C., Kalvius G.M., Colineau E., Oddou J.L., Jeandcy C. and Sanchez J.P., *J. Alloys Compds.* 201 (1993) 203.

[52] Nowak B., Zogal O.J., Niedzwiedz K., Troc R., Wochowski K. and Zolnierek Z., *Physica B* 192 (1993) 213.

[53] Havela L., Sechovsky V, Svoboda P., Nakotte H., Prokeš K., de Boer F.R., Seret A., Winand J.M., Rebizant J., Spirlet J.C., Purwanto A. and Robinson R.A., *J. Magn. Magn. Mater.* 140-144 (1995) 1367.

[54] Bourée F., Chevalier B., Fournès L., Mirambet F., Roisnel T., Tran V.H. and Zolnierek Z., *J. Magn. Magn. Mater.* 138 (1994) 307.

[55] Kindo K., Fukushima T., Kumada T., de Boer F.R., Nakotte H., Prokeš K., Havela L., Sechovsky V, Seret A., Winand J.M., Spirlet J.C. and Rebizant J., *J. Magn. Magn. Mater.* 140-144 (1995) 1369.

[56] Wastin F., Spirlet J.C. and Rebizant J., *J. Alloys Compds.* 219 (1995) 232.

[57] Havela L., Sechovsky V, Svoboda P., Divis M., Nakotte H., Prokeš K., de Boer F.R., Purwanto A., Robinson R.A., Seret A., Winand J.M., Rebizant J., Spirlet J.C., Richter M. and Eschrig H., *J. Appl. Phys.* 76 (1994) 6214.

[58] Nakotte H., Purwanto A., Robinson R.A., Prokeš K., Klaasse J.C.P., de Chatel P.F., de Boer F.R., Havela L., Sechovsky V, Pereira L.C.J., Seret A., Rebizant J., Spirlet J.C. and Trouw F., *Phys. Rev. B* 53 (1996) 3263.

[59] Mirambet F., Gravereau P., Chevalier B., Trut L. and Etourneau J., *J. Alloys Compds.* 191 (1993) L1-L3.

[60] Purwanto A., Robinson R.A., Havela L., Sechovsky V, Svoboda P., Nakotte H., Prokeš K., de Boer F.R., Seret A., Winand J.M., Rebizant J. and Spirlet J.C., *Phys. Rev. B* 50 (1994) 6792.

[61] Sechovsky V and Havela L., in: *Handbook of Magnetic Materials*, ed. by K.H.J. Buschow, Elsevier, Amsterdam (1998) pp. 1-290.

[62] de Boer F.R., Kindo K., Nakotte H., Prokeš K. and Sechovsky V, *Physica B* 246-247 (1998) 129.

[63] Tran V.H., Zolnierek Z., Bourée F. and Roisnel T., *J. Magn. Magn. Mater.* 161 (1996) 270.

[64] Nakotte H. Magnetism of cerium and uranium intermetallics, PhD Thesis, University of Amsterdam, 1994.

[65] Pinto R.P., Amado M.M., Salgueiro M.A., Braga M.E., Sousa J.B., Chevalier B., Mirambet F. and Etourneau J., *J. Magn. Magn. Mater.* 140-144 (1995) 1371.

[66] Kim J.S., Alwood J., Getty S.A., Sharifi F. and Stewart G.R., *Phys. Rev. B* 62 (2000) 6986.

[67] du Plessis P.de V., Strydom A.M. and Baran A., *Physica B* 206-207 (1995) 495.

[68] Prokeš K., Nakotte H., Havela L., Sechovsky V, Pereira L.C.J., Rijkeboer C., Seret A., Spirlet J.C., Svoboda P. and de Boer F.R., *Physica B* 223-224 (1996) 225.

[69] Bordallo H.N., Nakotte H., Kolomiets A.V., Christianson A., Havela L., Schultz A.J., Drulis H. and Iwasieczko W., *Physica B* 276-278 (2000) 706.

[70] Kolomiets A.V., Havela L., Rafaja D., Bordallo H.N., Nakotte H., Yartys V.A., Hauback B.C., Drulis H., Iwasieczko W. and DeLong L.E., *J. Appl. Phys.* 87 (2000) 6815.

[71] Raj P., Shashikala K., Sathyamoorthy A., Malik S.K. and Yelon W.B., *J. Appl. Phys.* 89 (2001) 7192.

[72] Yamamoto T. and Kayano H., *J. Alloys Compds.* 213-214 (1994) 533.

[73] Zogal O.J., Lam D.J., Zygmunt A., Drulis H., Petrynski W. and Stalinski S., *Phys. Rev. B* 29 (1984) 4837.

[74] Raj P., Shashikala K., Sathyamoorthy A., Harish Kumar N., Venkateswara Rao C.R. and Malik S.K., *Phys. Rev. B* 63 (2001) 094414.

[75] Yamamoto T., Ishii Y. and Kayano H., *J. Alloys Compds.* 269 (1998) 162.

[76] Raj P., Sathyamoorthy A., Shashikala K., Harish Kumar N., Venkateswara Rao C.R. and Malik S.K., *J. Alloys Compds.* 296 (2000) 20.

[77] Raj P., Shashikala K., Sathyamoorthy A., Harish Kumar N., Venkateswara Rao C.R. and Malik S.K., *Physica B* 312-313 (2002) 885.

[78] Kolomiets A.V., Havela L., Andreev A.V., Wastin F., Sebek J. and Marysko M., *Phys. Rev. B* 66 (2002) 144423.

[79] Kolomiets A.V., Havela L., Andreev A.V., Miliyanchuk K., Heathman S. and Goto T., *J. Magn. Magn. Mater.* 272-276 (2004) e343.

[80] Kolomiets A.V., Magnetism of f-electron compounds and their hydrides, PhD Thesis, Charles University, Prague, 2000.

[81] Asada K., Ono K., Yamaguchi K., Yamamoto T., Maekawa A., Oe S. and Yamawaki M., *J. Alloys Compds.* 231 (1995) 780.

[82] Kraus W. and Nolze G., Powder Cell for Windows, Berlin, 2000.

[83] Rietveld H.M., *J. Appl. Cryst.* 2 (1969) 65.

[84] Rodrigues-Carvajal J., FullProf Suite, LLB (CEA-CNRS), 2001.

[85] Rodrigues-Carvajal J., *Abstracts of the Satellite Meeting on Powder Diffraction of the XV Congress of IUCr*, Toulouse, France (1990) 127.

[86] Giacovazzo C., Monaco H.L., Artioli G., Viterbo D., Ferraris G., Gilli G., Zanotti G., and Catti M., Fundamentals of Crystollagraphy, Oxford University Press, Oxford, 2002

[87] Tawnawski Z., Kolwicz-Chodak L., Figiel H., Budziak A., Havela L., Vejpravova J., Kolomiets A., Sechovsky V. and Kim-Ngan N.-T.H., *Physica B* 355 (2005) 202.

[88] Waerenborgh J.C., Figueiredo M.O., Cabral J.M.P. and Pereira L.C.J., *J. Solid State Chem.* 111(2) (1994) 300.

[89] Ruebenbauer K. and Birchall T., *Hyperfine Interac.* 7 (1979) 125.

[90] Havela L., Neuzil L., Sechovsky V, Andreev A.V., Schmitzer C. and Hilscher G., *J. Magn. Magn. Mater.* 54-57 (1986) 551.

[91] Yartys V.A., Denys R.V., Hauback B.C., Fjellvag H., Bulyk I.I., Riabov A.B. and Kalychak Ya.M., *J. Alloys Compds.* 330-332 (2002) 132.

[92] Brinks H.W., Yartys V.A. and Hauback B.C., *J. Alloys Compds.* 332 (2001) 160.

[93] Yartys V.A., Olavesen T., Hauback B.C., Fjellvag H. and Brinks H.W., *J. Alloys Compds.* 330-332 (2002) 141.

[94] Raj P., Sathyamoorthy A., Shashikala K., Venkateswara Rao C.R. and Malik S.K., *Solid State Commun.* 120 (2001) 375.

[95] Malik S.K., Raj P., Sathyamoorthy A., Shashikala K., Harish Kumar N. and Menon L., *Phys. Rev. B* 63 (2001) 172418.

[96] Mishra S.G. and Ramakrishnan T.V., *Phys. Rev. B* 18 (1978) 2308.

[97] Gonçalves A.P., Noël H. and Waerenborgh J.C., *J. Magn. Magn. Mater.* 251 (2002) 1.

[98] Noël H. and Gonçalves A.P., *Intermetallics* 9 (2001) 473.

[99] Aldred A.T., *J. Magn. Magn. Mater.* 10 (1979) 42.

[100] Takeshita T., *J. Alloys Compds.* 231 (1995) 51.

Appendix A

X-ray powder patterns of UCoSn and $UCoSnH_{1.4}$ (Co-*K*α radiation). Observed pattern is represented by crosses, calculated – by solid line, the difference between the observed and calculated patterns is shown. R_B = 11.8% for UCoSn, R_B= 10.9% for $UCoSnH_{1.4}$.

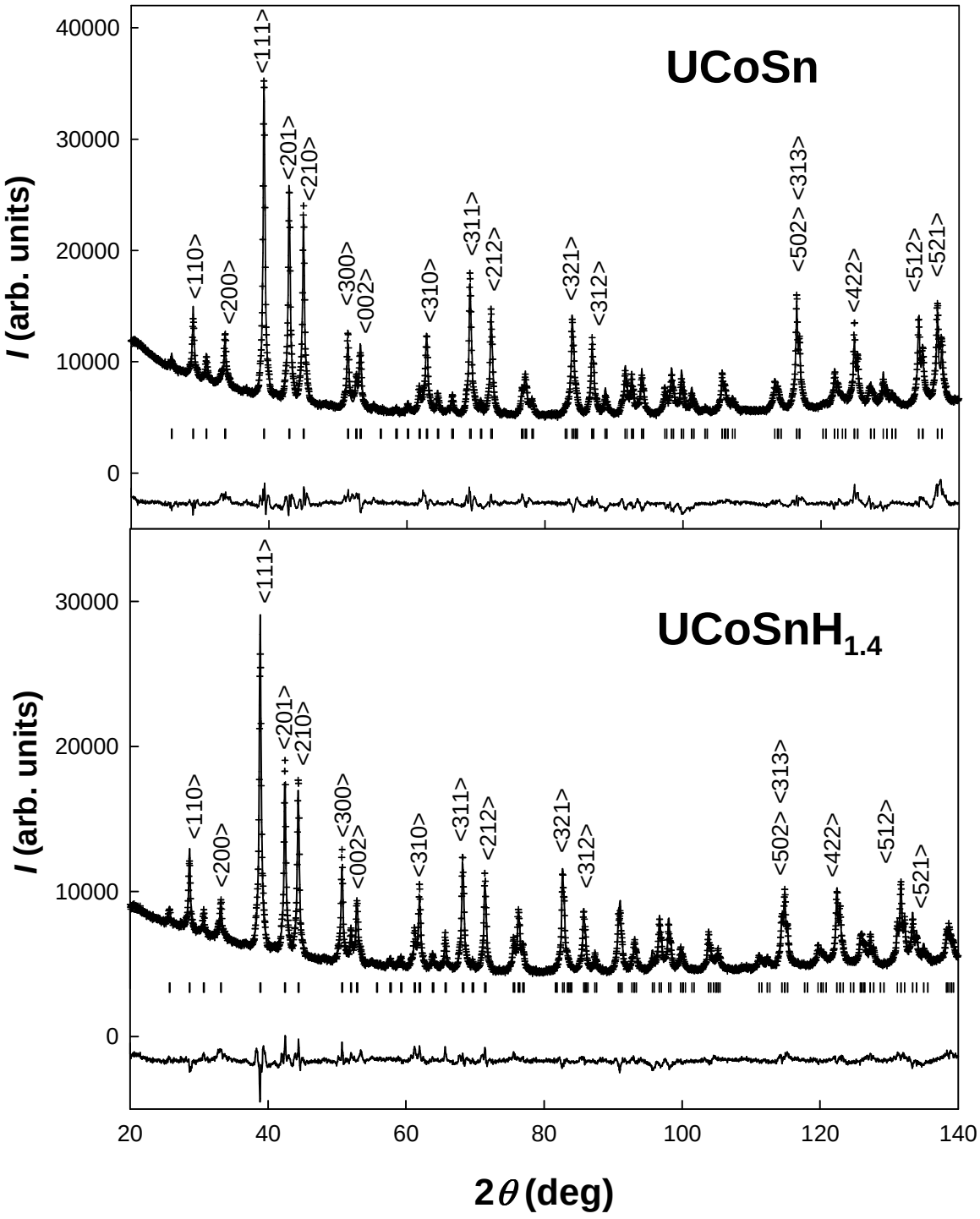

Appendix B

X-ray powder patterns of URuSn and $URuSnH_{1.4}$ (Co-*K*α radiation). Observed pattern is represented by crosses, calculated – by solid line, the difference between the observed and calculated patterns is shown. R_B = 15.4% for URuSn, R_B= 14.9% for $URuSnH_{1.4}$.

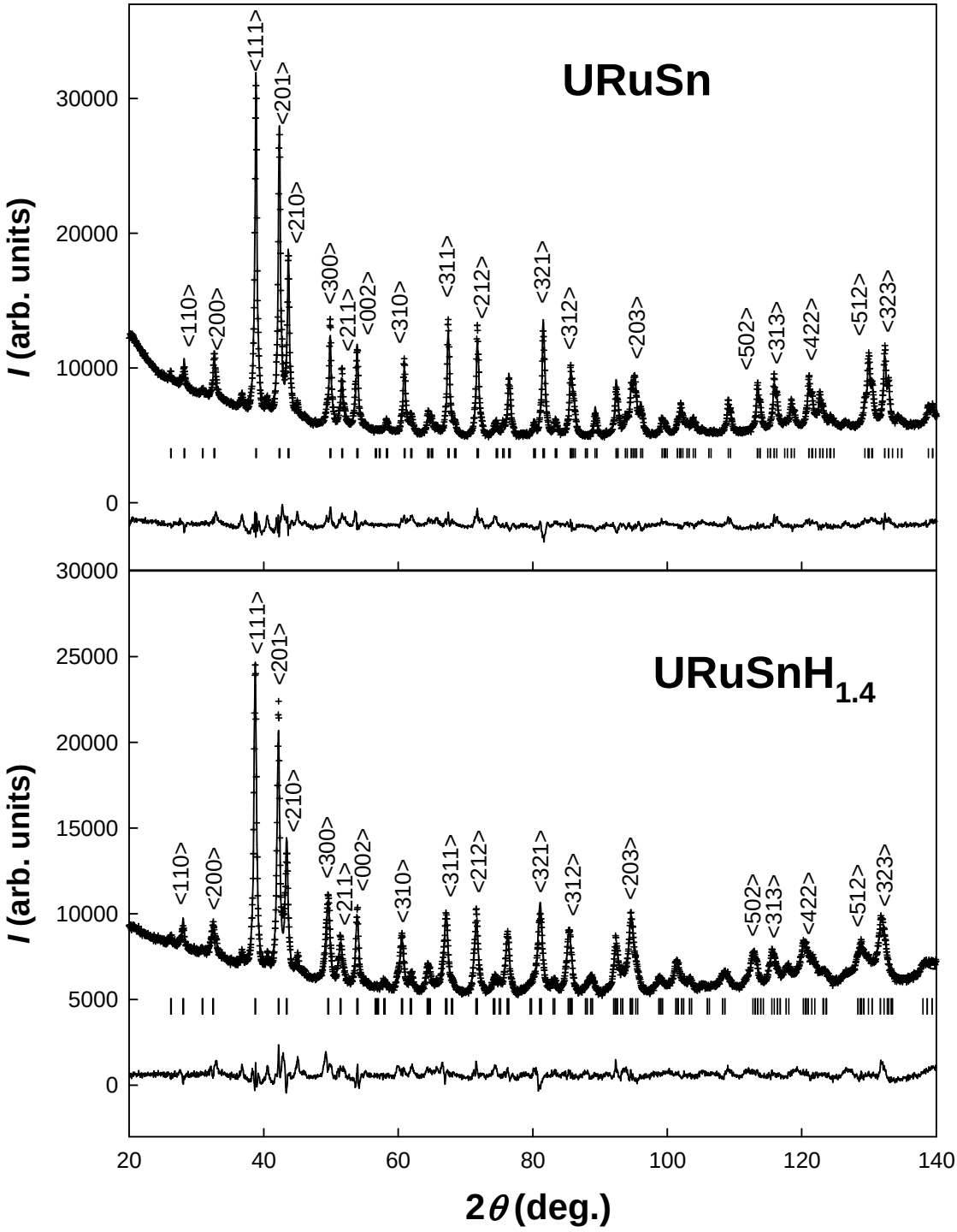

Appendix C

Table of interatomic distances below 500 pm for $UCoSnD_{0.6}$ compound

Atom 1	Atom 2	Distance (pm)	Coordination Number
U	D	221(1)	2x
	D	221(1)	2x
	Co1	292(1)	1x
	Co2	298(1)	4x
	Sn	316(1)	2x
	Sn	325(1)	4x
	U	381(1)	4x
	U	402(1)	2x
	Co1	431(1)	1x
	D	439(3)	2x
	D	439(3)	2x
	D	478(3)	2x
	D	478(3)	2x
	Co1	497(1)	2x
Co1	Sn	274(1)	6x
	U	292(1)	3x
	Co1	402(1)	2x
	D	418(1)	4x
	D	418(1)	8x
	U	431(1)	3x
	Co2	463(1)	12x
	U	497(1)	6x
Co2	D	179(3)	2x
	D	223(3)	2x
	Sn	272(1)	3x
	U	298(1)	6x
	Co2	402(1)	2x
	Co2	417(1)	3x
	D	454(1)	4x
	D	454(1)	2x
	Sn	457(1)	3x
	Co1	463(1)	6x
	D	473(2)	4x
	D	473(2)	2x
	Sn	485(1)	6x
Sn	Co2	272(1)	2x
	Co1	274(1)	2x
	U	316(1)	2x
	Sn	324(1)	2x
	D	325(2)	2x
	D	325(2)	2x
	U	325(1)	4x
	D	351(2)	2x
	D	352(2)	2x
	Sn	402(1)	2x

Atom 1	Atom 2	Distance (pm)	Coordination Number
	Co2	457(1)	2x
	Sn	471(1)	4x
	Co2	485(1)	4x
	D	491(1)	2x
	D	491(1)	2x
D	D	44(5)	1x
	Co2	179(3)	1x
	U	221(1)	1x
	U	221(1)	1x
	U	221(1)	1x
	Co2	223(3)	1x
	Sn	325(2)	1x
	Sn	325(2)	1x
	Sn	325(2)	1x
	Sn	351(2)	1x
	Sn	352(2)	1x
	Sn	352(2)	1x
	D	358(5)	1x
	D	402(5)	2x
	D	417(1)	2x
	D	417(1)	1x
	Co1	418(1)	1x
	Co1	418(1)	2x
	D	420(1)	1x
	D	420(1)	2x
	U	439(3)	1x
	U	439(3)	1x
	U	439(3)	1x
	D	446(5)	1x
	Co2	454(1)	2x
	Co2	454(1)	1x
	Co2	473(2)	2x
	Co2	473(2)	1x
	U	478(3)	1x
	U	478(3)	1x
	U	478(3)	1x
	Sn	491(1)	1x
	Sn	491(1)	1x
	Sn	491(1)	1x

Appendix D

Table of interatomic distances below 500 pm for $URuSnD_{0.6}$ compound

Atom 1	Atom 2	Distance (pm)	Coordination Number
U	D1	227(1)	2x
	D2	259(32)	2x
	D2	285(26)	1x
	Ru1	299(2)	1x
	Ru2	301(1)	4x
	Sn	324(3)	2x
	Sn	328(4)	4x
	U	393(3)	4x
	U	395(1)	2x
	Ru1	445(2)	1x
	D1	455(1)	4x
	D2	459(26)	1x
	D2	472(1)	4x
	D2	487(15)	2x
	Ru1	495(1)	2x
Ru1	D2	160(18)	3x
	Sn	273(2)	6x
	U	299(2)	3x
	Ru1	395(1)	2x
	D2	426(10)	6x
	D1	430(1)	6x
	U	445(2)	3x
	Ru2	473(1)	12x
	U	495(1)	6x
Ru2	D1	197(1)	2x
	Sn	283(2)	3x
	U	301(1)	6x
	D2	361(15)	6x
	Ru2	395(1)	2x
	Ru2	430(1)	3x
	Sn	469(4)	3x
	D1	473(1)	2x
	Ru1	473(1)	6x
	D1	473(1)	4x
	Sn	486(2)	6x
	D2	450(28)	6x
Sn	D2	199(4)	2x
	Ru1	273(3)	2x
	Ru2	283(2)	2x
	U	324(3)	2x
	Sn	326(5)	2x
	U	328(2)	4x
	D1	345(2)	4x
	D2	361(19)	4x
	Sn	395(1)	2x

Atom 1	Atom 2	Distance (pm)	Coordination Number
	Ru2	469(2)	2x
	Ru2	486(2)	4x
	Sn	490(4)	4x
D1	Ru2	197(1)	2x
	U	227(1)	3x
	D2	302(18)	3x
	Sn	345(2)	6x
	D1	395(1)	2x
	D1	430(1)	1x
	Ru1	430(1)	2x
	D1	430(1)	1x
	Ru1	430(1)	1x
	D1	430(1)	1x
	U	456(1)	6x
	D2	459(31)	3x
	Ru2	473(1)	6x
	D2	497(11)	6x
D2	Ru1	160(26)	1x
	Sn	199(4)	2x
	U	259(2)	2x
	D2	277(32)	2x
	U	285(26)	1x
	D1	302(18)	2x
	Ru2	361(15)	4x
	Sn	361(17)	4x
	D2	395(1)	2x
	Ru1	426(10)	2x
	D1	459(9)	2x
	U	459(26)	1x
	U	472(2)	4x
	D2	482(18)	4x
	U	487(15)	2x
	D1	497(11)	4x
	Ru2	499(8)	4x

Appendix E

X-ray powder patterns of $U_2Ni_2SnH_{1.8}$ and $U_2Ni_2InH_{1.9}$ (Cu-*K*α radiation). Observed patterns are represented by crosses, calculated – by solid line, the difference between the observed and calculated patterns is shown. R_B = 16.6% for URuSn, R_B= 10.1% for $U_2Ni_2InH_{1.9}$.

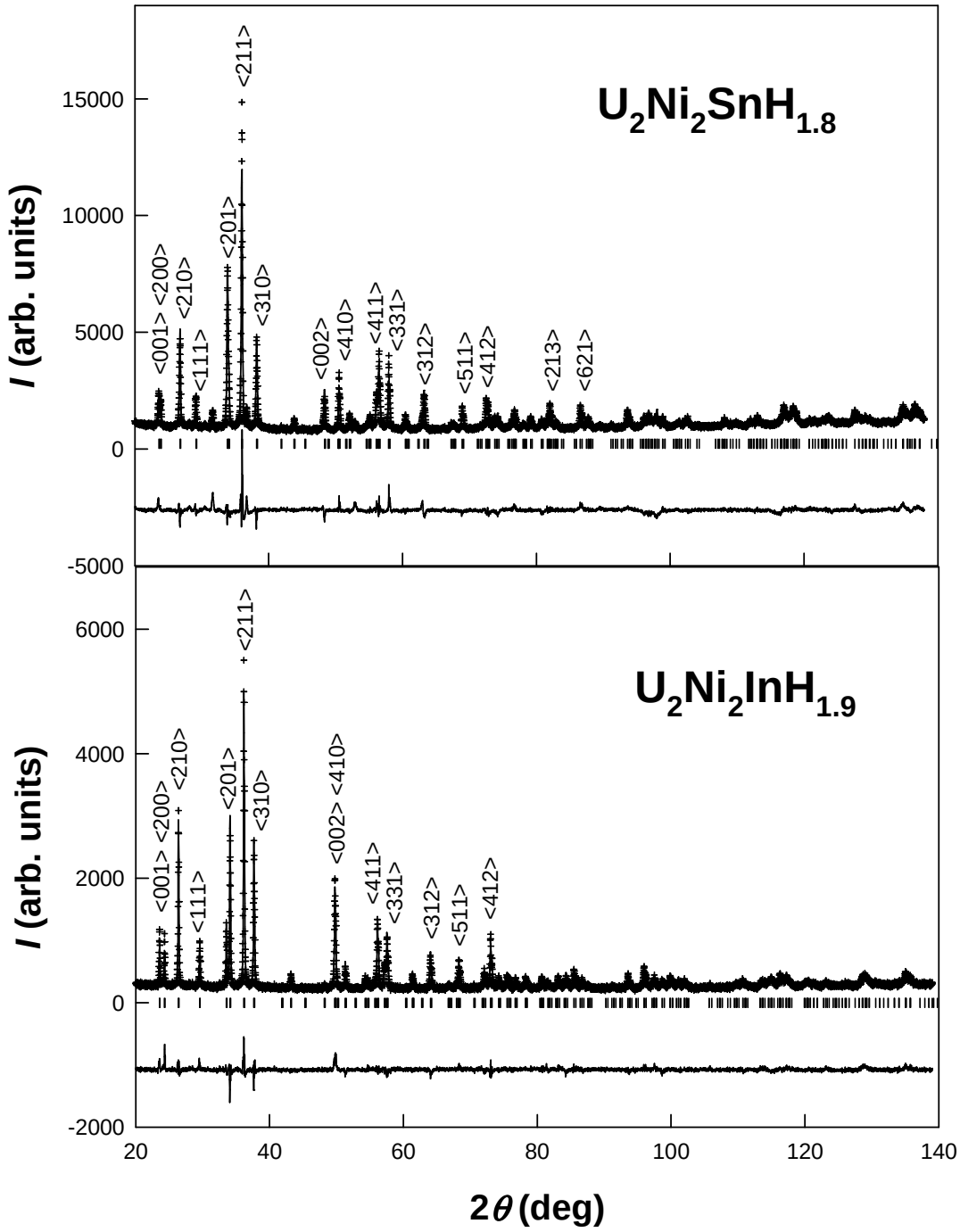

Appendix F

Table of interatomic distances below 400 pm for $U_2Ni_2SnD_{1.8}$ compound

Atom 1	Atom 2	Distance (pm)	Coordination Number
U	D	218(1)	2x
	D	223(1)	4x
	Ni	278(1)	2x
	Ni	296(1)	4x
	Sn	331(1)	4x
	U	376(1)	1x
	U	376(1)	2x
	U	3861(1)	4x
Ni	D	176(2)	2x
	D	201(2)	2x
	Ni	263(1)	1x
	U	279(1)	2x
	Sn	294(1)	2x
	U	297(1)	4x
	D	307(2)	2x
	D	322(2)	2x
	Ni	376(1)	2x
Sn	Ni	294(1)	4x
	U	332(1)	8x
	D	347(2)	8x
	D	360(2)	8x
	Sn	376(1)	2x
D	D	25(4)	1x
	Ni	176(3)	1x
	Ni	201(3)	1x
	U	218(1)	1x
	U	223(1)	2x
	D	240(1)	1x
	D	241(1)	1x
	Ni	307(2)	1x
	Ni	322(2)	1x
	Sn	347(2)	2x
	D	351(4)	1x
	Sn	360(2)	2x
	D	376(4)	2x